UNIVERSIDADE FEDERAL DO RIO GRANDE DO NORTE
CENTRO DE CIÊNCIAS EXATAS E DA TERRA
PROGRAMA DE PÓS-GRADUAÇÃO EM GEODINÂMICA E GEOFISICA

TESE DE DOUTORADO

IMPACTOS DA DISSOLUÇÃO CÁRSTICA NA PERMO-POROSIDADE DE ROCHAS CARBONÁTICAS: IMPLICAÇÕES PARA O DESENVOLVIMENTO DE REDES DE FRATURAS ALARGADAS E CAMADAS SUPER-K

Autora:
JULIANA APARECIDA GONÇALVES LOPES

Orientador:
PROF. DR. WALTER EUGÊNIO DE MEDEIROS

Tese nº 74/PPGG

Setembro de 2022
Natal/RN, Brasil

JULIANA APARECIDA GONÇALVES LOPES

IMPACTOS DA DISSOLUÇÃO CÁRSTICA NA PERMO-POROSIDADE DE ROCHAS CARBONÁTICAS: IMPLICAÇÕES PARA O DESENVOLVIMENTO DE REDES DE FRATURAS ALARGADAS E CAMADAS SUPER-K

Tese apresentada no dia 30 de setembro de 2022 ao Programa de Pós-Graduação em Geodinâmica e Geofísica (PPGG) da Universidade Federal do Rio Grande do Norte (UFRN) como requisito a obtenção do Título de Doutora em Geodinâmica e Geofísica, Área de concentração Geofísica.

BANCA EXAMINADORA:

____

PROF. DR. WALTER EUGÊNIO DE MEDEIROS
Presidente e orientador (PPGG/UFRN)

____

PROF. DR. ADERSON FARIAS DO NASCIMENTO
Membro interno (PPGG/UFRN)

____

DR. FABIO LUIZ BAGNI
Membro externo (PETROBRAS)

____

PROF. DR. FABRIZIO BÁLSAMO
Membro externo (Università di Parma)

____

PROF. DR. RENATO RAMOS DA SILVA DANTAS
Membro externo (UFRN)

Universidade Federal do Rio Grande do Norte - UFRN
Sistema de Bibliotecas - SISBI
Catalogação de Publicação na Fonte. UFRN - Biblioteca Setorial Prof. Ronaldo Xavier de Arruda - CCET

Lopes, Juliana Aparecida Gonçalves.
Impactos da dissolução cárstica na permo-porosidade de rochas carbonáticas: implicações para o desenvolvimento de redes de fraturas alargadas e camadas super-k / Juliana Aparecida Gonçalves Lopes. - 2022.
124f.: il.

Tese (Doutorado) - Universidade Federal do Rio Grande do Norte, Centro de Ciências Exatas e da Terra, Programa de Pós-Graduação em Geodinâmica e Geofísica. Natal, 2022.
Orientador: Prof. Dr. Walter Eugênio de Medeiros.

1. Geofísica - Tese. 2. Reservatórios carbonáticos - Tese. 3. Análogos de reservatórios - Tese. 4. Dissolução cárstica - Tese. 5. Redes de fratura - Tese. 6. Zonas de alta permeabilidade - Tese. 7. Super-k - Tese. I. Medeiros, Walter Eugênio de. II. Título.

RN/UF/CCET CDU 550.3

Elaborado por Joseneide Ferreira Dantas - CRB-15/324

Aos meus pais, meu marido, e meu filho
que inspiram o melhor de mim todos os dias.

AGRADECIMENTOS

Ao apoio financeiro do projeto de P&D em andamento registrado como ANP 20502-1, "Processos e Propriedades em Reservatórios Carbonáticos Fraturados e Carstificados – POROCARSTE 3D" (UFRN/UNB/UFRJ/UFC/Shell Brasil/ANP) – Porokarst – Processos e Propriedades em Reservatórios Carbonáticos Fraturados e Karstificados, patrocinado pela Shell Brasil sob a taxa de P&D da ANP como "Compromisso de Investimento com Pesquisa e Desenvolvimento".

À Universidade Federal do Rio Grande do Norte, pela ótima estrutura para a realização desta tese, e ao Programa de Pós-Graduação em Geodinâmica e Geofísica (PPGG) pela oportunidade.

Ao meu orientador, Prof. Dr. Walter Eugênio de Medeiros, por todos os ensinamentos e pela dedicação durante todo o desenvolvimento desta tese. Além disso, não posso deixar de agradecê-lo por todo apoio e compreensão durante a minha maternidade, que coincidiu com o final do doutorado.

Ao Prof. Dr. Francisco Hilário Rego Bezerra, pela confiança e acolhimento durante todo o meu período de pós-graduação na UFRN.

Ao Profs. Drs. Josibel Gomes de Oliveira Jr., Milton Morais Xavier Jr. e Francisco Pinheiro Lima Filho, aos amigos e colaboradores tanto na UFRN, Flávio Lemos, Bruno Baraúna, Renata Araújo, Vincenzo La Bruna e Tomaz Bezerra, como na Unicamp, Alexandre de Lima, pelo apoio e/ou colaboração nas diversas etapas da minha pesquisa.

A todos os professores e funcionários do Departamento de Geologia e do Departamento de Geofísica (DGEO e DGEF), com quem convivi nos últimos quatro anos e meio. Em especial, a Antônio Vicente e Naiyan, os quais me deram todo o suporte técnico para desenvolvimento desta Tese.

Aos colegas do LABSIS/LAGAP, Nitzchia, Ingrid, Iurianne, Fabio, Cayo, Lorenna, Victória e João Victor, pelos momentos de angústia e alegrias vividos, além de todo conhecimento compartilhado.

Aos meus queridos amigos Patrícia, Juliana e David por todo apoio, além das contribuições e discussões acadêmicas.

À minha família Potiguar. Em especial: tia Didi, tia Lenol e Dona Sandra, por cuidarem tão bem do meu pequeno na minha ausência durante os momentos decisivos para a conclusão da tese.

Aos meus pais, Alcides e Kátia, e meu irmão Alcides Neto, pela confiança e incentivo. Em especial aos meus pais, por todo amor e suporte, indispensáveis para a conclusão de mais essa etapa na minha vida.

Ao meu marido Ricardo, por todo apoio, companheirismo, paciência, e pelo meu maior presente: nosso filho, João Ricardo. Foi o João que me mostrou o quão forte e perseverante eu posso ser. Obrigada, filho!

Aos membros da banca, Prof. Dr. Aderson Farias do Nascimento, Dr. Fabio Luiz Bagni, Prof. Dr. Fabrizio Bálsamo e Prof. Dr. Renato Ramos da Silva Dantas pela avaliação e valiosas contribuições.

Por fim, agradeço a todos que contribuíram de alguma forma para a realização deste trabalho.

RESUMO

Nós avaliamos o impacto da dissolução cárstica no sistema permo-poroso de rochas carbonáticas, utilizando dados de campo obtidos em afloramentos da Formação Jandaíra (Bacia Potiguar). O sistema cárstico desta formação apresenta excelentes exposições, que permitem o estudo das feições cársticas tanto em planos verticais quanto em planos horizontais. A abordagem integrada e multidisciplinar desta tese foi feita em duas etapas. A primeira etapa foi dominantemente bidimensional (2D), na qual utilizamos *scanlines* e imagens aéreas de Veículos Aéreos Não Tripulados para caracterizar redes de fraturas subverticais carstificadas. Nesta etapa, nós mostramos que o processo de alargamento das fraturas por dissolução cárstica modifica as relações estatísticas entre comprimento e abertura das fraturas. Para estágios iniciais de dissolução cárstica, os valores de comprimento e abertura seguem aproximadamente a clássica lei de potência típica de fraturas de origem mecânica. No entanto, com o avanço da carstificação, a abertura das fraturas tende a ficar constante, independentemente do seu comprimento. Dessa forma, adaptando a curva de abertura-comprimento, de acordo com o estágio conhecido de dissolução cárstica, é possível contruir modelos discretos de fraturas que incluam os efeitos da dissolução cárstica. Nós chamamos o modelo resultante de DFKN (*Discrete Fracture and Karst Network*). Mostramos ainda que o alargamento das fraturas pode aumentar a transmissividade de uma rede de fraturas carstificadas em até cinco ordens de magnitude, sem alterar sua conectividade. A segunda etapa da pesquisa consiste de uma análise tridimensional (3D) de redes de fraturas, interfaces litoestratigráficas e feições cársticas, a partir da interpretação conjunta de cubos de Radar de Penetração no Solo (GPR), testemunhos de sondagem, perfis de porosidade, permeabilidade e radiação total, imagens de paredes de poço e lâminas delgadas. Nesta etapa nós verificamos que zonas de atenuação do sinal de GPR estão relacionadas a alterações secundárias das rochas carbonáticas, que são causadas por fraturamento, alargamento de fraturas e poros, além de dissolução de estilólitos. Tais alterações secundárias aumentam significativamente a porosidade e permeabilidade das rochas. As fraturas são as vias principais para a percolação de fluidos, contribuindo para a evolução dos processos de carstificação, principalmente nas camadas com maior porosidade/permeabilidade primárias. Por outro lado, camadas com baixa porosidade/permeabilidade primárias, mas com alta concentração de estilólitos, também podem desenvolver zonas de alta permeabilidade devido à interconexão dos estilólitos dissolvidos. As zonas de atenuação/dissolução podem compor volumes conectados de alta permeabilidade e geralmente apresentam geometria tabular, porque são limitadas por fraturas subverticais e interfaces estratigráficas subhorizontais. Na escala de reservatório, estes corpos tabulares podem constituir camadas super-k. Numa visão unificada, nossos resultados contribuem para uma melhor compreensão do sistema permo-poroso tridimensional de reservatórios carbonáticos fraturados e carstificados.

Palavras-chave: Reservatórios carbonáticos; análogos de reservatórios; dissolução cárstica; redes de fratura; zonas de alta permeabilidade; super-k.

ABSTRACT

We evaluated the impact of karst dissolution on the permo-porous system of carbonate rocks, using field data obtained from outcrops of the Jandaíra Formation (Potiguar Basin). The karst system of this formation has excellent exposures, which allow the study of karst features both in vertical and horizontal planes. The integrated and multidisciplinary approach of this thesis was carried out in two stages. The first stage was predominantly two-dimensional (2D), in which we used scanlines and aerial images of Unmanned Aerial Vehicles to characterize networks of karstified subvertical fractures. In this stage, we show that the process of fractures enlargement by karstic dissolution modifies the statistical relationships between fracture length and aperture. For early stages of karst dissolution, the length and aperture values follow approximately the classical power law distribution typical of mechanical fractures. However, as karstification progresses, fracture aperture tends to remain constant, regardless of its length. Thus, by adapting the aperture-length curve, according to the known stage of karst dissolution, it is possible to build discrete fracture models that include the effects of karstic dissolution. We call the resulting model DFKN (Discrete Fracture and Karst Network). We also show that fracture enlargement can increase the transmissivity of a karstified fracture network by up to five orders of magnitude, without changing its connectivity. The second stage of the research consists of a three-dimensional (3D) analysis of fracture networks, lithostratigraphic interfaces and karst features, based on the joint interpretation of Ground Penetrating Radar (GPR) cubes, core logs, porosity, permeability and total radiation profiles, images of borehole walls and thin sections. In this stage we verified that GPR signal attenuation zones are related to secondary alterations of carbonate rocks, which are caused by fracturing, fracture and pore enlargement, as well as stylolite dissolution. Such secondary alterations significantly increase the porosity and permeability of rocks. Fractures are the main pathways for fluid percolation, contributing to the evolution of karstification processes, especially in layers with higher primary porosity/permeability. On the other hand, layers with low primary porosity/permeability, but with a high concentration of stylolites, can also develop zones of high permeability due to the interconnection of dissolved stylolites. The attenuation/dissolution zones can compose connected volumes of high permeability and generally have tabular geometry, because they are limited by subvertical fractures and subhorizontal stratigraphic interfaces. At the reservoir scale, these tabular bodies may constitute super-k layers. In a unified view, our results contribute to a better understanding of the three-dimensional permo-porous system of fractured and karstified carbonate reservoirs.

Keywords: Carbonate reservoirs; reservoir analogues; karst dissolution; fracture networks; high permeability zones; super-k.

LISTA DE FIGURAS

CAPÍTULO 1

CAPÍTULO 2

CAPÍTULO 3

LISTA DE TABELAS

CAPÍTULO 2

CAPÍTULO 3

SUMÁRIO

1. INTRODUÇÃO

1.1 Apresentação

Esta Tese de Doutorado foi desenvolvida sob a orientação do Prof. Dr. Walter Eugênio de Medeiros, e visa atender aos requisitos necessários para a obtenção do Título de Doutora em Geodinâmica e Geofísica, pelo Programa de Pós-graduação em Geodinâmica e Geofísica da Universidade Federal do Rio Grande do Norte (UFRN). A presente tese está vinculada ao projeto "Processos e propriedades em reservatórios carbonáticos fraturados e carstificados", sigla "Porocarste 3D", que foi financiado pela Shell Brasil Petróleo e coordenado pelo Prof. Dr. Francisco Hilário Rego Bezerra.

O objetivo central desta pesquisa é avaliar o impacto da dissolução cárstica no sistema permo-poroso de rochas carbonáticas. Para tanto, foram utilizadas imagens de GPR (Radar de Penetracão no Solo) e VANT (Veículo Aéreo Não Tripulado), *scanlines*, imagens de poços e testemunhos, lâminas delgadas e medidas petrofísicas de porosidade, permeabilidade e radiação total. Para realizar esta abordagem multidisciplinar, nós contamos com uma rede de colaboradores, que incluiu: Prof. Dr. Francisco Hilário Bezerra, Prof. Dr. Vincenzo La Bruna e nossa colega doutoranda Renata Emilly de Araújo Brito, que nos auxiliaram nas etapas de campo, interpretação de dados estruturais e na descrição dos testemunhos de sondagem; Sr. Francisco Tomaz Lima Bezerra, que nos auxiliou na aquisição e processamento das imagens de VANT; Prof. Dr. Josibel Gomes de Oliveira Jr., Dr. Flávio Lemos de Santana, MSc. Bruno Baraúna dos Santos e Sr. Antônio Vicente do Nascimento, que nos auxiliaram nas etapas de aquisição e/ou processamento dos dados de GPR, bem como de perfuração dos poços e imageamento das paredes dos poços; Prof. Dr. Milton Morais Xavier Jr. e Prof. Dr. Francisco Pinheiro Lima Filho, que nos auxiliaram na realização das medidas petrofísicas, e o doutorando Alexandre de Lima (UNICAMP), com quem interagimos para elaborar um modelo DFKN (redes discretas de fraturas carstificadas) determinístico.

1.2 Estrutura da tese

Esta Tese de Doutorado está estruturada em cinco capítulos, dois deles elaborados na forma de artigos científicos, de modo a cumprir os requisitos do PPGG para a obtenção do grau de doutor.

O presente Capítulo 1 apresenta uma visão geral da tese e de suas justificativas, de modo a orientar o leitor quanto a área de estudo e os resultados gerais obtidos.

O capítulo 2 apresenta a primeira parte dos resultados da tese, que estão contidos no artigo "*Advancements towards DFKN modelling: Incorporating fracture enlargement resulting from karstic dissolution in discrete fracture networks*", que foi publicado no fascículo de novembro de 2021 do periódico *Journal of Petroleum Science and Engineering*. Neste artigo nós apresentamos a metodologia utilizada e os resultados e discussões da interpretação bidimensional (2D) e multiescalar de redes de fratura subverticais carstificadas, visando elaborar um modelo determinístico de redes de fraturas que incluam os efeitos do alargamento das fraturas devido à dissolução cárstica.

O capítulo 3 apresenta a segunda parte dos resultados da tese, que compõem o manuscrito "*Three-dimensional characterization of karstic dissolution zones, fracture networks, and lithostratigraphic interfaces using GPR cubes, core logs, and petrophysics: implications for thief zones development in carbonate reservoirs*", que foi submetido para publicação em 10/09/2022 no periódico *Marine and Petroleum Geology*. Este manuscrito apresenta a metodologia e os resultados e discussões da abordagem multidisciplinar 3D, em que caracterizamos os principais fatores que controlam a formação de volumes conectados de rochas carbonáticas, com alta permeabilidade, que podem resultar de alterações secundárias.

O capítulo 4 apresenta de forma sucinta três pesquisas adicionais, também desenvolvidas no âmbito do projeto Porocarste 3D e em temas estreitamente relacionados com o tema desta tese, nas quais a sua autora colaborou. Resultaram destas pesquisas três artigos científicos publicados e/ou submetidos em periódicos científicos, nos quais a autora da presente tese consta como coautora.

Por fim, o Capítulo 5, apresenta uma visão integral sumária dos resultados da presente tese.

1.3 Justificativas

Fraturas e feições cársticas afetam significativamente o fluxo de fluido subsuperficial em reservatórios carbonáticos (e.g., Biver et al., 2012; Medekenova and Jones, 2014; Liu et al., 2021). Sistemas de fraturas desempenham um papel fundamental na percolação de fluidos em várias escalas, e são as principais responsáveis pela circulação de fluidos em rochas com matriz de baixa porosidade/permeabilidade, como os carbonatos (Nelson, 2001; Davy et al., 2010; Hardebol et al., 2015; Araújo et al., 2021). As feições cársticas, por sua vez, resultam da dissolução de rochas carbonáticas, que muitas vezes ocorrem ao longo de descontinuidades estruturais e sedimentares (James e Choquette et al., 1988; Araújo et al., 2021), resultando em um arcabouço bastante heterogêneo e complexo.

Em reservatórios carbonáticos, as fraturas facilitam o processo de dissolução cárstica (e.e. Cazarin et al., 2018; Bagni et al., 2020; Araújo et al., 2021), aumentando significativamente a porosidade e a permeabilidade secundária das rochas carbonáticas (Jones, 2015; Bagni et al., 2022; Lopes et al., 2022). Esse aumento da porosidade e permeabilidade leva a formação de zonas de alta permeabilidade, as quais são, geralmente, associadas a falhas e fraturas (La Bruna et al., 2021; Cross et al., 2021). Isso faz com que essas zonas sejam subestimadas na caracterização dos reservatórios, especialmente quando ocorrem na escala subsísmica. Além disso, camadas com alta permeabilidade, como camadas super-k, podem desencadear uma série de eventos indesejáveis, como queda de pressão de fluidos e chegada prematura de água nos poços produtores (Medeiros et al., 2004; Yixiang et al., 2017).

É quase sempre difícil identificar feições cársticas com dados sísmicos devido aos limites de resolução (Medekenova e Jones., 2014; Tian et al., 2019a; La Bruna et al., 2021). Além disso, geralmente existem pouco poços exploratórios, criando uma lacuna nas informações sobre dimensões e conectividade das fraturas e sistemas cársticos no espaço tridimensional do reservatório (Medekenova e Jones, 2014; Jones, 2015; Li et al., 2016; Yan et al., 2022).

Uma maneira de compreender melhor a relação entre fraturas e feições cársticas na escala subsísmica é a partir do estudo de afloramentos análogos, onde as propriedades geométricas dessas estruturas podem ser diretamente analisadas (Ennes-Silva et al., 2016; Menezes et al., 2020; Bagni et al., 2020) e utilizadas para elaborar modelos determinísticos e estocásticos (e.g., Hardebol et al., 2015; Giuffrida et al., 2019; Massaro et al., 2019), bem como modelos conceituais (La Bruna et al., 2021; Araújo et al., 2021). Assim, o estudo de afloramentos análogos é fundamental para a caracterização de fraturas e feições cársticas e ajudam a reduzir as incertezas na caracterização de reservatórios carbonáticos (Howell et al., 2014; Gutmanis et al., 2017; Becker et al., 2018 ; Giuffrida et al., 2019). Além disso, a combinação de dados geológicos e geofísicos nos permite estabelecer relações entre a escala micro e macro, contribuindo para uma melhor compreensão das heterogeneidades intrínsecas aos reservatórios carbonáticos (Tian et al., 2019a, 2019b).

Por esse motivo, esse trabalho foca na caracterização 2D e 3D de redes de fraturas e feições cársticas, com o objetivo de compreender melhor o papel da dissolução na formação de porosidade e permeabilidade secundárias em rochas carbonáticas. Nossos resultados poderão ser utilizados na elaboração de modelos de reservatórios, de modo a subsidiar estudos de simulação e gerenciamento de reservatórios fraturados e carstificados.

1.4 Área de estudo

As áreas escolhidas para esta pesquisa incluem os lajedos Soledade e Arapuá, que afloram na Formação Jandaíra. Esta formação constitui uma plataforma carbonática intensamente carstificada, que aflora nas porções centro-oeste e leste da Bacia Potiguar, no estado do Rio Grande do Norte (Figura 1). Devido ao clima semi-árido, o sistema cárstico da Formação Jandaíra está bem preservado e apresenta excelentes afloramentos, que permitem o estudo das feições cársticas tanto no plano vertical quanto no plano horizontal (Fernandes et al., 2015; Araújo et al., 2021).

1.5 Objetivos

Esta pesquisa tem como objetivo principal compreender como a dissolução cárstica influencia a porosidade e permeabilidade das rochas carbonáticas, de modo a contribuir com a elaboração de modelos preditivos de reservatórios carbonáticos fraturados e carstificados. Para tanto, nós utilizamos abordagens 2D e 3D multiescalares e multidisciplinares, que nos permitiram alcançar os seguintes objetivos específicos:

- Avaliar qualitativamente o arcabouço estrutural dos afloramentos estudados;
- Determinar as leis de escala que governam a distribuição dos comprimentos e aberturas das fraturas;
- Compreender como o arranjo das fraturas controla o processo de carstificação;
- Compreender como o grau de carstificação impacta as leis de escala e a transmissividade dos sistemas de fraturas;

- Elaborar um modelo determinístico incorporando o alargamento das fraturas devido a dissolução cárstica para avaliar o impacto da carstificação em modelos de reservatórios;
- Interpretar tridimensionalmente os arcabouços estratigráficos e estruturais de rochas carbonáticas;
- Delimitar tridimensionalmente as zonas de alteração secundárias em rochas carbonáticas;
- Identificar os principais fatores que controlam o desenvolvimento de zonas de dissolução.
- Construir um modelo conceitual para a formação de zonas de alta permeabilidade em reservatórios carbonáticos.

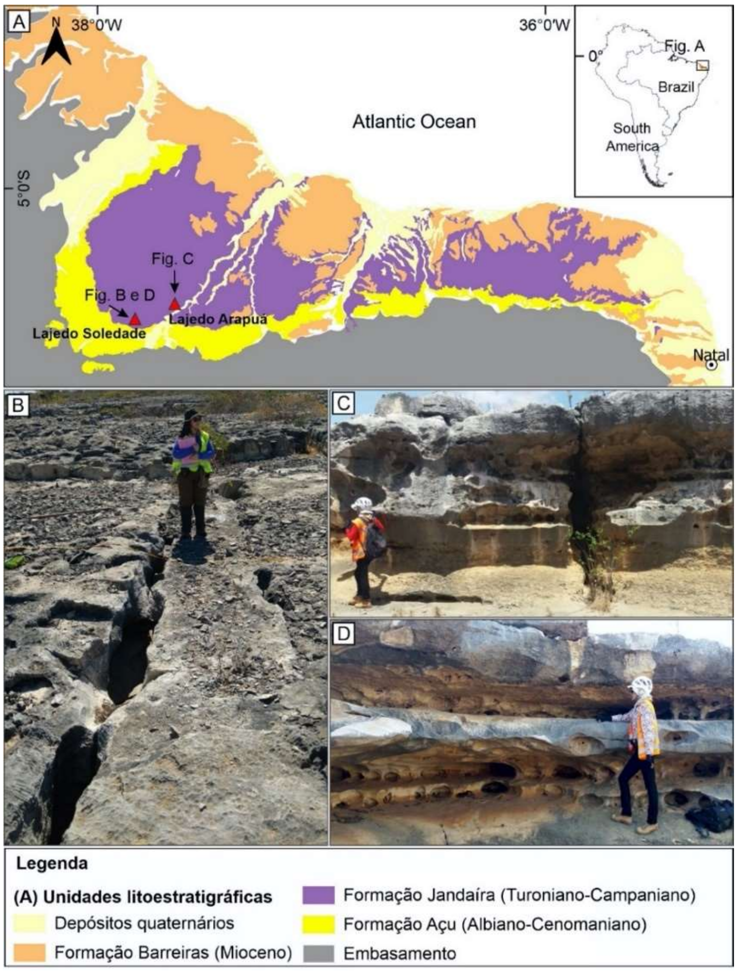

Figura 1: (A) Mapa geológico simplificado da Bacia Potiguar. Os triângulos vermelhos indicam as áreas de estudo. As fotografias mostram, no Lajedo Soledade, a dissolução

cárstica ocorrendo ao longo de fraturas sub-verticais (B e C) e acompanhando superfícies subhorizontais (D).

REFERÊNCIAS

Araújo, R. E., La Bruna, V., Rustichelli, A., Bezerra, F. H., Xavier, M. M., Audra, P., ... Antonino, A. C. 2021. Structural and sedimentary discontinuities control the generation of karst dissolution cavities in a carbonate sequence, Potiguar Basin, Brazil. Mar. Pet. Geol. 123, 104753.

Bagni, F.L., Bezerra, F.H., Balsamo, F., Maia, R.P., Dall'Aglio, M., 2020. Karst dissolution along fracture corridors in an anticline hinge, Jandaíra Formation, Brazil: Implications for reservoir quality. Mar. Pet. Geol. 115, 104249.

Bagni, F.L., Erthal, M.M., Tonietto, S.N., Maia, R.P., Bezerra, F.H., Balsamo, F., Córdoba, V.C., de Souza, F.G., Brod, J.A., Fernandes, C.P., Fonseca, J.P.T., 2022. Karstified layers and caves formed by superposed epigenic dissolution along subaerial unconformities in carbonate rocks – Impact on reservoir-scale permeability. Mar. Pet. Geol. 138. https://doi.org/10.1016/j.marpetgeo.2022.105523

Becker, I., Koehrer, B., Waldvogel, M., Jelinek, W., Hilgers, C., 2018. Comparing fracture statistics from outcrop and reservoir data using conventional manual and t-LiDAR derived scanlines in Ca2 carbonates from the Southern Permian Basin, Germany. Mar. Pet. Geol. 95, 228–245. https://doi.org/10.1016/j.marpetgeo.2018.04.021

Biver, P., Longis, C., Penna, E., Ovsyannikov, A., 2012. Modeling uncertainties in carbonate karstic reservoirs: Presentation of a tool and its application to a real field case in Russia. In SPE Russian Oil and Gas Exploration and Production Technical Conference and Exhibition. Society of Petroleum Engineers. https://doi.org/10.2118/160721-RU

Cazarin, C.L., Bezerra, F.H.R., Borghi, L., Santos, R. V., Favoreto, J., Brod, J.A., Auler, A.S., Srivastava, N.K., 2018. The conduit-seal system of hypogene karst in Neoproterozoic carbonates in northeastern Brazil. Mar. Pet. Geol. 101, 90–107. https://doi.org/10.1016/j.marpetgeo.2018.11.046

Cross, N.E., van Veen, L.J., Al-Enezi, A., Singh, S., van Beusekom, G., 2021. Seismic Geomorphology of Karst in Cretaceous to Early Cenozoic Carbonates of North

Kuwait. Mar. Pet. Geol. 128, 104947. https://doi.org/10.1016/j.marpetgeo.2021.104947

Davy, P., Le Goc, R., Darcel, C., Bour, O., De Dreuzy, J.R., Munier, R., 2010. A likely universal model of fracture scaling and its consequence for crustal hydromechanics. J. Geophys. Res. Solid Earth 115, 1–13. https://doi.org/10.1029/2009JB007043

Ennes-Silva, R.A., Bezerra, F.H.R., Nogueira, F.C.C., Balsamo, F., Klimchouk, A., Cazarin, C.L., Auler, A.S., 2016. Superposed folding and associated fracturing influence hy- pogene karst development in Neoproterozoic carbonates, São Francisco Craton, Brazil. Tectonophysics 666, 244–259. https://doi.org/10.1016/j.tecto.2015.11.006.

Fernandes, A.L., Medeiros, W.E., Bezerra, F.H.R., Oliveira, J.G., Cazarin, C.L., 2015. GPR investigation of karst guided by comparison with outcrop and unmanned aerial vehicle imagery. J. Appl. Geophys. 112, 268–278. https://doi.org/10.1016/j.jappgeo.2014.11.017

Giuffrida, A., La Bruna, V., Castelluccio, P., Panza, E., Rustichelli, A., Tondi, E., Giorgioni, M., Agosta, F., 2019. Fracture simulation parameters of fractured reservoirs: Analogy with outcropping carbonates of the Inner Apulian Platform, southern Italy. J. Struct. Geol. 123, 18–41.

Gutmanis, J., I Oró, L.A., DíEz-Canseco, D., Chebbihi, L., Awdal, A., Cook, A., 2017. Fracture analysis of outcrop analogues to support modelling of the subseismic domain in carbonate reservoirs, south-central Pyrenees. Geol. Soc. Spec. Publ. 459, 139–156. https://doi.org/10.1144/SP459.2

Hardebol, N. J., Maier, C., Nick, H., Geiger, S., Bertotti, G., Boro, H., 2015. Multiscale fracture network characterization and impact on flow: A case study on the Latemar carbonate platform. Journal of Geophysical Research: Solid Earth, 120(12), 8197-8222. https://doi.org/10.1002/2015JB011879

Howell, J.A., Martinius, A.W., Good, T.R., 2014. The application of outcrop analogues in geological modelling: a review, present status and future outlook. Geol. Soc. London, Spec. Publ. 387, 1–25. https://doi.org/10.1144/sp387.12

Jones, G.D., 2015. Flow-Based Effective Properties of Sub-Seismic Karst Karst Flow-Based Properties Geologic Modeling Workflow Overview 8–11. https://doi.org/10.2118/172648-MS

La Bruna, V., Bezerra, F.H.R., Souza, V.H.P., Maia, R.P., Auler, A.S., Araujo, R.E.B., Cazarin, C.L., Rodrigues, M.A.F., Vieira, L.C., Sousa, M.O.L., 2021. High-permeability zones in folded and faulted silicified carbonate rocks – Implications for karstified carbonate reservoirs. Mar. Pet. Geol. 128, 105046.

Li, D., Yang, J., Lu, D., 2016a. Thief zone identification based on transient pressure analysis: a field case study. J. Pet. Explor. Prod. Technol. 6, 63–72. https://doi.org/10.1007/s13202015-0168-8

Liu, H., Shi, K., Liu, B., Song, X., Deng, L., Guo, R., Tian, Z., Li, Y., Deng, Y., Wang, G., 2021. The characteristics and origins of thief zones in the Cretaceous limestone reservoirs of Central and southern Mesopotamian Basin. J. Pet. Sci. Eng. 201, 108395. https://doi.org/10.1016/j.petrol.2021.108395

Lopes, J.A.G., Medeiros, W.E., La Bruna, V., Lima, A. De, Bezerra, F.H.R., Schiozer, D.J., 2022. Advancements towards DFKN modelling : Incorporating fracture enlargement resulting from karstic dissolution in discrete fracture networks. J. Pet. Sci. Eng. 209. https://doi.org/10.1016/j.petrol.2021.109944

Massaro, L., Corradetti, A., Tramparulo, F.D., Vitale, S., Prinzi, E.P., Iannace, A., Parente, M., Invernizzi, C., Morsalnejad, D., Mazzoli, S., 2019. Discrete fracture network modelling in triassic–jurassic carbonates of NW lurestan, zagros fold-and-thrust belt, Iran. Geosci. 9, 1–24. https://doi.org/10.3390/geosciences9120496

Medeiros, R.S., Biswas, D., DeGolyer, MacNaughton, Suryanarayana, P. V., 2004. Impact of thief zone identification and shut-off on water production in the nimr field. SPE/IADC Underbalanced Technol. Conf. Exhib. - Proc. 297–303. https://doi.org/10.2523/91665-ms

Medekenova, A., Jones, G.D., 2014. Characterization and modeling challenges associated with fracture and karst (non-matrix) in the margin area of a carbonate reservoir. Soc. Pet. Eng. - SPE Annu. Casp. Tech. Conf. Exhib. https://doi.org/10.2118/172275-ms

Menezes, D.F., Bezerra, F.H., Balsamo, F., Arcari, A., Maia, R.P., Cazarin, C.L., 2020. Subsidence rings and fracture pattern around dolines in carbonate platforms – Implications for evolution and petrophysical properties of collapse structures. Mar. Pet. Geol. 113, 104113. https://doi.org/10.1016/j.marpetgeo.2019.104113

Nelson, R. A.,2001. Geologic Analysis of Naturally Fractured Reservoirs, 2nd ed., Gulf Prof. Publ. Co., Boston, Mass.

Tian, F., Di, Q., Jin, Q., Cheng, F., Zhang, W., Lin, L., ..., Li, Y. 2019a. Multiscale geological-geophysical characterization of the epigenic origin and deeply buried paleokarst system in Tahe Oilfield, Tarim Basin. Mar. Pet. Geol., 102, 16-32. https://doi.org/10.1016/j.marpetgeo.2018.12.029

Tian, F., Luo, X., Zhang, W., 2019b. Integrated geological-geophysical characterizations of deeply buried fractured-vuggy carbonate reservoirs in Ordovician strata, Tarim Basin. Mar. Pet. Geol. 99, 292–309. https://doi.org/10.1016/j.marpetgeo.2018.10.028

Yan, L., Liu, Q., Liu, X., 2022. Research on 3D geological modeling of fractured-vuggy carbonate reservoirs. Energy Reports 8, 491–500. https://doi.org/10.1016/j.egyr.2022.03.052

Yixiang, Z., Xinmin, S., Benbiao, S., Shuiqing, H., Changbing, T., Yan, G., Weimin, Z., Yong, L., 2017. Genesis of High Permeable Thief-zones and Integrated Reservoir Modeling of Intense Heterogeneous Reef-flat Carbonates : A Case Study for the Mishrif Formation of the Rumaila Oilfield , Iraq. SPE Annu. Tech. Conf. Exhib. 1–12. https://doi.org/https://doi.org/10.2118/187235-MS

2. ARTIGO PUBLICADO

O conteúdo deste capítulo foi publicado no *Journal of Petroleum Science and Engineering* no Volume 209, February 2022, 109944. https://doi.org/10.1016/j.petrol.2021.109944

Advancements towards DFKN modelling: Incorporating fracture enlargement resulting from karstic dissolution in discrete fracture networks

Juliana A.G. Lopes[(a)], Walter E. Medeiros[(a)(b)(e)], Vincenzo La Bruna[(a)(c)], Alexandre de Lima[(d)], Francisco H.R. Bezerra[(a)(c)], and Denis José Schiozer[(d)]

(a) Post-Graduation Program on Geodynamics and Geophysics, Federal University of Rio Grande do Norte, Natal, Brazil

(b) Department of Geophysics, Federal University of Rio Grande do Norte, Natal, Brazil, and INCT-GP/CNPq/CAPES-National Institute of Science and Technology in Petroleum Geophysics

(c) Department of Geology, Federal University of Rio Grande do Norte, Natal, Brazil

(d) Department of Energy, Division of Petroleum Engineering, FEM, UNICAMP/CEPETRO, Campinas, Brazil

(e) Corresponding author

Abstract

We present a multiscale approach to develop a deterministic Discrete Fracture Network (DFN) model including fracture enlargement due to karstic dissolution in low-porosity carbonate rocks. The result is a DFKN (Discrete Fracture and Karst Network) model from which it is possible to quantify, in a practical manner, the impact of fracture enlargement due to karstic dissolution on the fracture network transmissivity. We provide a case study using two large outcrops in the Jandaíra Formation, an intensely karstified carbonate platform of Turonian-Campanian age in the Potiguar Basin, Brazil. The study is based on scanlines collected both in field and from Unmanned Aerial Vehicle (UAV) imagery, allowing to cover three orders of magnitude in length and aperture of fractures. We found that if karstic dissolution is low, aperture-length data plotted on bi-logarithmic graphs can be fitted by straight lines, thus following the aperture-length power law typical of mechanical apertures. However, advanced stages of karstification modifies the aperture-length relationship due to the fact that dissolution causes similar fracture enlargement regardless of fracture length. As a result, the aperture-length curve gradually degenerates to a constant value as the degree of dissolution increases. This behavior is the key to quantitatively taking into account fracture enlargement, by simply adapting an aperture-length curve according to the known stage of karstic dissolution of the modeled carbonate rocks. We show that fracture enlargement can increase the transmissivity of a karstified fracture network by up to five orders of magnitude without changing its connectivity. Our approach can be useful to better understand the behavior of fluid flow in carbonate reservoirs with fracture networks affected by karstic dissolution.

Keywords: Carbonate reservoirs; discrete fracture networks; karstified fracture networks; fracture network connectivity.

2.1 Introduction

In low-porosity carbonate reservoirs, fractures and karstic features have a significant impact on fluid flow, affecting both reservoir performance and forecasting (e.g., Biver et al., 2012; Medekenova and Jones, 2014). In this study, the term fracture is used to refer to any open discontinuity of a medium, such as joints, faults, and dissolved stylolites or veins. Karstic features result from the dissolution of carbonate rocks, which often follow structural and sedimentary discontinuities (James and Choquette et al., 1988; Araújo et al., 2021). Our focus here is on the impact of karstic dissolution on fracture enlargement and its effect on fracture network transmissivity.

Fracture systems play a key role in fluid percolation at various scales, including centimeter-scale joints up to kilometer-scale faults (Davy et al., 2010; Hardebol et al., 2015; Araújo et al., 2021). Open and connected fractures (even when they are filled with relatively permeable material) greatly increase the transmissivity of fracture networks (Nelson, 2001), because they are primarily responsible for the circulation of fluids in rocks with a low-permeability matrix. As a result of concentrating fluid flow, fractures also facilitate karstification processes in carbonate rocks (Cazarin et al., 2018; Bagni et al., 2020; Araújo et al., 2021). In fact, enlargement of fracture apertures due to karstic dissolution might increase network transmissivities by several orders of magnitude (Kaufmann, 2003; Wang and Yu., 2018), thus improving rock transport properties and, consequently, reservoir productivity (Bourdon et al., 2004).

Despite their relevance in the oil industry, karstic features in general are underestimated in the development of reservoir models due to the complexity and variability of their forms (Bourdon et al., 2004; Burchette, 2012), causing considerable uncertainties in predictive models (Medekenova and Jones, 2014). The resolution of the available seismic images and the presence of few exploratory wells often result in a considerable information gap between seismic and well scales, making the characterization of subseismic fractures and karst a pressing challenge (Burchette, 2012; Gutmanis et al., 2017). In fact, subseismic structures might have a significant impact on fluid flow behavior in a reservoir (Agar et al., 2010; Souche et al., 2012; Bisdom et al., 2017; Yao et al., 2019) and might be incorporated into reservoir models by upscaling processes (Agar et al., 2010), for example. In particular, fracture network transmissivity can vary significantly at the inter-well scale, even in slightly deformed reservoirs, due to variations in the geometric properties and topology of the fractures (Bisdom et al., 2017).

Outcropping rocks which are analogues of oil reservoirs often offer excellent exposures of structural and sedimentary features. Detailed studies of outcrops might improve assessment and modeling of oil reservoirs, thus contributing to reduce uncertainties (Gutmanis et al., 2017; Ghosh et al., 2018; Giuffrida et al., 2019; Siddiqui et al., 2020). For example, it is quite difficult to obtain information about fracture connectivity in oil reservoirs. In this case, information from outcrop analogues is essential (Zeeb et al., 2013; Becker et al., 2018). Thus, one way to better understand fracture networks on subseismic scales is through the study of outcrops, because geometric properties of these networks can be directly measured (Ennes-Silva et al., 2016; Menezes et al., 2020; Bagni et al., 2020). In particular, the resulting information can be used to develop deterministic and stochastic Discrete Fracture Network (DFN) models (e.g., Hardebol et al., 2015; Giuffrida et al., 2019, 2020; Massaro et al., 2019). Given a background medium (a layer cake, for example), a DFN incorporates different fracture sets in the medium, thus composing a model that simulates a fractured reservoir (Lei et al., 2017). DFN models can be built directly from geological mapping (deterministic approach) or by stochastic and geomechanical simulations (Lei et al., 2017). However, DFNs studies, even in carbonate rocks, often focus on modeling just the fracture network, thereby neglecting the presence of fracture enlargement due to karstic dissolution.

The objective of this study is to construct a DFN model using a deterministic approach that incorporates fracture enlargement due to karstic dissolution, composing what is referred to as a DFKN (Discrete Fracture and Karst Network) model. The DFKN model represents then a static model of a carbonate reservoir with a karstified fracture network that can be used as input for fluid flow simulations. In this first approach, we study two-dimensional (2D) distributions of subvertical fractures using structural and statistical characterizations of two large outcrops in the Jandaíra Formation, which is an intensely karstified carbonate platform in the Potiguar Basin, Brazil (Fig. 1). The outcropping karstified fracture networks are used as analogs of oil reservoirs, at least from a structural-geometrical perspective.

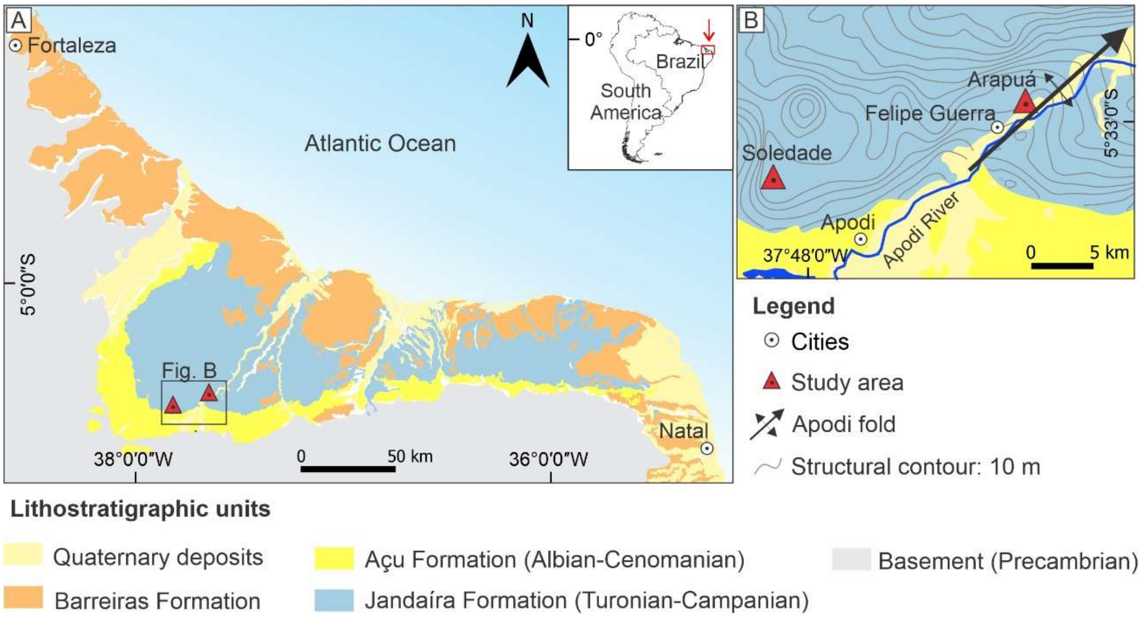

Figure 1: A) Simplified geological map of the Potiguar Basin, modified after Angelim et al. (2006), indicating the location of the Soledade and Arapuá outcrops. B) Local geological context of the two studied outcrops with respect to the Apodi anticline (modified from Bagni et al., 2020).

Due to the semiarid climate of the region, the epigenetic karst system of the Jandaíra Formation is very well preserved, exposing excellent outcrops that allow multiscale studies of karstic features (e.g., Fernandes et al., 2015). We integrate images from Unmanned Aerial Vehicles (UAVs) and field data to construct DFKN models that cover three orders of magnitude of fracture length and aperture, including the effect of fracture enlargement caused by karstic dissolution. Our results might contribute to a better understanding of the behavior of oil reservoirs containing karstified fracture networks.

2.2 Geological setting

2.2.1 Main structures and stratigraphy of the Potiguar Basin

The Potiguar Basin is located on the equatorial margin of Brazil (Fig. 1A). This basin has both onshore and offshore parts, which are associated with the opening of the South Atlantic Ocean during the Jurassic-Cretaceous Period (~160-120 Ma). The main rupture event occurred in the Cretaceous (~130 Ma) (Matos, 1992, 2000). The onshore part is comprised of a syn-rifted, NE-oriented graben and horsts formed under a WNW-ESE-oriented extension of the Lower Berriasian/Upper Barremian (Chang et al., 1988; Matos, 1992).

The stratigraphic record of the Potiguar Basin includes sedimentary units of the rift and post-rift phases (Matos, 1992; Pessoa Neto et al., 2007). Of particular interest to this study is the post-rift Albian phase in which the tectonic regime was controlled by thermal subsidence and continental drift. In this phase, transgressive-regressive cycles of sediments include the Jandaíra Formation (Pessoa Neto et al., 2007).

2.2.2 Jandaíra Formation and associated karstified fracture networks

The Jandaíra Formation is a Turonian-Campanian carbonate platform, which has a maximum thickness of 600 m and overlaps the siliciclastic rocks of the Açu Formation (Pessoa Neto et al., 2007). The Jandaíra Formation encompasses rock types ranging from mudstones to bioclastic and intraclastic grainstones, with rare intercalations of sandstones, shales, marl, and evaporites deposited in systems of tidal plains, shallow lagoons, shallow platforms, and open sea (Córdoba, 2001).

Due to tectonic uplifts and eustatic variations, this carbonate platform was subjected to four episodes of subaerial exposure, represented by the unconformities of the

Upper Turonian, Upper Santonian, Upper Campanian, and a Late Cenozoic exhumation (Miocene-recent) (Pessoa Neto et al., 2007; Reis et al., 2013; Bezerra et al., 2020). These episodes promoted an intense karstification that affected the carbonate rocks of the Jandaíra Formation (Silva et al., 2017). In particular, the karstified fracture networks that we investigate have fractures enlarged by the fourth and most recent phase of karstification (Miocene-recent).

The Jandaíra Formation suffered two post-Campanian episodes of deformation (de Graaf et al., 2017; Bertotti et al., 2017; Bezerra et al., 2020). The first and main episode is characterized by a Campanian to Miocene N-S-oriented compression and an E-W-oriented extension (Bezerra et al., 2020). During this event, the carbonates of the Jandaíra Formation were completely cemented after early diagenesis, and the circulation of fluids was practically restricted to fracture networks (de Graaf et al., 2017; Bertotti et al., 2017).

The second and most recent event of deformation (Miocene-Quaternary) is characterized by an E-W-oriented compression and a N-S-oriented extension, in the eastern part of the basin, and a NW-SE-oriented compression and a NE-SW-oriented extension, in the central and western parts of the basin (Bezerra et al., 2020). This event formed new veins and stylolites, which were later dissolved and enlarged by the last karstification process above referred (de Graaf et al., 2017; Bertotti et al., 2017; Bagni et al., 2020; Araújo et al., 2021).

Karstification in the Jandaíra Formation is essentially epigenic and has an important structural control associated with post-rift tectonics (Xavier Neto et al., 2008; Silva et al., 2017; Araújo et al., 2021). Isotopic analysis and fluid inclusion data done on calcite veins show that calcite precipitation is associated with a single type of fluid that circulated through the fracture systems. This fluid is meteoric in nature and not seawater (Bertotti et al., 2017). Karstified fracture networks result from the linkage of subvertical structures (stylolites, faults and/or joints) that were dissolved and/or enlarged by dissolution. In addition, sedimentary discontinuities also suffered dissolution, thus contributing to the overall interconnection of a system of secondary porosity (Rabelo et al., 2020; Araújo et al., 2021).

During the above referred second event of deformation, a large-scale anticline, named as the Apodi fold, was formed (Fig. 1B; Bagni et al., 2020). In the hinge of this anticline, a striking NE-SW fracture corridor was implanted, and intense karst activity concentrated along the hinge, resulting in the formation of part of the Apodi River valley (Fig. 1B). According to Bagni et al. (2020), density, length, and aperture of the fractures increase towards the anticline axis, making this region favorable for the creation of high karst porosity and permeability.

We studied two outcrops, named as Arapuá and Soledade, which are located in the western part of the Jandaíra formation (Fig. 1A), in the regional structural domain of the Apodi fold. The Arapuá outcrop occurs near the anticline hinge whilst the Soledade outcrop occurs far from the hinge, in the limb zone (Bagni et al., 2020). We identified three types of fractures in these outcrops: 1) joints, which are open fractures, typically with parallel and flat walls, along which little or no movement is observed (Price, 1966); 2) stylolites, which are serrated features that result from rock compaction processes (Rispoli, 1981), and that, in the studied outcrops, are completely dissolved and open; and 3) veins, which are structures that are completely or partially filled with minerals such as calcite and/or quartz (Peacock et al., 2016). Sometimes it is difficult to identify precisely the type of open structure because their distinctive characteristics may have been obliterated by advanced stages of karstic dissolution (Araújo et al., 2021). We then use the term fracture to designate any open discontinuity of the medium.

It is important to emphasize that the precise physical and chemical processes that triggered the karstic processes of the Jandaíra Formation are not relevant to our study. We evaluated just the impact of karstic dissolution on the geometric properties of the fracture networks, particularly fracture enlargement. In this strict sense, the results can be applied to any karstified fracture network, because fracture enlargement can occur either in epigenetic or hypogenic karst systems.

2.3 Methods

This research was developed through an integrated and multidisciplinary approach using fieldwork and Unmanned Aerial Vehicle (UAV) imagery. The objective was to characterize the macro- and mesoscale fractures and the impact on these fractures of karstic dissolution (Fig. 2). We used a multiscale approach that covers approximately three orders of magnitude of fracture length (from 1 m to 1000 m) and five orders of magnitude of aperture (from 0.01 mm to 1000 mm). The collected data allowed us to establish statistical relationships, such as scale laws, that characterize the probability distributions of fracture length and aperture, considering the effects of fracture enlargement due to dissolution. Such statistical relationships constitute the inputs used to modify the DFN model to account for fracture enlargement, resulting in the final DFKN model. Below, we provide general information on the materials and methods used; more specific approaches are characterized together with the acquired data.

2.3.1 Aerophotogrammetry

For the acquisition of aerial images, we used the DJI Phantom 4 Pro UAV, which has a resolution of 20 megapixels. The images were obtained from flights with average heights of 15 and 70 m from the ground surface, with spatial resolutions of 0.5 cm/pixel and 3.5 cm/pixel, respectively. A longitudinal and lateral overlap of 85% between the flight tracks reduced the loss of information in the orthomosaics and increased the quality of the images. To process the UAV images, we used the Agisoft PhotoScan software. Orthomosaics were used in this study for interpretation and quantitative analysis of the geometrical parameters of the karstified fracture networks. Fractures were extracted and quantified using both manual and automated approaches in the Quantum GIS and FraqPaQ softwares.

2.3.2 Scanlines

We performed scanlines both in field and using UAV images to analyze the karstified fracture networks. We performed eight field scanlines at the Soledade outcrop (Fig. 2A) and five field scanlines at the Arapuá outcrop (Fig. 2B), completing a total of 186 m of survey. The field scanline directions were selected to cross the main sets of fractures. The fracture attributes that were measured and effectively used were: distance of the fracture from the origin, fracture length, aperture, dip angle, direction, type of termination, type of infilling (if present), karstified aperture, and fracture type (joint, vein, or stylolite). Several aperture measurements were made along the same fracture to quantify the impact of karstic dissolution on the aperture values.

Seven digital scanlines on the UAV images were also measured, resulting in a total of 612 m of survey. Compared to the field scanlines, digital scanlines can be placed anywhere but have limitations both on aperture resolution (only fracture apertures higher than 8 mm could be measured) and fracture type characterization. For example, the dip angle could not be measured. Based on field data, we assume that all fractures are subvertical (Fig. 3). Under this hypothesis, the 2D analysis is sufficient to characterize the fracture networks because connectivity relationships observed on the surface can be safely extrapolated to the subsurface.

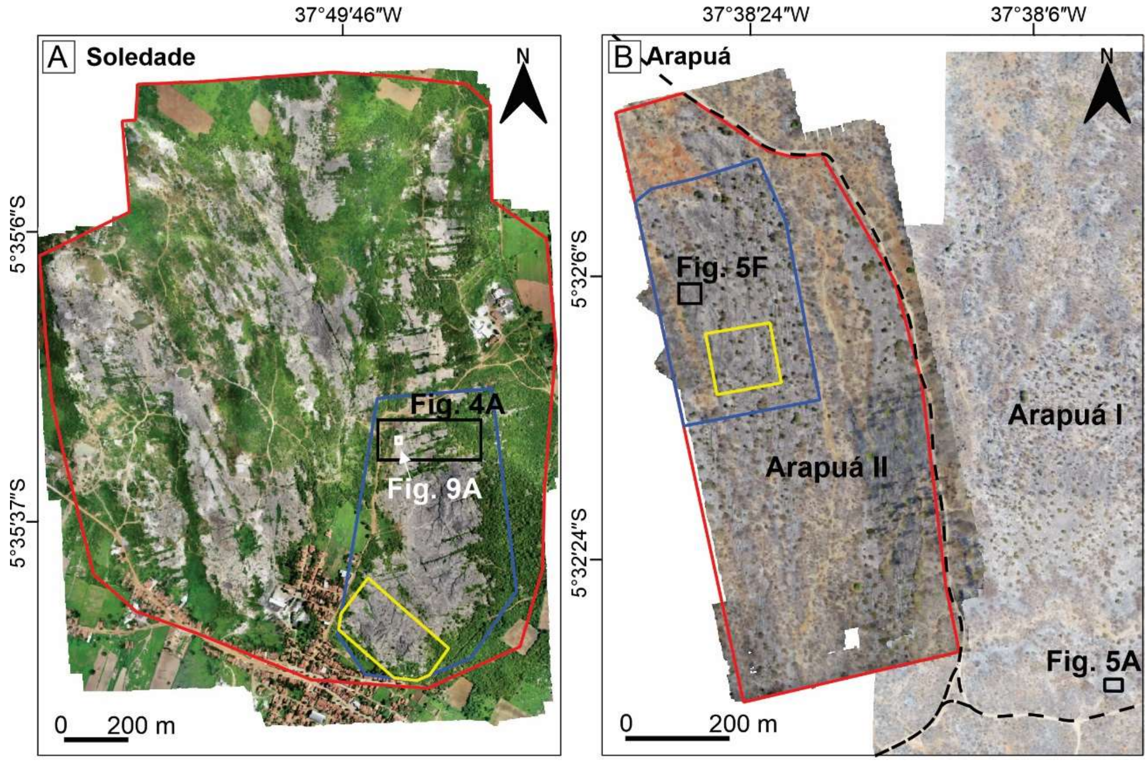

Figure 2: General view of the two outcrops. In Soledade (A) and Arapuá (B) outcrops, the polygons in red, blue, and yellow identify the subareas used for the multi-scale statistical characterization of fractures (see details in the text and in Fig. 6).

2.3.3 Discrete modeling of the fractures including fracture enlargement

The final deterministic DFKN model incorporates a karstified fracture network, which can be used as a static model for fluid flow simulations. The main advantage of the deterministic approach to build a DFN is to preserve the field geological characteristics (e.g., geometrical properties) (Lei et al., 2017). To simulate the influence of karstic dissolution on fracture enlargement, that is, to build different DFKN models of the same fracture network in different scenarios of karstic dissolution, we modified the fracture apertures obtained in the scanlines to simulate different stages of dissolution. DFKN modeling was performed using the FracaFlow software from Beicip-Franlab, which was developed to characterize and model fractured reservoirs.

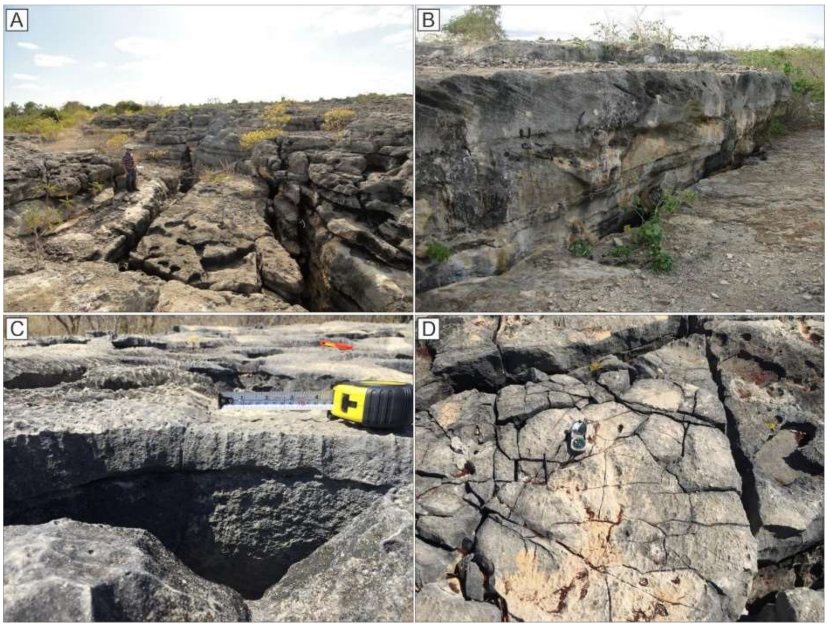

Figure 3: Photographs showing that most fractures both in Soledade (A and B) and Arapuá (C and D) outcrops are subvertical.

The area used in the DFKN modeling was the Soledade outcrop, to be detailed later. For the static modeling, the Jandaíra Formation was represented by a medium with a constant thickness, without considering its internal stratification (Massaro et al., 2019). For the development of the deterministic model, three groups of subvertical fractures were used and defined by lengths in the ranges of 1 - 10 m, 10 - 100 m, and 100 - 1000 m. The fractures were extracted from the UAV images, and, in addition to the parameters of length, spacing and direction, aperture variation as a function of karstic dissolution degree was also considered and incorporated into the model.

2.4 Qualitative analyses of stratigraphic and structural framework

The carbonate rocks comprising the studied outcrops were identified as grainstones and bioclastic packstones based on macroscopic analyses. These rocks ranged from medium to very coarse grained in size, with a moderated to well-selected sorting degrees. The main sedimentary structures included planar cross stratifications, planar parallel stratifications, and bioturbations, indicating a marine system dominated by high- and low-energy conditions (Córdoba, 2001; Santos Filho et al., 2015). The identified bioclasts included ostracods, gastropods, foraminifers, bivalves, ooids, and peloids (Tibana and Terra, 1981; Santos Filho et al., 2015). The carbonate rocks formed centimetric- to metric-scale subhorizontal beds, which dip very smoothly to the northeast. The subhorizontal boundaries between some layers exhibit high degrees of dissolution/karstification due to epigenetic fluid percolation (Araújo et al., 2021). As previously described, the fractures exposed in the Soledade and Arapuá outcrops can be joints, and dissolved stylolites or veins. All these fractures are subvertical, often appear open and do not contain infillings, except for the veins, as shown in Fig. 3.

2.4.1 Soledade outcrop

The identified structures include mostly subvertical stylolites and, less frequently, subvertical joints and veins. Subvertical stylolites occur in almost all directions (Fig. 4D), although they occur most frequently in the E-W to ESE-WNW directions. In addition, the ENE-WSW set often presents the longest fractures, which can exceed 100 m in length (Fig. 4A). In turn, the subvertical joints strike N-S to NNE-SSW, NE-SW, E-W, and NW-SW (Fig. 4E). Finally, the veins -strike mostly N-S to NNE-SSW, with secondary sets striking in the E-W and NNW-SSE directions (Fig. 4F). The abutting and crosscutting relationships of the structures are inferred from the field analyses (Figs. 4B and C). In particular, the ENE-SSW and E-W stylolite sets show mutual abutting and crosscutting relationships with the N-S and NW-SE striking joint sets (Figs. 4B and C).

2.4.2 Arapuá outcrop

This outcrop presents two fracture patterns, which form two structural subdomains: Arapuá I (Fig. 5A) and Arapuá II (Fig. 5F). The first presents an orthogonal system of fractures, whereas the second is dominated by an apparent conjugate system of fractures. Both Arapuá I and II subdomains present intensely karstified fractures.

In Arapuá I, the subvertical stylolites strike mostly E-W, with secondary sets striking NE-SW, NW-SE, and NNW-SSE (Fig. 5C). The subvertical joints mostly strike the N-S, NNW-SSE, and NNE-SSW directions (Fig. 5D). The calcite veins exhibit a well-defined main orientation ranging from the N-S to NNE-SSW directions (Fig. 5E). The N-

S striking joint set and the E-W striking subvertical stylolites crosscut each other (Figs. 5A and C).

In Arapuá II, few subvertical stylolites are observed, and they strike NNE-SSW and NNW-SSE (Fig. 5H). The subvertical joints strike mostly NNE-SSW and NW-SE and form the low-angle conjugate pair that characterizes the outcrop (Fig. 5F and I). The veins, as seen in Arapuá I, strike N-S to NNE-SSW (Fig. 5J). The N-S joint and the NW-SE joint sets are coeval (Fig. 5G).

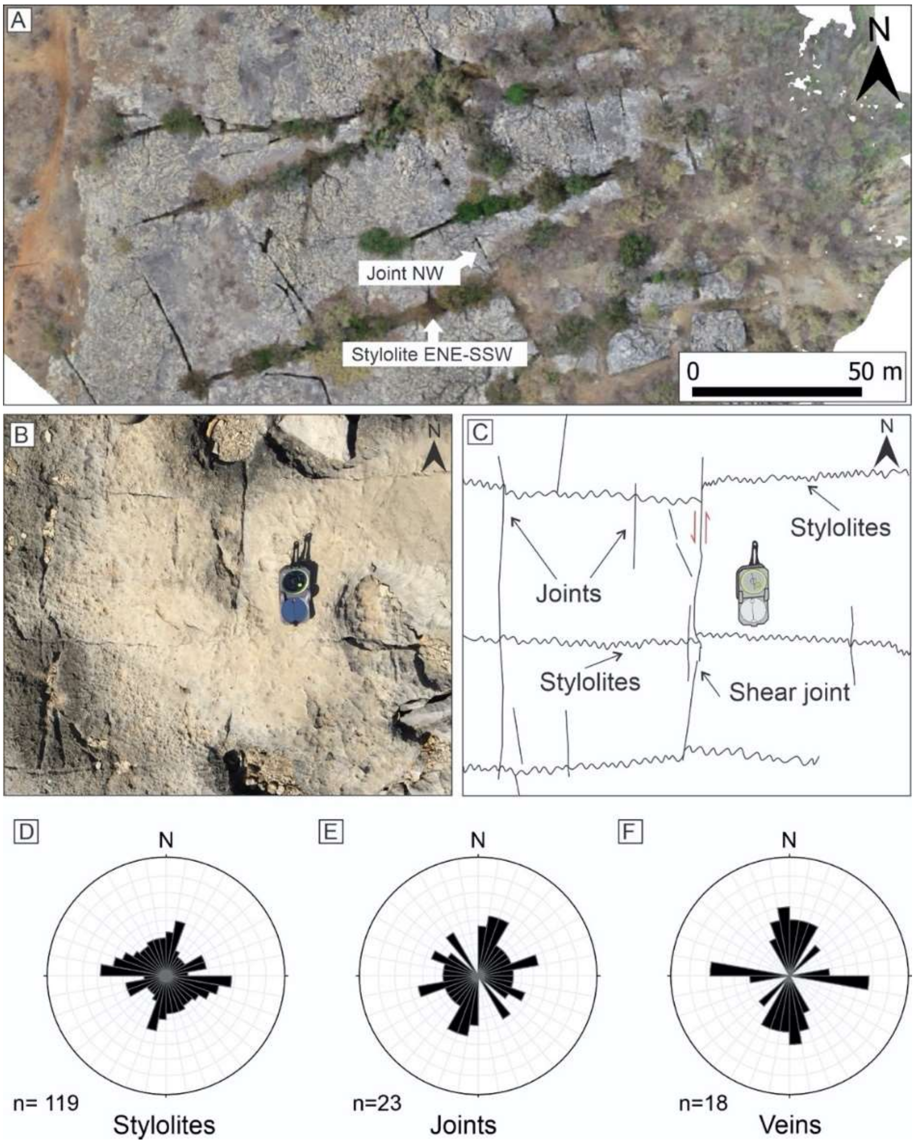

Figure 4: Soledade outcrop. A) UAV image showing ENE-WSW striking stylolites, which can exceed 100 m in length and cross the NW-SE striking joints. B) Close-up view showing the mutual abutting and crosscutting relationships between the E-W striking

stylolites and the N-S striking joints. C) Line drawing of B detailing the termination relationships between the stylolites and joints. D to F) Rose diagrams of the stylolite, joint and vein sets. Fig. A is located in Fig. 2A.

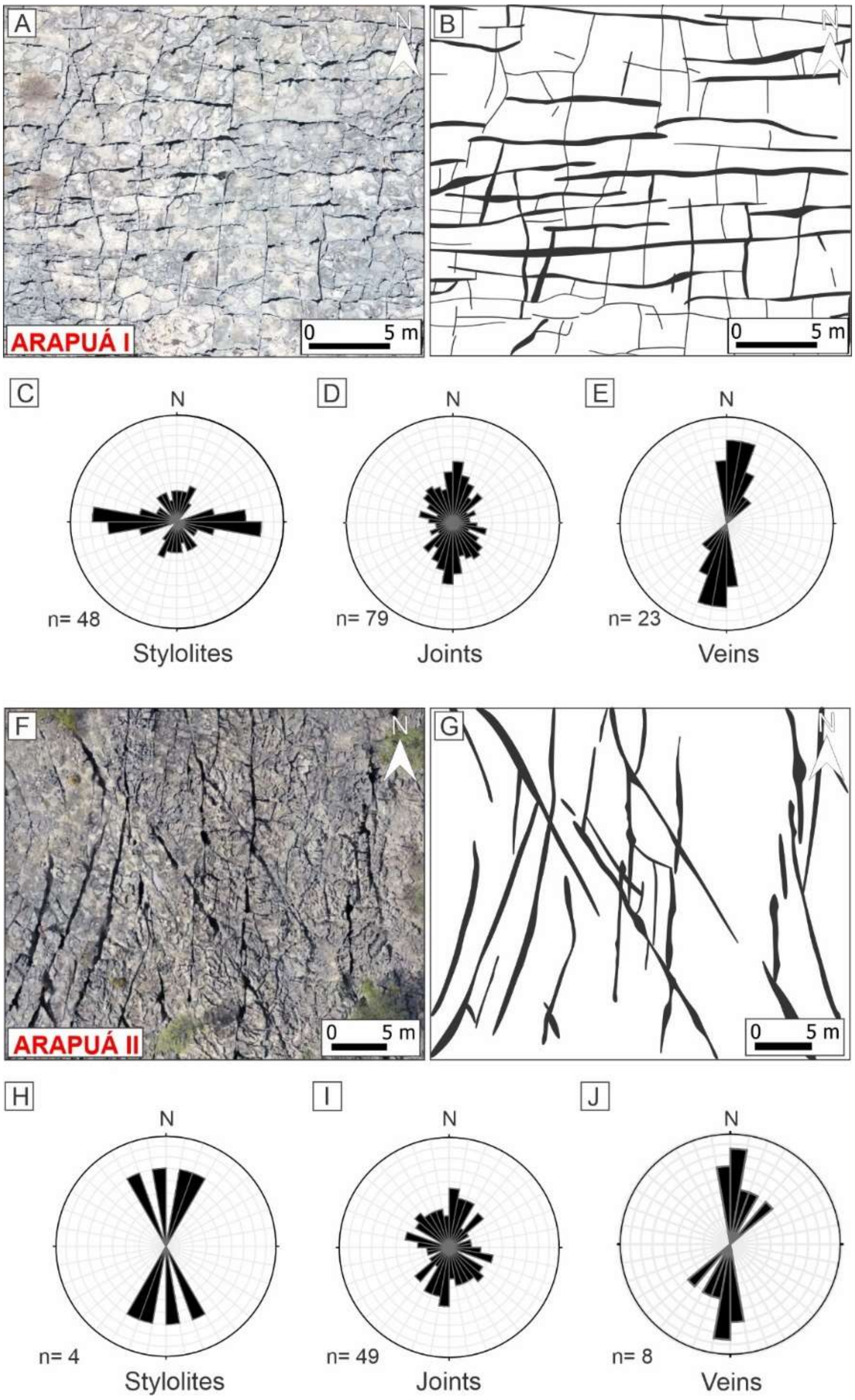

Figure 5: Arapuá outcrop. A and F) UAV images showing the two patterns of fractures in the outcrop. In Arapuá I subdomain (A), abutting and crosscutting relationships of the

N-S joints and E-W striking stylolite sets form an orthogonal geometry, whilst in Arapuá II subdomain (F), fractures form an apparent conjugate pair of sets. B and G) Line drawings highlighting the termination relationships between fractures. C) to E) and H to J) Rose diagrams of stylolites, joints, and vein sets of the two subdomains. Figs. A and F are located in Fig. 2B.

2.5 Quantitative analyses of the karstified fracture networks

2.5.1 Analysis of fracture length

2.5.1.1 Manual collection of fracture length data

This dataset was collected from the UAV images in the Soledade and Arapuá outcrops to test if the probability distributions of fracture length can be described by power laws. Three subareas of different sizes were chosen (Fig. 2). Note that the largest subarea (in red) contains the intermediate-sized subarea (in blue), which in turn contains the smallest subarea (in yellow). This zoom-in strategy makes the manual work of measuring lengths feasible and maintains the hypothesis that the fracture lengths measured at the three different scales belong to the same structural setting. To provide an overlap of the three different length ranges, allowing us to duplicate the measurements at length transitions, we measured fractures with lengths between 50 and 1000 m (largest subarea; Fig. 6A and B), 5 and 200 m (intermediate subarea; Fig. 6C and D), and 0.5 and 20 m (smallest subarea; Fig. 6E and F). The dimensions of the subareas and the number of fractures counted are shown in Table 1.

The probabilities of fracture length occurrence are shown in Figs. 7A and B. For each outcrop, the curves for the three subareas were jointly normalized so that they could be viewed as a single probability curve (Pickering et al., 1994). Both outcrops presented similar distributions for the sampling probability of fracture length. In particular, the approximate parallelism of the curves in each outcrop, obtained at the three scales, revealed that the statistical distributions of the fractures follow power laws.

2.5.1.2 Automatic collection fracture length data

To confirm the reliability of the manually sampled probability curves (Figs. 7A and B), we used the FracPaQ software (Healy et al., 2017) to collect fracture lengths automatically in the smallest subarea of the outcrops (Figs. 6E and F). The probability curves of the fracture lengths are also shown in Figs. 7C and D. The practical overlap of the probability curves resulting from manual and automatic collections validate both procedures.

2.5.1.3 Fitting the sampled probabilities with power laws

The probability density function $p(l)$ approximating the sampled probability of the fracture lengths in the interval $[lmin, lmax]$ can be fitted by the power law:

$$p(l) = \beta\, l^{-\alpha} \qquad (1)$$

where l is a generic length and β and α are the density and exponent parameters, respectively (Davy, 1993; Bonnet et al., 2001).

The sampled probability curves were fitted with power laws (Figs. 7C and D) using FracPaQ (Table 2) because this software employs a robust approach to the estimation process. As a result, the censoring and truncation effects in the estimated power law parameters are attenuated. Within the identified length limits (Figs. 7C and D), the probabilities of occurrence of fracture length of the Soledade and Arapuá outcrops can be fitted by power laws with exponents α equal to 2.22 and 2.66, respectively (Figs. 7C and D and Table 2). The high correlations obtained for the fittings in both cases (Table 2) demonstrate the good adherence to the power law of the two datasets.

Table 1: Area sizes and number of fractures counted in each subarea of the Soledade and Arapuá outcrops in the manual collection of fracture lengths.

	Soledade		**Arapuá**	
Length range	Interpretation area (km²)	Number of fractures	Interpretation area (km²)	Number of fractures
50-1000 m	2.625	230	0.502	149
5-200 m	0.404	743	0.125	1145
0.5-20 m	0.062	1102	0.016	1574

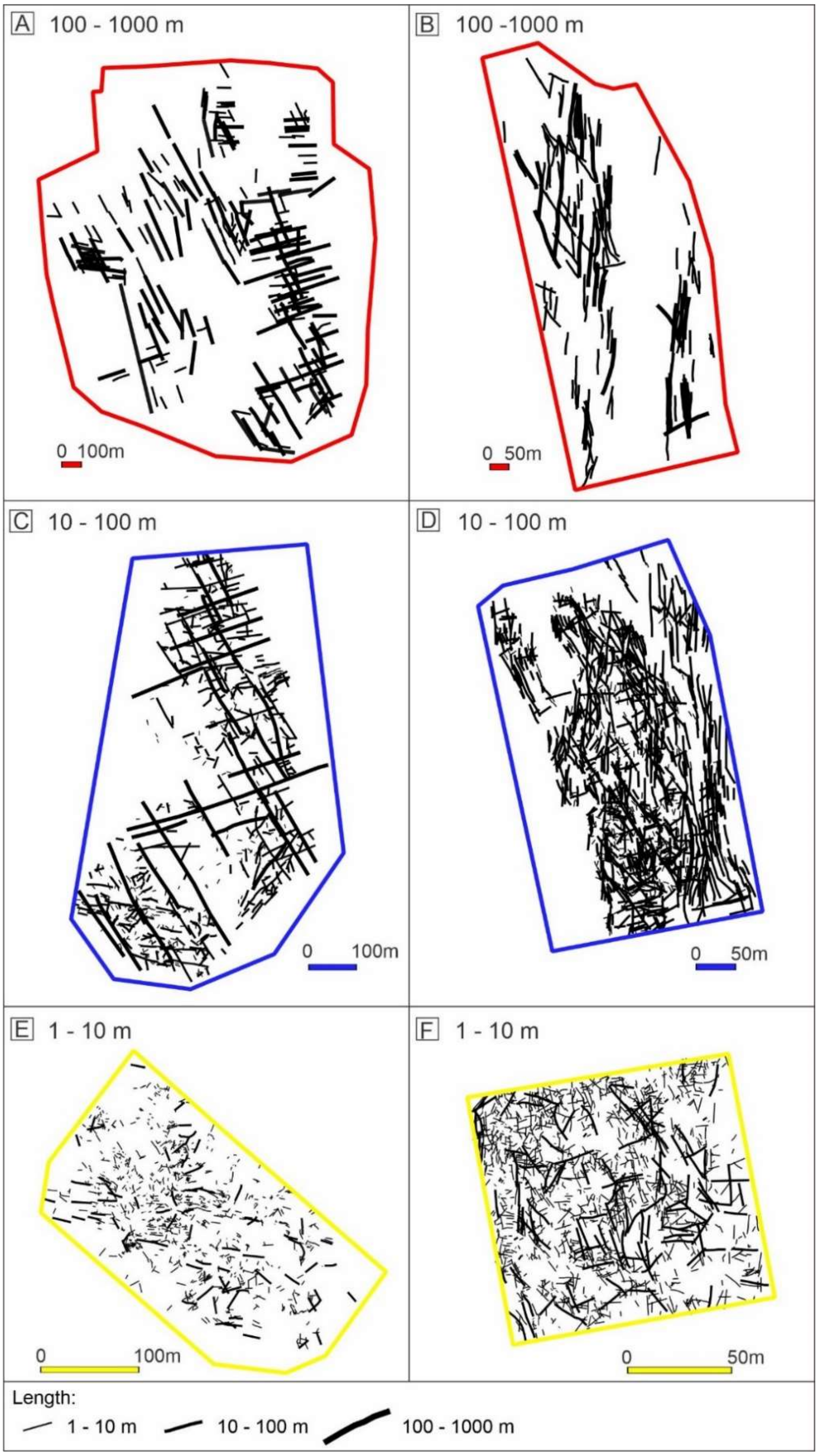

Figure 6: Soledade (left column) and Arapuá (right column) outcrops. A) to F) Subareas used to characterize fractures with lengths between 50 and 1000 m, 5 and 200 m, and 0.5 and 20 m in both outcrops. Note that there is an overlap (or duplication) of the fracture

length measurements, in the transition from a larger scale to the subsequent smaller scale, in order to better characterize the three coverage scales (1-10 m, 10-100 m, and 100- 1000 m). See details in the text and in Fig. 7.

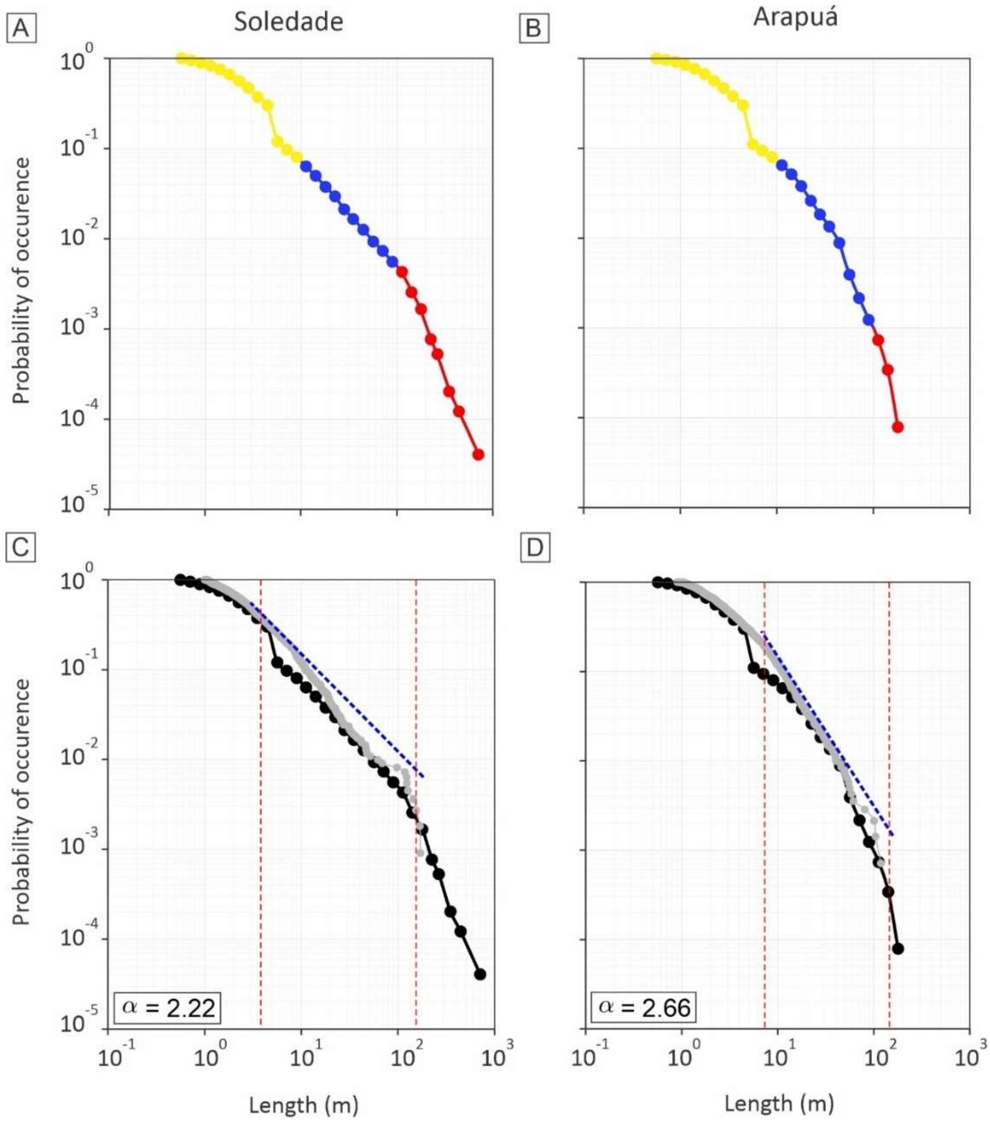

Figure 7: Soledade (left column) and Arapuá (right column) outcrops. A and B) Probability curves for fracture length resulting from manual sampling; the sampling probabilities were normalized. To calculate the probabilities, manual count of fractures were done in each of the three sampling intervals of length: from 0.5 to 20 m (in yellow), from 5 to 200 m (in blue) and from 50 to 1000 m (in red). C and D) Comparison between the curves extracted manually (in black) and automatically through the FracPaq software

(in gray). In (C) and (D)Power laws (dotted lines in blue) were fitted with the FracPaq software and the vertical lines (in dotted red) show the approximate limits of sampling validity imposed by the effects of truncation and censoring.

Table 2: Estimates of the power law parameters fitting the probability curves of the Soledade and Arapuá outcrops obtained with the FracPaQ software.

Outcrop	**Area (m²)**	**Number of fractures per interval**			**Estimated parameters**				
		1-10 m	10-100 m	100-1000 m	Upper limit (m)	Lower limit (m)	Exponent α	Fracture Density P_{21} (m^{-2})	Correlation coefficient
Soledade	64484	980	119	9	121	3.8	2.22	0.025	84%
Arapuá	15616	1226	180	5	-	7.0	2.66	0.160	98%

2.5.2 Connectivity analysis of the fracture networks

The small subareas (Figs. 6E and F) of each outcrop were used to analyze the connectivity of the fracture networks based on the obtained percolation backbones (Fig. 8). The backbone is composed only by the fractures that are connected within a network. That is, the backbone is the resulting network after all "dead ends" fractures are removed (Odling et al., 1999; Manzocchi, 2002). Although topology is widely used for connectivity analysis of fractured systems (Manzocchi, 2002; Sanderson and Nixon, 2018), we chose the backbone approach to test the validity of the correlation, proposed by Bour and Davy (1997), between backbone complexity (including the relative importance of different fracture lengths) with the value of the power law coefficient, as described below.

The fracture networks of the Soledade and Arapuá outcrops show very different backbones, and consequently very different connectivities. In the Soledade outcrop, the backbone is formed mainly by long fractures (Fig. 8A), whilst in the Arapuá outcrop, the backbone is much more complex; in this case, there are contributions from all fracture lengths (Fig. 8B). Following Bour and Davy (1997), this difference in the backbones can be related to the fitted power-law exponent α (equation 1), which controls the fracture length distributions: the smaller α is, the greater the influence of long fractures on the connectivity. In fact, in the Soledade outcrop, α is equal to 2.22 (Fig. 7C), whilst in Arapuá, α is equal to 2.66 (Fig. 7D). In accordance, we found fewer fracture intersections in the Soledade outcrop (125 connected nodes) than in the Arapuá outcrop (1053 connected nodes), although the sampled area is larger in Soledade than in Arapuá (Fig. 8). These findings are in accordance with the numerical simulations of synthetic fracture networks done by Bour and Davy (1997), which predict the number of fracture intersections based only on the exponent α. Note that although the difference between the two exponents appear to be not large, they are in the range of $2 < \alpha < 3$, which is a critical interval where the curve estimating the number of intersections per fracture is very sensitive to exponent variations (Bour and Davy, 1997).

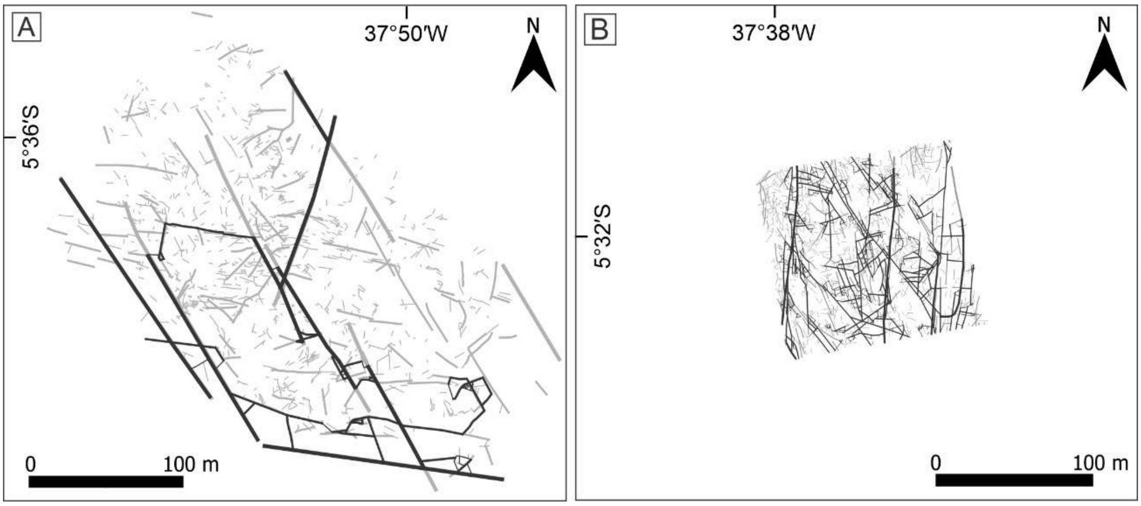

Figure 8: Backbones of the fracture systems of the Soledade (α = 2.22) (A) and Arapuá (α = 2.66) (B) outcrops. Note that the scale in both figures is the same. Rectangles in Figs. A and B refer to the yellow subareas located in Fig. 2A (Soledade) and 2B (Arapuá).

The contrasts in the connectivity of the fracture networks are conditioned by the distance of the outcrop in relation to the Apodi fold (Fig. 1B): a higher fracture density is expected closer to the fold axis (Bagni et al., 2020). In fact, the fracture density of the Arapuá outcrop is approximately six times greater than that of the Soledade outcrop (Table 2). A higher fracture density has a direct impact on the karstic dissolution of the fractures: the higher the connectivity is, the easier the percolation of fluids will be (Odling et al., 1999; Bagni et al., 2020), thus contributing to increase karstic dissolution in Arapuá, a fact that is verified by both field data and UAV images (Figs. 4A; 5A and F).

2.5.3 Fracture aperture analysis

To characterize the impact of karstic dissolution on fracture apertures, we used the information collected by both field surveys and digital scanlines to perform the following analyses: to classify the apertures according to their karstification degree, to correlate the aperture values with fracture directions, to characterize the probability of occurrence of fracture apertures and, finally, to obtain the relationships between fracture aperture and length. Each one of these analyses is detailed below. We stress that only open fractures were used. In total, 151 fractures in the Soledade outcrop (128 and 23 resulting from field and digital scanlines, respectively) and 120 fractures in the Arapuá outcrop (111 and 9 resulting from field and digital scanlines, respectively) were analyzed. The aperture values obtained from the digital scanlines were used to complement the field data, allowing us to incorporate data from fractures with lengths greater than 100 m. We also emphasize that several measurements of aperture were done along the same fracture, totalizing 1137 measures of aperture.

2.5.3.1 Aperture classification according to the karstic dissolution degree

Due to karstic dissolution, the studied fractures may present varied apertures. Aperture variation can occur from one fracture to another and even along the same fracture (Fig. 9A). The variation in the aperture values is caused by mechanical effects during fracture formation, besides karstic dissolution that occurs over time (Bonnet et al., 2001; Wennberg et al., 2016).

In the literature, aperture values associated with non-karstified and karstified fractures are not well established. Indeed, the chosen average values depend on the applied methodology, type of fracture, and objective of the research. Wennberg et al. (2016), for example, analyzed partially dissolved fractures in rock analogs of carbonate reservoirs, adopting aperture values of 0.3 mm and 3.5 mm for non-karstified and karstified fractures, respectively. An additional example is given by Fournillon et al. (2017) from a field survey carried out in the Rospo Mare oil field (Adriatic Sea). In this case, the apertures of karstified fractures, although unknown, were assumed to be in the interval from 50 mm to 200 mm.

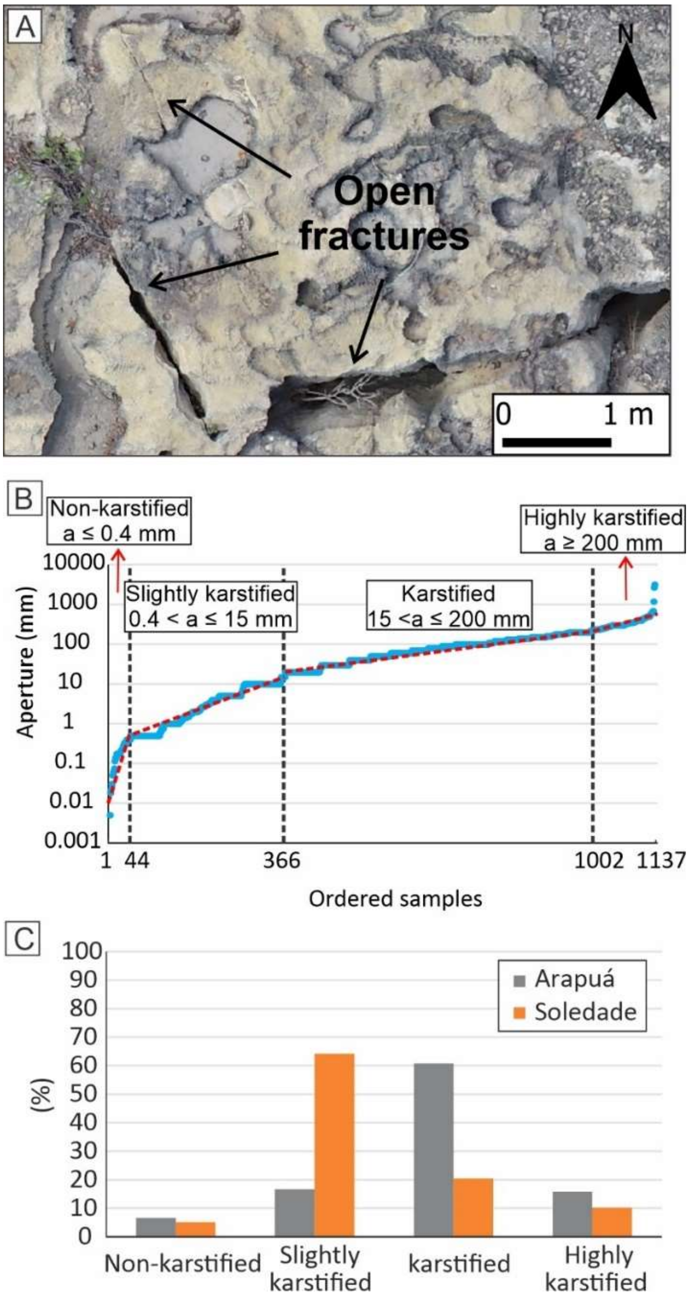

Figure 9: A) UAV image of the Soledade outcrop showing that aperture varies along the same fracture due to changes in karstic dissolution. Image A is located in Fig. 2A. B) Classification of the fracture apertures into four groups according to their degree of karstic dissolution. The aperture values resulted from all field scanlines measured in Soledade and Arapuá outcrops. A total of 1137 measured apertures were ordered from the lowest to the highest value of aperture. The four red dashed lines show a piecewise linear approximation of the actual increase in the aperture values. On the hypothesis that each piecewise linear part represents one degree of karstic dissolution, we classify the apertures

into four groups: non-karstified, slightly karstified, karstified, and highly karstified. The respective aperture intervals are shown in the figure. C) Percentage of fractures according to the degree of karstic dissolution in the Soledade (in orange) and Arapuá (in gray) outcrops.

The fracture apertures measured in the Soledade and Arapuá outcrops are listed together in ascending order in Fig. 9B. Note that the variation covers more than five orders of magnitude. We approximate this graph with a piecewise linear curve showing the smallest number of parts. Then, we classify the apertures based on the intervals in which each linear behavior by parts is valid. As a result, fractures are classified into four groups: non-karstified (≤ 0.4 mm), slightly karstified (0.4 - 15 mm), karstified (15 - 200 mm), and highly karstified (≥ 200 mm). The average apertures for each fracture group were calculated and the results are shown in Fig. 9C. It can be seen that in the Soledade outcrop, most fractures are slightly karstified, whilst in the Arapuá outcrop, most fractures are karstified (Fig. 9C), a result that is consistent with the visual analyses of the two outcrops (compare Fig. 4A with Fig. 5A, for example).

2.5.3.2 Aperture distribution by direction

The average apertures resulting from the field scanlines (using fractures up to 60 m in length) were plotted in polar graphs to verify the effect of karstic dissolution on each direction set (Fig. 10). We stress that the average apertures were calculated considering the variation of the aperture along the length of the same fracture.

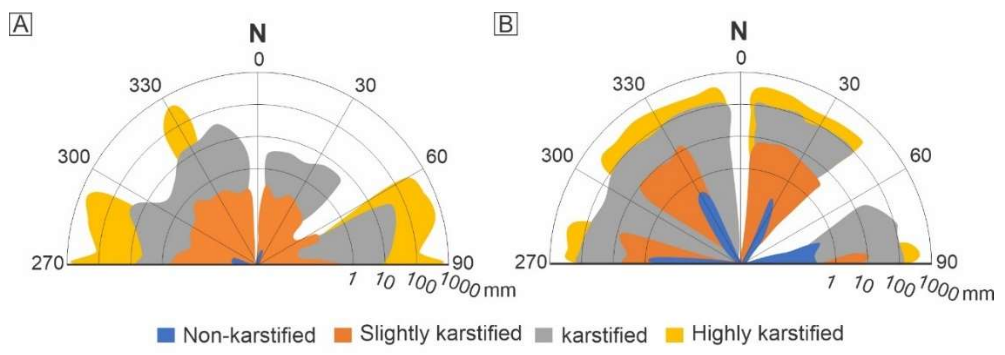

Figure 10: Distribution of the mean values of fracture aperture by direction in the Soledade (A) and Arapuá (B) outcrops.

In the Soledade outcrop, although karstic dissolution occurs in all directions, it mainly affects the ENE-WSW-, E-W-, and NW-SE-striking fracture sets; these three sets show aperture averages up to 800 mm (Fig. 10A). On the other hand, in the Arapuá outcrop, the aperture distribution per direction is more homogeneous. In particular, intensely karstified fractures are present in all directions (Fig. 10B).

The dependence of aperture distribution with direction is related to the connectivity of the fracture network in each outcrop and has a major implication for the transmissivity of the fracture systems. In the Soledade outcrop, we have already seen that connectivity is controlled by the longest fractures (Fig. 8A); in this outcrop, few connections are present, so the system is more channeled, and therefore, the flow is more concentrated along the long fractures, contributing to the increased dissolution in these structures. This explains the existence of more enlarged fractures in some preferential directions. On the other hand, in the Arapuá outcrop, the connectivity has contributions of fractures of all lengths (Fig. 8B); in fact, there are more connections in this outcrop, and the fracture system is more evenly distributed, thus contributing to a more homogenized dissolution process.

2.5.3.3 Probability of occurrence of fracture apertures

In the previous section, the variation in the aperture along the same fracture was considered. Now, for each fracture length, only one value (an average) is used to relate aperture and length. First, the weighted average of the apertures along the same fracture is calculated, thus resulting in a single aperture value for each fracture. For this analysis, data taken from the UAV images are also included, allowing us to incorporate aperture values of fracture lengths exceeding 100 m. The averages are plotted in bi-logarithmic graphs, which demonstrate that the distribution patterns are not random (Fig. 11), in accordance with the fact that aperture distributions of fracture networks are usually approximated by power laws or lognormal distributions (Hooker et al., 2009; Gong and Rossen et al., 2017).

In the Soledade outcrop, the resulting curve can be fitted by a power law that produces a correlation coefficient equal to 0.92 (Fig. 11A). Note that there are two deviations from the fitted curve, one at approximately 1000 mm and another at approximately 0.265 mm; both deviations are certainly associated with sampling limitations, such as those caused by censoring and truncating effects. Conversely, in the Arapuá outcrop, the resulting curve can be better fitted by an exponential distribution that produces a correlation coefficient equal to 0.98 (Fig. 11B). Apparently, here there are no edge effects, and there is great uniformity in the number of fractures with apertures in the interval ranging from 0.062 mm to 35 mm.

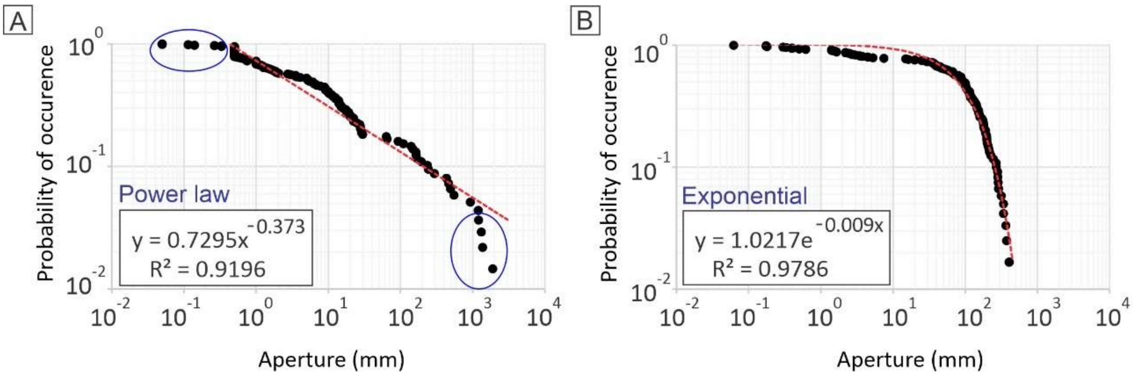

Figure 11: Probability of occurrence of number of fractures according to the mean average apertures for the Soledade (A) and Arapuá (B) outcrops. The red lines correspond to the respective fitted law in each graph: a power law in Soledade and an exponential law in Arapuá. In A), the ellipses (in blue) identify the aperture ranges affected by censoring and truncation effects. In contrast with the Soledade outcrop, in the Arapuá outcrop the probability of occurrence of aperture cannot be described by a power law, as a consequence of its higher degree of karstic dissolution.

2.5.3.4 Aperture-length relationship

Many authors have proposed an approximately linear relationship between the aperture and length of fractures when plotted in bi-logarithmic graphs (e.g., Vermilye and Scholz, 1995; Olson, 2003; Torabi and Berg, 2011; Ghanbarian et al., 2018). This approximation is the mathematical basis for constructing stochastic DFN models (Gong and Rossen, 2017; Lei et al., 2017). Next, we analyze the validity of this approach for the two studied outcrops.

The aperture values are plotted as a function of length for the Soledade and Arapuá outcrops in Fig. 12. In the Soledade outcrop, this distribution can be fitted by a single straight line in the bi-logarithmic graph, which corresponds to an exponential increase in the aperture with length. However, this is not possible in the Arapuá outcrop; in this case, a single straight line might approximately fit the distribution only to fracture lengths less than 1.0 m. For longer fractures, the apertures can be approximated by a constant value regardless of fracture length (Fig. 12B).

We interpret from Fig. 12 that, as karstic dissolution evolves, the power law is gradually broken, this effect evolving from longer to shorter fractures. The break in the validity of the power law relating aperture and length in the Arapuá outcrop can then be attributed to its higher degree of karstic dissolution. This interpretation is in accordance with the fact that karstification has been recognized as an important factor influencing fracture aperture (Kaufmann, 2003; Wang and Yu., 2018). However, we stress that when karstic dissolution degree is relatively low, as in Soledade outcrop, the power law is still approximately valid because aperture-length relationship remains dominated by mechanical origins.

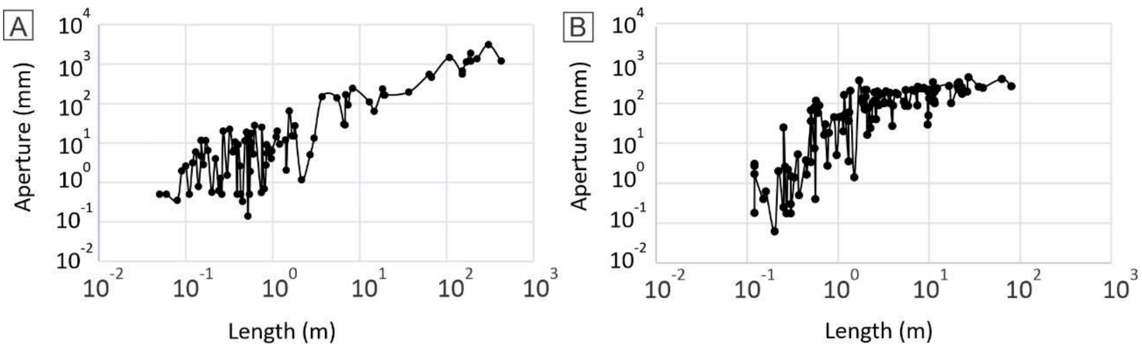

Figure 12: Mean fracture aperture as a function of fracture length for the Soledade (A) and Arapuá (B) outcrops. Note that in (A) the graph can be approximately fitted by a straight line, which is not possible in (B). See text for the implications of this difference for the transmissivities of the fracture networks.

The results presented above introduce a new perspective on how to incorporate the effects of aperture enlargement due to karstic dissolution into stochastic simulations of fractured carbonate reservoirs. These effects can be incorporated in a practical manner by modifying the relationship between aperture and length. Fig. 13 illustrates this approach schematically: the effect of increasing the karstic dissolution degree in a fracture network can be simulated by gradually horizontalizing the curve relating aperture and length plotted in a bi-logarithmic graph. The key benefit of this approach is that it can be readily implemented by just modifying the scale law. The modified curve can then serve as a basis for modeling fractures in a modified DFN model, incorporating the effect of the enlargement of fracture apertures due to karstic dissolution. We refer to the resulting model as a DFKN model. We detail this approach in the following section.

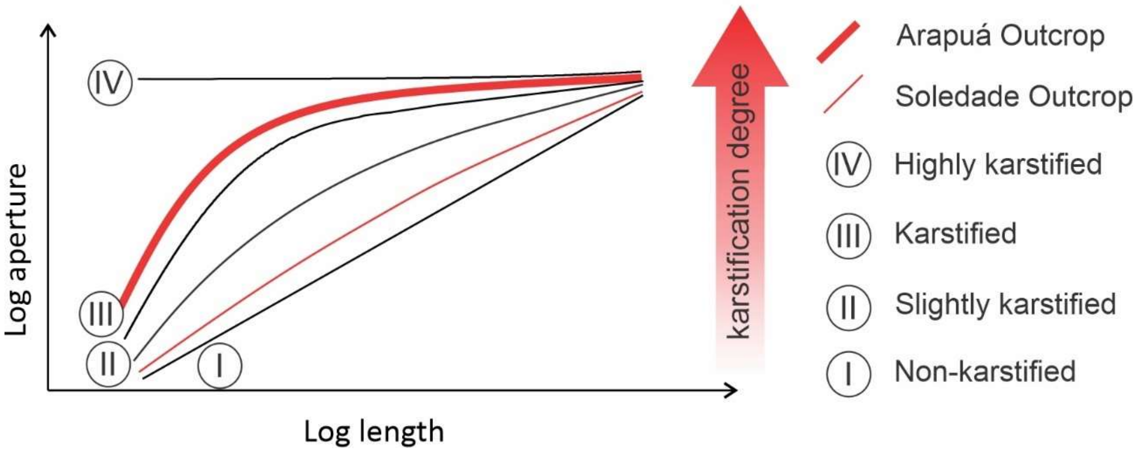

Figure 13: Schematic graph showing how to modify the relationship between fracture aperture and length to incorporate increasing stages of karstic dissolution in oil reservoirs affected by karstified fracture networks. In this scheme, in a non-karstified reservoir (I), the aperture-length curve obeys a power law very well. With the increase in the degree of karstic dissolution, the power law gradually loses its validity, passing through intermediate stages II and III, which approximate the karstic dissolution stages characterized in the Soledade and Arapuá outcrops, respectively. Finally, the aperture-length curve degenerates into a horizontal line (IV), in a very intense end-member stage of karstic dissolution.

2.6 Discrete fracture and karst network (DFKN) models

The impact of karstic dissolution on fractures is very important because intrinsic permeability is proportional to the cube of aperture. This relation is based on the Poiseuille's law and is usually referred to as the cubic law (Lomize, 1961; Snow, 1965; Louis, 1969; Witherspoon et al., 1980). Note that using intrinsic permeability, there is no need to consider the type of fluid because this quantity is based on geometric parameters only.

We chose the Soledade outcrop to build a deterministic DFKN model given that this outcrop has experienced relatively low karstic dissolution and that the power law relating fracture aperture and length is still approximately valid. The DFKN model was built based on the smallest subarea of the Soledade outcrop (Fig. 6E), which is the same subarea used for the automatic collection of fracture lengths. We use all fracture sets interpreted from the UAV images and their aperture values measured from both digital and field scanlines to compose the model.

To simplify the model, we classified the fractures into four fracture sets in the directions N0º (N-S), N49º (NE-SW), N104º (E-W), and N146º (NW-SE). In each direction set, the fractures were grouped into three ranges of length: 1-10 m, 10-100 m, and 100-1000 m. Finally, for each range of length, the fractures were classified into three karstic dissolution degrees, resulting in thirty-six fracture subsets; the percentages in relation to the total number of analyzed fractures (901) are given in Table 3. For each fracture length range, an average aperture was calculated, and the results are shown in Table 4. To calculate the mean apertures given in this table, we adopted the simplified approach of considering that all fractures are open and without any type of infilling. Veins were not included because, according to the field scanlines, their apertures were in the range of 0.05 mm to 2.5 mm, thus covering a range of apertures smaller than the UAV image resolution (approximately 5 mm). In addition, to the other fractures that we could not assign an aperture value due to the limit in UAV image resolution, we attributed aperture values of 6.02 mm (N-S), 1.16 mm (NE-SW), 5.65 mm (E-W), and 4.68 mm (NW-SE), regardless of their length. In detail, these fractures were in the length ranges of 1.0 - 10 m (approximately 15% of the fractures) and 10 - 100 m (only 10% of the fractures). However, according to the cubic law, this simplification has a relatively low impact on the modeling results because the fractures in question have relatively small apertures. In addition, from visual analysis, we observed that they are predominantly isolated.

The average aperture per group of fractures, shown in Table 4, was incorporated into a DFKN model that was constructed using grids with cell dimensions of 100 m x 100 m on the Earth's surface with a constant thickness of 2.5 m (Fig. 14A). To avoid upscaling issues, as FracaFlow does not handle small cell dimensions well, all fracture lengths were multiplied by a scaling factor of 100. An advantage of scaling up the fracture lengths of the Soledade outcrop is that they now have the same dimensions as those of a real oil field reservoir. In addition, all fractures were assumed to be subvertical and to have the same vertical dimension (2.5 m). Although this is a rough hypothesis for the fracture geometry, it is useful in real applications because an oil reservoir is usually confined to a sub-horizontal layer with the vertical dimension much smaller than the horizontal dimension. The other parameters, such as length, spacing, and orientation, were input in the software from the digital UAV images.

The three resulting intrinsic permeability fields in *i* (northeast), *j* (southeast), and *k* (vertical) directions are shown in Figs. 14B-D. These directions correspond approximately to the main directions of the intrinsic permeability tensor (Volatili et al., 2019). Note that in directions *j* and *k*, the largest fractures have the highest intrinsic permeability values, while in direction *i*, both large- and intermediate-sized fractures may have similar permeability values. This highlights the importance of grid direction analysis in reservoir simulations.

Table 3: Percentages of fracture types of the Soledade outcrop. The fractures were grouped into thirty-six groups, according to four direction sets, three-length intervals, and three degrees of karstic dissolution. The total number of fractures is equal to 901.

Length interval	Karstification degree	Set N-S (%)	Set E-W (%)	Set NW-SE (%)	Set NE-SW (%)
1-10 m	Slightly karstified	2.3	7.1	7.7	6.7
	Karstified	6.1	15.3	10.7	16.1
	Highly karstified	1.8	4.3	3.9	5.9
10-100 m	Slightly karstified	0.0	0.6	0.9	0.1
	Karstified	0.4	1.2	0.8	1.3
	Highly karstified	0.3	3.0	1.1	1.4
100-1000 m	Slightly karstified	0.0	0.0	0.0	0.0
	Karstified	0.0	0.0	0.1	0.0
	Highly karstified	0.1	0.1	0.7	0.0

To study the effect of different karstic dissolution scenarios, we simplified the aperture-length relationship (Fig. 12A) by approximating this curve with a piecewise constant by part curve. To do this, the measured aperture values were averaged in the three-length intervals, thus producing the curve shown in black in Fig. 15. Given this curve, three other karstic dissolution scenarios were elaborated (Figs. 15 and 16), according to increasing degrees of dissolution. Note that in each interval length, the log of the apertures increases linearly (the apertures increase in accordance with geometric progressions) between the scenarios to reach the final end-member scenario where all apertures are equal, regardless of length. The final four piecewise constant values, composing the curves relating aperture and length shown in Fig. 15, will be from now on be referred to as the reference (or Stage 1 in black), Stage 2 (in orange), Stage 3 (in dark orange), and Stage 4 (in red) scenarios of karstic dissolution.

Table 4: Average apertures calculated for the Soledade outcrop. The fractures were grouped into twelve groups, according to four direction sets and three length intervals, in order to obtain just one representative value of aperture to each fracture set.

Length interval	**Aperture (mm)**			
	Set N-S	Set E-W	Set NW-SE	Set NE-SW
1-10 m	77.72	95.10	116.71	154.56
10-100 m	231.84	280.60	229.61	232.80
100-1000 m	880.92	1039.22	929.47	No fractures

For each one of the four stages of karstic dissolution, the intrinsic permeability in the *i* (northeast) direction is shown in Fig. 16. First, note that Fig. 16A is a good approximation to Fig. 15B, thus validating the simplified approach of constructing aperture-length curves with piecewise constant values. Second, from Stage 1 to Stage 4 of karstic dissolution, the increase in intrinsic permeability covers approximately five orders of magnitude. As a consequence, fracture networks with the same connectivity might present very different transmissivity values due to the enlargement of fractures caused by dissolution.

2.7 Discussion

2.7.1 Tectonic origin of the fractures in the Soledade and Arapuá outcrops

The main differences between the two outcrops are fracture density and the relative predominance of the orthogonal or conjugate fracture systems. However, the abutting and crosscutting relationships of the fractures in both outcrops indicate that they are coeval.

Concerning possible origin, the fracture directions are consistent with the first post-Campanian tectonic event that affected the Potiguar Basin (Bezerra et al., 2020). In turn, the development of the Apodi fold (Fig. 1B), during the second tectonic event, might be the cause of the higher fracture density in the Arapuá outcrop (Bagni et al., 2020), since during this event, new fractures with the same direction as the older structures were created (Bertotti et al., 2017). In addition, many preexisting veins and stylolites were dissolved and extended (Bertotti et al., 2017). This may have contributed to the intense enlargement of the ENE-WSW trending stylolites observed in the Soledade outcrop (Fig. 4A).

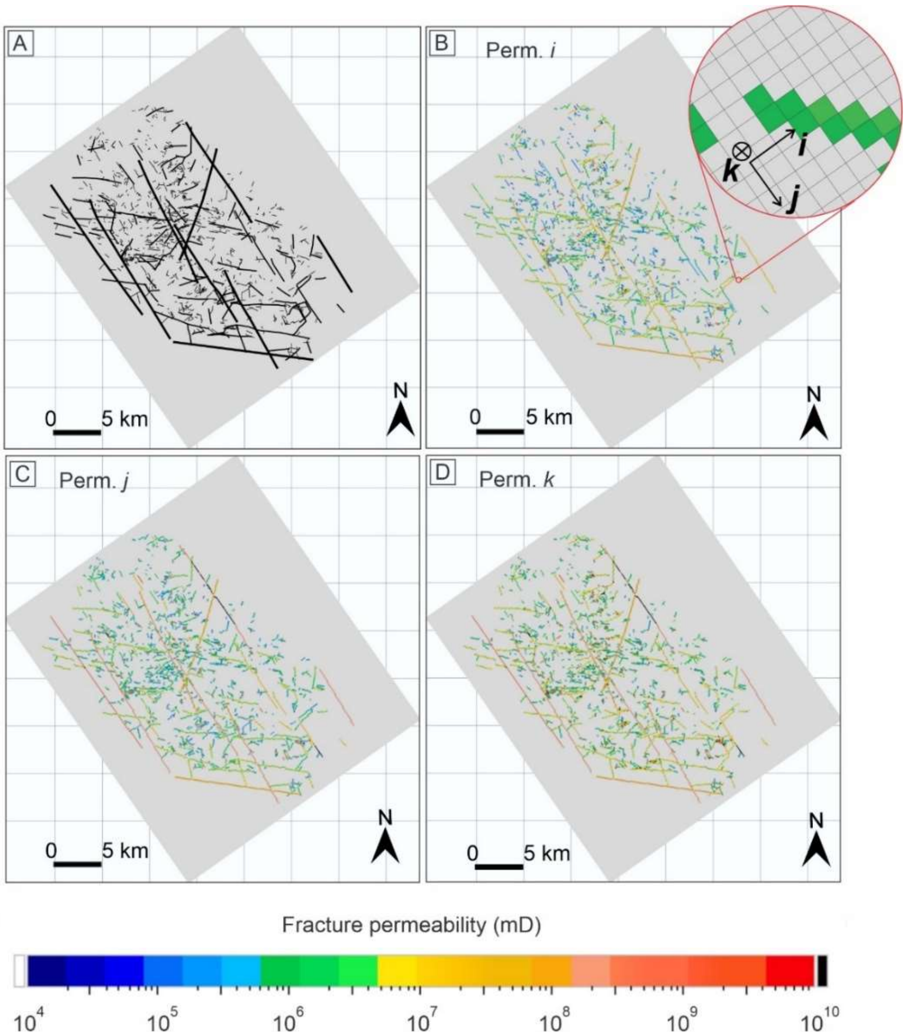

Figure 14: Static model for the Soledade outcrop. Deterministic DFN model (A) and intrinsic permeabilities of the fractures in the main directions i (B), j (C), and k (D) of the intrinsic permeability tensor.

2.7.2 Karstic dissolution effects on length and aperture of fractures

The main parameters that control the fluid flow in a fracture network are the connectivity, aperture, density, and roughness of the fractures (Berkowitz, 2002; Moumni et al., 2016; Huo et al., 2016). Although fracture systems have been widely studied, as well as their implications for fluid flow in reservoirs (e.g., Hardebol et al., 2015; Massaro et al., 2018; Giuffrida al., 2019), incorporating the impact of karstification in these studies is still a debated topic (Mendekenova and Jones, 2014; Tian et al., 2016; Lu et al., 2020).

The analysis for the probability of occurrence of number of fractures as function of length (Fig. 7) shows that, in both outcrops, fracture lengths follow power laws, in accordance with described results in the literature (e.g., Bonnet et al., 2001; Neumann, 2008; Bertrand et al., 2015; Miranda et al., 2018). This behavior results mainly from the fact that fracture growth is controlled by mechanical interactions, which occur during fracture formation, resulting in nonrandom distributions of fracture length (Davy et al., 2013). In addition, it evidences that karstification process does not significantly affected the distribution of fracture lengths in both outcrops.

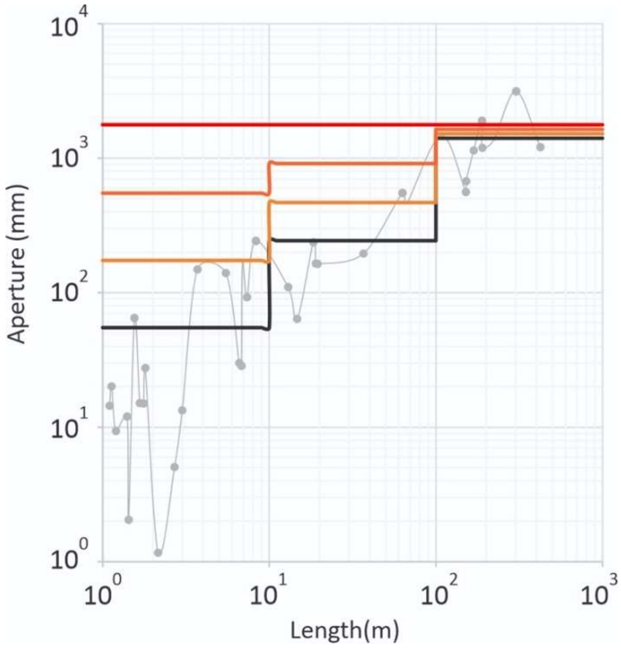

Figure 15: Soledade outcrop. Four scenarios (piecewise constant curves) for the aperture-length relationship incorporating an increase in the degree of karstic dissolution. The four curves represent the reference scenario or Stage 1 (in black), Stage 2 (in orange), Stage 3 (in dark orange), and Stage 4 (in red). The gray curve is the same aperture-length curve

shown in Fig. 12A. Stage 1 is then a piecewise constant curve approximating the actual dataset. The other three piecewise constant curves represent hypothetical karstic dissolution scenarios to exemplify a practical implementation of the conceptual approach given in Fig. 13.

However, this scenario changes drastically in relation to fracture aperture. Many studies based on outcrop data propose that apertures in open mode fractures in carbonate rocks are distributed according to power laws (e.g., Marret et al., 1999; Ortega et al., 2006; Hooker et al., 2012, 2013; Guerriero et al., 2010; Miranda et al., 2018; Massaro et al., 2019). This behavior implies scale invariance, meaning that it is possible to predict the occurrence of a given parameter on unobserved scales (Laubach and Gale 2006; Hooker et al. 2009). However, all the studies mentioned above were based on kinematic apertures only. Because in Soledade outcrop, the probability distribution for apertures still follows a power law, this implies that karstic dissolution degree is still relatively low, so that aperture remains related to fracture length as predicted by mechanical models. On the other hand, in the Arapuá outcrop, probability of occurrence of fracture aperture follows an exponential distribution. We attribute this difference between the two outcrops to the influence of aperture enlargement caused by a higher degree of karstic dissolution in Arapuá. In accordance, the linear relationship (in bi-logarithm graphs) between fracture aperture and length is no longer valid in Arapuá, but it is still valid in Soledade.

The models presented by Clark et al. (1995) and Hooker et al. (2012) for open fractures (open mode fractures) show similar results regarding probability distributions for aperture values. Clark et al. (1995) proposed different models relating aperture and length of fractures to explain the growth of metamorphic veins in the Kodiak complex. In a model where the aperture growths in proportion to the length, simulations of vein thickness results in a power law distribution for the apertures, whereas for a constant growth model, regardless of length, the resulting distribution is exponential.

Hooker et al. (2012) obtained similar results to those of Clark et al. (1995), showing that, in carbonate rocks, random simulations of aperture which are not proportional to fracture length result in exponential distributions for the apertures. The main difference between our results and the results of Clark et al. (1995) and Hooker et al. (2012) is that we worked with actual field data and not with simulations.

We conclude then that fracture apertures are highly influenced by the degree of karstic dissolution of the fracture networks. As consequence, fracture apertures tend to a constant value, regardless of fracture length, when the degree of karstic dissolution is high (Fig. 13). Akara et al. (2020) evaluated the influence of apertures on the intrinsic permeability of a fracture system from comparisons between a sublinear aperture-length relationship and a constant aperture value for all fracture lengths. Flow simulations in these two scenarios were calibrated with data reported from a pumping test. According to Akara et al. (2020), the two approaches reported good agreement with the pumping test results, but the sublinear aperture-length relationship provided a more realistic representation of the permeability of the fracture system, in accordance with our results.

We recommend that the interpreter can try to identify the degree of fracture enlargement based on borehole log images, well test analysis and/or mud loss drilling information, for example. Based on this evaluation, the interpreter can test and analyze different scenarios of aperture-length laws in order to propose better models for predicting the behavior of reservoirs containing karstified fracture networks.

Besides the aperture effects, fracture connectivity in rocks with low-permeability matrix is fundamental to understand fluid flow behavior (Berkowitz, 2002). Depending on the spatial organization of the fractures (reflected in the associated exponent of the scale law), different fracture networks may have different connectivities, which result in different transmissivities (Bour and Davy, 1997; Sanderson and Nixon, 2015). In addition, depending on the karstic dissolution degree, fracture networks with the same connectivity can present different values of transmissivity (Fig. 16), since the latter is fundamentally controlled by the fracture apertures, which are strongly impacted by dissolution.

2.7.3 Limitations of the proposed approach for real reservoir simulations

Some considerations must be done when applying the obtained results for real oil reservoirs. Fracture studies in outcrops are generally restricted to 2D analyses and, for this reason, they might be applied with caution in 3D scenarios, particularly in the presence of dipping fractures (Lei et al., 2017). In fact, in this situation 2D analyses often underestimate permeability and connectivity in relation to 3D approaches (Lang et al., 2014). However, our study is based on subvertical fractures, which are very common in nature. Certainly, this is one of the reasons why so many studies of reservoir analogues are done in outcrops presenting subvertical fractures (Odling et al., 1999; Becker et al., 2018; Biber et al., 2018). In fact, if fractures are subvertical, connectivity is approximately the same for 2D and 3D models.

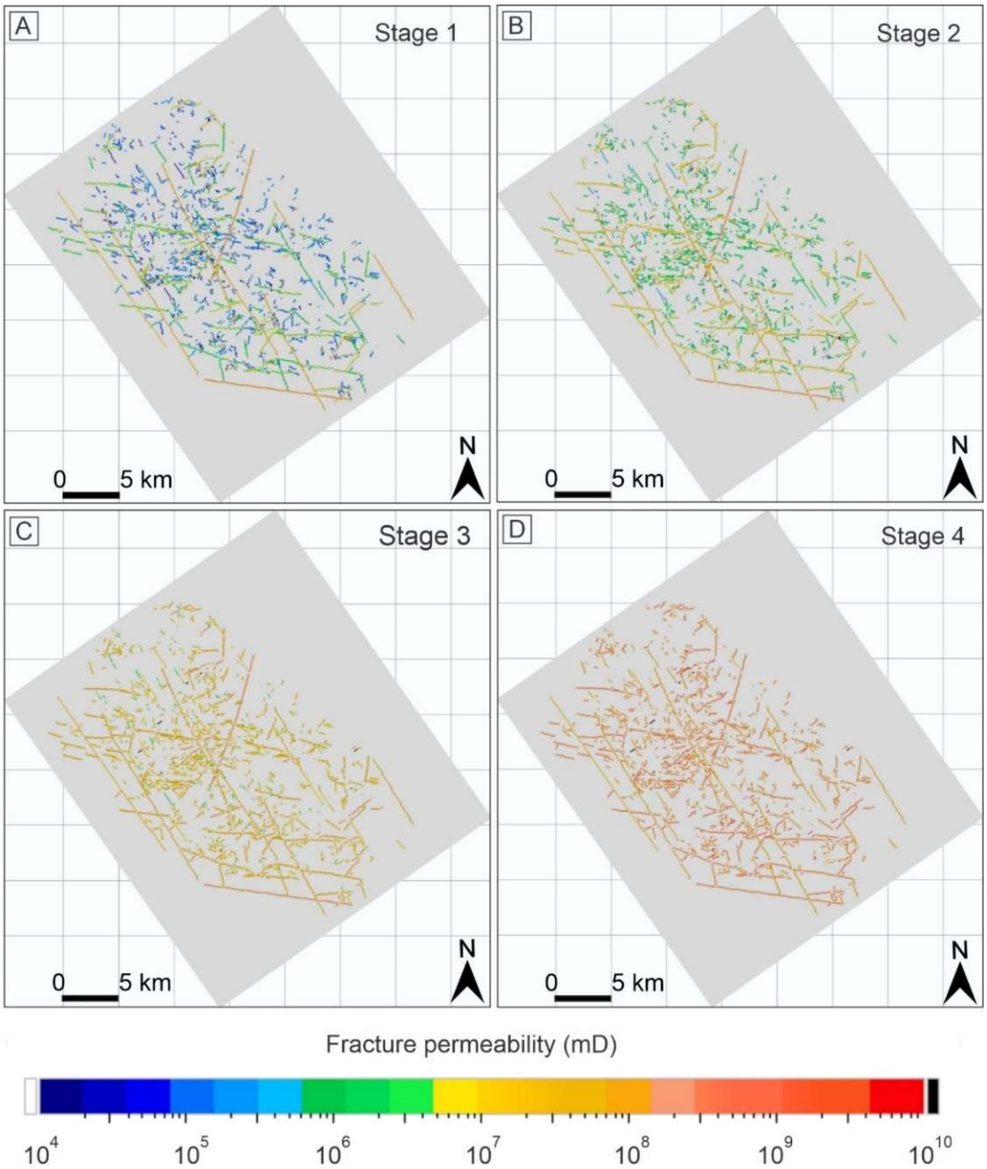

Figure 16: Soledade outcrop. Intrinsic permeability of the fractures in the principal direction i of the intrinsic permeability tensor (Fig. 14B), for the four stages of aperture-length distribution, depending on the degree of karstic dissolution (Fig. 15).

Additional information about fracture infilling, lithology and sedimentary structures is also demanded for adapting the results for real reservoir modelling (Eltom et al., 2016; Gao et al., 2016). Typically, fractures in carbonate reservoirs are infilled with geologic materials resulting from dissolution, transport and precipitation processes. These materials have also great influence in fluid flow (Popov et al., 2009; Gao et al., 2016). However, if the infilling materials are permeable, fracture networks are still the dominant routes for fluid flow in rocks with low-permeability matrix and our results are still valid, at least in a qualitative approach.

Concerning lithology and sedimentary structures, differences in the sedimentary processes and diagenesis can promote significant variations in primary porosity and permeability between layers (Eltom et al., 2016; Abdullah, 2021). However, most carbonate rocks have a very low-permeability matrix due to cementation and compaction during diagenesis (Halley and Schmoker, 1983). In this situation, most of the effective porosity and permeability are of secondary origin, as occurs in the Jandaíra Formation (Bagni et al., 2020; Araújo et al., 2021). As a result, fractures concentrate fluid flow pathways, regardless of lithologic variations, allowing that fracture permeability be four orders of magnitude greater than matrix permeability (Rashid et al., 2021).

Finally, we stress that fracture aperture values measured in outcropping rocks do not represent, in general, good approximations for the aperture values in subsurface conditions. For this reason, the obtained aperture values should be used in reservoir modeling only for rough estimations (Becker et al., 2018). To determine the actual values for fracture aperture in great depths, it is necessary to know the ambient stress field in addition to the burial conditions (Wilson et al., 2011; Becker et al., 2018). As we mentioned above, using information from borehole log images might be a good approach to estimate aperture values. However, the guiding idea that aperture-length relationship is controlled by the degree of karstic dissolution is also valid for carbonate reservoirs, regardless of reservoir depth.

2.8 Conclusion

The present study combined field data and UAV imagery to characterize two outcropping fracture networks in low-porosity carbonate rocks of the Jandaíra Formation (Potiguar Basin) presenting different degrees of karstic dissolution. Our main objective was to estimate the impact of dissolution degree on the geometric properties of the fracture networks.

The probability distributions of fracture length follow power laws in both studied outcrops, regardless of dissolution degree. However, due to different distances from the two outcrops to a regional anticline, the fitted power laws present distinct exponents, that are related to the connectivity of each fracture network. The smaller the exponent of the power law is, the lower the connectivity of the fracture system, which is controlled by the largest fractures. In this case, fluid flow and dissolution are more channeled/concentrated in the longest fractures, as in the case of Soledade outcrop. Conversely, the higher the power law exponent is, the greater the connectivity of the fracture system. In this case, fractures of all size influence fluid flow and karstic dissolution and, as result, fluid flow is more evenly distributed and dissolves the fractures with the same intensity, regardless of their lengths, as in the case of Arapuá outcrop.

The probability distributions of fracture aperture change according to the degree of karstic dissolution. When the degree of dissolution is low, aperture probability data still follows a power law, as in the case of Soledade outcrop. However, when the degree of dissolution is high, the power law behavior is broken, as in the case of Arapuá outcrop. As a result, for non-karstified fracture networks, aperture-length relationship still follows a linear relationship, when plotted on a bi-logarithmic graph, as in the case of Soledade outcrop. However, with an increase in the degree of karstic dissolution, aperture-length curves tend to show a constant value, regardless of fracture length, as in the case of Arapuá outcrop. This reveals the importance of taking into consideration the degree of karstic dissolution when proposing statistical distributions to incorporate aperture values in models simulating carbonate reservoirs. In fact, an increase of approximately five orders of magnitude might occur in the intrinsic permeability of karstified fracture networks as a result of aperture enlargement due to dissolution. As consequence, fracture systems with the same connectivity can present very different values of transmissivity.

Acknowledgments

This research was carried out in association with the ongoing R&D project registered as ANP 20502–1, “Processos e Propriedades em Reservatórios Carbonáticos Fraturados e Carstificados – POROCARSTE 3D” (UFRN/UNB/UFRJ/UFC/Shell Brasil/ANP)

(Porokarst – Processes and Properties in Fractured and Karstifed Carbonate Reservoirs), sponsored by Shell Brasil under the ANP R&D levy as "Compromisso de Investimento com Pesquisa e Desenvolvimento". The Brazilian agency CNPq is thanked for the research fellowships and associated grants provided to WEM and FHRB, besides financial support from the INCT-GP to purchase the computational infrastructure used in this study. Profs. Narendra Srivastava and Charles Bristow helped us to identify the bioclasts and depositional environments, respectively. We thank Tomaz Bezerra for the acquisition and processing of the UAV images. Finally, we thank two anonymous reviewers for their careful and constructive revisions, which greatly improved our manuscript.

REFERENCES

Abdullah, F.H., 2021. Porosity and permeability of karst carbonate rocks along an unconformity outcrop: A case study from the Upper Dammam Formation exposure in Kuwait, Arabian Gulf. Heliyon, 7(7), e07444. https://doi.org/10.1016/j.heliyon.2021.e07444

Agar, S.M., Geiger, S., Matthäi, S.K., 2010. The impact of hierarchical fracture networks on flow partitioning in carbonate reservoirs : examples based on a Jurassic carbonate ramp analog from the High Atlas. SPE Annu. Tech. Conf. Exhib. 2, 1–19. https://doi.org/10.2118/135135-MS

Akara, M.E.M., Reeves, D.M., Parashar, R., 2020. Enhancing fracture-network characterization and discrete-fracture-network simulation with high-resolution surveys using unmanned aerial vehicles. Hydrogeol. J. https://doi.org/10.1007/s10040-020-02178-y

Angelim, L. A. A., Medeiros, V. C., Nesi, J. R., 2006. Programa Geologia do Brasil – PGB, Projeto Mapa Geológico e de Recursos Minerais do Estado do Rio Grande do Norte, Mapa Geológico do Estado do Rio Grande do Norte, Escala 1 : 500 000, Recife: CPRM/FAPERN.

Araújo, R. E., La Bruna, V., Rustichelli, A., Bezerra, F. H., Xavier, M. M., Audra, P., ... Antonino, A. C. 2021. Structural and sedimentary discontinuities control the generation of karst dissolution cavities in a carbonate sequence, Potiguar Basin, Brazil. Mar. Pet. Geol. 123, 104753.

Bagni, F.L., Bezerra, F.H., Balsamo, F., Maia, R.P., Dall'Aglio, M., 2020. Karst dissolution along fracture corridors in an anticline hinge, Jandaíra Formation, Brazil: Implications for reservoir quality. Mar. Pet. Geol. 115, 104249. https://doi.org/10.1016/j.marpetgeo.2020.104249

Becker, I., Koehrer, B., Waldvogel, M., Jelinek, W., Hilgers, C., 2018. Comparing fracture statistics from outcrop and reservoir data using conventional manual and t-LiDAR derived scanlines in Ca2 carbonates from the Southern Permian Basin, Germany. Mar. Pet. Geol. 95, 228–245. https://doi.org/10.1016/j.marpetgeo.2018.04.021

Berkowitz, B., 2002. Characterizing flow and transport in fractured geological media: A review. Adv. Water Resour. 25, 861–884. https://doi.org/10.1016/S0309-1708(02)00042-8

Bertotti, G., de Graaf, S., Bisdom, K., Oskam, B., Vonhof, H.B., Bezerra, F.H.R., Cazarin, C., 2017. Fracturing and fluid-flow during post-rift subsidence in carbonates of the Jandaíra Formation, Potiguar Basin, NE Brazil. Basin Res. 29, 836–853. https://doi.org/10.1111/bre.12246

Bertrand, L., Géraud, Y., Le Garzic, E., Place, J., Diraison, M., Walter, B., Haffen, S., 2015. A multiscale analysis of a fracture pattern in granite: A case study ofthe Tamariu granite, Catalunya, Spain. J. Struct. Geol. 78, 52–66. https://doi.org/10.1016/j.jsg.2015.05.013

Bezerra, F.H., de Castro, D.L., Maia, R.P., Sousa, M.O.L., Moura-Lima, E.N., Rossetti, D.F., Bertotti, G., Souza, Z.S., Nogueira, F.C.C., 2020. Postrift stress field inversion in the Potiguar Basin, Brazil – Implications for petroleum systems and evolution of the equatorial margin of South America. Mar. Pet. Geol. 111, 88–104. https://doi.org/10.1016/j.marpetgeo.2019.08.001

Biber, K., Khan, S.D., Seers, T.D., Sarmiento, S., Lakshmikantha, M.R., 2018. Quantitative characterization of a naturally fractured reservoir analog using a hybrid lidar-gigapixel imaging approach. Geosphere 14, 710–730. https://doi.org/10.1130/GES01449.1

Bisdom, K., Bertotti, G., Bezerra, F. H., 2017. Inter-well scale natural fracture geometry and permeability variations in low-deformation carbonate rocks. J. Struct. Geol. 97, 23-36.

Biver, P., Longis, C., Penna, E., Ovsyannikov, A., 2012. Modeling uncertainties in carbonate karstic reservoirs: Presentation of a tool and its application to a real field case in Russia. In SPE Russian Oil and Gas Exploration and Production Technical Conference and Exhibition. Society of Petroleum Engineers. https://doi.org/10.2118/160721-RU

Bonnet, E., Bour, O., Odling, N.E., Davy, P., Main, I., Cowie, P., Berkowitz, B., 2001. Scaling of fracture systems in geological media. Rev. Geophys. 39, 347–383. https://doi.org/10.1029/1999RG000074

Bour, O., Davy, P., 1997. Connectivity of random fault networks following a power law fault length distribution. Water Resour. 33, 1567–1583. https://doi.org/10.1029/96WR00433

Bourdon, L., Coca, S., Alessio, L., 2004. Karst identification and impact on development plan. SPE Asia Pacific Oil Gas Conf. Exhib. APOGCE 585–593. https://doi.org/10.2523/88520-ms

Burchette, T. P.,2012. Carbonate rocks and petroleum reservoirs: a geological perspective from the industry. Geological Society, London, Special Publications, 370(1), 17–37. doi:10.1144/sp370.14

Cazarin, C.L., Bezerra, F.H.R., Borghi, L., Santos, R. V., Favoreto, J., Brod, J.A., Auler, A.S., Srivastava, N.K., 2018. The conduit-seal system of hypogene karst in Neoproterozoic carbonates in northeastern Brazil. Mar. Pet. Geol. 101, 90–107. https://doi.org/10.1016/j.marpetgeo.2018.11.046

Chang, H. K., Kowsmann, R. O., de Figueiredo, A. M.,1988. New concepts on the development of East Brazilian marginal basins. Episodes Journal of International Geoscience, 11(3), 194-202.

Clark, M., Brantley, S.L., Fisher, D.M., 1995. Power-law vein-thickness distributions and positive feedback in vein growth. Geology 23, 975–978. https://doi.org/10.1130/0091-7613(1995)023<0975:PLVTDA>2.3.CO;2

Córdoba, V.C., 2001, A evolução da plataforma carbonática Jandaíra durante o Neocretáceo na Bacia Potiguar: Análise paleoambiental, diagenética e estratigráfica. PhD Thesis. Universidade Estadual Paulista (UNESP).

Davy, P.,1993. On the frequency-lengthd istributiono f the San Andreas fault system, J. Geophys. Res., 98, 12,141-12,151.

Davy, P., Le Goc, R., Darcel, C., 2013. A model of fracture nucleation, growth and arrest, and consequences for fracture density and scaling. J. Geophys. Res. Solid Earth 118, 1393–1407. https://doi.org/10.1002/jgrb.50120

Davy, P., Le Goc, R., Darcel, C., Bour, O., De Dreuzy, J.R., Munier, R., 2010. A likely universal model of fracture scaling and its consequence for crustal hydromechanics. J. Geophys. Res. Solid Earth 115, 1–13. https://doi.org/10.1029/2009JB007043

de Graaf, S., Reijmer, J.J.G., Bertotti, G. V., Bezerra, F.H.R., Cazarin, C.L., Bisdom, K., Vonhof, H.B., 2017. Fracturing and calcite cementation controlling fluid flow in the shallow-water carbonates of the Jandaíra Formation, Brazil. Mar. Pet. Geol. 80, 382–393. https://doi.org/10.1016/j.marpetgeo.2016.12.014

Eltom, H.A., Kubur, A.K., Abdulraziq, A.M., Babalola, L.O., Makkawi, M.H., Abdullatif, O.M., 2017. Three-dimensional outcrop reservoir analog model: A case study of the Upper Khuff Formation oolitic carbonates, central Saudi Arabia. J. Pet. Sci. Eng. 150, 115–127. https://doi.org/10.1016/j.petrol.2016.11.035

Ennes-Silva, R.A., Bezerra, F.H.R., Nogueira, F.C.C., Balsamo, F., Klimchouk, A., Cazarin, C.L., Auler, A.S., 2016. Superposed folding and associated fracturing influence hy- pogene karst development in Neoproterozoic carbonates, São Francisco Craton, Brazil. Tectonophysics 666, 244–259. https://doi.org/10.1016/j.tecto.2015.11.006.

Fernandes, A.L., Medeiros, W.E., Bezerra, F.H.R., Oliveira, J.G., Cazarin, C.L., 2015. GPR investigation of karst guided by comparison with outcrop and unmanned aerial vehicle imagery. J. Appl. Geophys. 112, 268–278. https://doi.org/10.1016/j.jappgeo.2014.11.017

Fournillon, A., Bellentani, G., Moccia, A., Jumaeucourt, C., Terdich, P., Siliprandi, F., Peruzzo, F., 2017. Characterization of a paleokarstic oil field (Rospo Mare, Italy): sedimentologic and diagenetic outcomes, and their integration in reservoir simula-tion. In: EuroKarst 2016, Neuchatel, no.5.

Gao, B., Huang, Z.Q., Yao, J., Lv, X.R., Wu, Y.S., 2016. Pressure transient analysis of a well penetrating a filled cavity in naturally fractured carbonate reservoirs. J. Pet. Sci. Eng. 145, 392–403. https://doi.org/10.1016/j.petrol.2016.05.037

Ghanbarian, B., Perfect, E., Liu, H.H., 2018. A geometrical aperture-width relationship for rock fractures. Fractals 27, 1–12. https://doi.org/10.1142/S0218348X19400024

Ghosh, S., Galvis-Portilla, H. A., Klockow, C. M., & Slatt, R. M., 2018. An application of outcrop analogues to understanding the origin and abundance of natural fractures in the Woodford Shale. Journal of Petroleum Science and Engineering, 164, 623-639. https://doi.org/10.1016/j.petrol.2017.11.073.

Giuffrida, A., La Bruna, V., Castelluccio, P., Panza, E., Rustichelli, A., Tondi, E., Giorgioni, M., Agosta, F., 2019. Fracture simulation parameters of fractured reservoirs: Analogy with outcropping carbonates of the Inner Apulian Platform, southern Italy. J. Struct. Geol. 123, 18–41.

Giuffrida, A., Agosta, F., Rustichelli, A., Panza, E., La Bruna, V., Eriksson, M., Torrieri, S., Giorgioni, M., 2020. Fracture stratigraphy and DFN modelling of tight carbonates, the case study of the Lower Cretaceous carbonates exposed at the Monte Alpi (Basilicata, Italy). Mar. Petrol. Geol. 112, 104045. https://doi.org/10.1016/j. marpetgeo.2019.104045.

Gong, J., Rossen, W.R., 2017. Modeling flow in naturally fractured reservoirs: effect of fracture aperture distribution on dominant sub-network for flow. Pet. Sci. 14, 138–154. https://doi.org/10.1007/s12182-016-0132-3

Guerriero, V., Iannace, A., Mazzoli, S., Parente, M., Vitale, S., Giorgioni, M., 2010. Quantifying uncertainties in multiscale studies of fractured reservoir analogues: Implemented statistical analysis of scan line data from carbonate rocks. J. Struct. Geol. 32, 1271–1278. https://doi.org/10.1016/j.jsg.2009.04.016

Gutmanis, J., I Oró, L.A., DíEz-Canseco, D., Chebbihi, L., Awdal, A., Cook, A., 2017. Fracture analysis of outcrop analogues to support modelling of the subseismic domain in carbonate reservoirs, south-central Pyrenees. Geol. Soc. Spec. Publ. 459, 139–156. https://doi.org/10.1144/SP459.2

Halley, R.B., and Schmoker, J.W., 1983, High porosity Cenozoic carbonate rocks of south Florida: progressive loss of porosity with depth: AAPG Bulletin, v. 67, p. 191-200.

Hardebol, N. J., Maier, C., Nick, H., Geiger, S., Bertotti, G., Boro, H., 2015. Multiscale fracture network characterization and impact on flow: A case study on the Latemar carbonate platform. Journal of Geophysical Research: Solid Earth, 120(12), 8197-8222. https://doi.org/10.1002/2015JB011879

Healy, D., Rizzo, R.E., Cornwell, D.G., Farrell, N.J.C., Watkins, H., Timms, N.E., Gomez-Rivas, E., Smith, M., 2017. FracPaQ: A MATLAB^{TM} toolbox for the quantification of fracture patterns. J. Struct. Geol. 95, 1–16. https://doi.org/10.1016/j.jsg.2016.12.003

Hooker, J.N., Gale, J.F.W., Gomez, L.A., Laubach, S.E., Marrett, R., Reed, R.M., 2009. Aperture-size scaling variations in a low-strain opening-mode fracture set, Cozzette Sandstone, Colorado. J. Struct. Geol. 31, 707–718. https://doi.org/10.1016/j.jsg.2009.04.001

Hooker, J.N., Gomez, L.A., Laubach, S.E., Gale, J.F.W., Marrett, R., 2012. Effects of diagenesis (cement precipitation) during fracture opening on fracture aperture-size scaling in carbonate rocks. Geol. Soc. Spec. Publ. 370, 187–206. https://doi.org/10.1144/SP370.9

Hooker, J.N., Laubach, S.E., Marrett, R., 2013. Fracture-aperture sized frequency, spatial distribution, and growth processes in strata-bounded and non-strata-bounded fractures, cambrian mesón group, NW argentina. J. Struct. Geol. 54, 54–71. https://doi.org/10.1016/j.jsg.2013.06.011

Huo, D., Pini, R., Benson, S.M., 2016. A calibration-free approach for measuring fracture aperture distributions using X-ray computed tomography. Geosphere 12, 558–571. https://doi.org/10.1130/GES01175.1

James, N.P. and Choquette, P.W.,1988. Paleokarst. Springer, 6Eds., New York 416 p.

Kaufmann, G., 2003. Numerical models for mixing corrosion in natural and artificial karst environments. Water Resour. Res. 39, 1–12. https://doi.org/10.1029/2002WR001707

Lang, P.S., Paluszny, A., Zimmerman, R.W., 2014. Permeability tensor of three-dimensional fractured porous rock and a comparison to trace map predictions. J. Geophys. Res.: Solid Earth 119 (8), 6288–6307.

Laubach, S. E., Gale, J. F. W.,2006. Obtaining fracture information for low-permeability (tight) gas sandstones from sidewall cores. Journal of Petroleum Geology, 29(2), 147-158. https://doi.org/10.1111/j.1747-5457.2006.00147.x

Lei, Q., Latham, J.P., Tsang, C.F., 2017. The use of discrete fracture networks for modelling coupled geomechanical and hydrological behaviour of fractured rocks. Comput. Geotech. 85, 151–176. https://doi.org/10.1016/j.compgeo.2016.12.024

Lomize, G.M., 1961. Water flow in jointed rock (trans. Filtrarsiia v Treshchinovatykh Porod). Gosenergoizdat, Moscow

Louis, CA.,1969. A study of groundwater flow in jointed rock and its influence of the stability of rock masses. Rock mechanics research report 10. Imperial College, London

Lu, X., Wang, Y., Yang, D., Wang, X., 2020. Characterization of paleo-karst reservoir and faulted karst reservoir in Tahe Oilfield, Tarim Basin, China. Adv. Geo-Energy Res. 4, 339–348. https://doi.org/10.46690/ager.2020.03.11

Marrett, R., Ortega, O.J., Kelsey, C.M., 1999. Extent of power-law scaling for natural fractures in rock. Geology 27, 799–802. https://doi.org/10.1130/0091-7613(1999)027<0799:EOPLSF>2.3.CO;2

Massaro, L., Corradetti, A., Tramparulo, F.D., Vitale, S., Prinzi, E.P., Iannace, A., Parente, M., Invernizzi, C., Morsalnejad, D., Mazzoli, S., 2019. Discrete fracture network modelling in triassic–jurassic carbonates of NW lurestan, zagros fold-and-thrust belt, Iran. Geosci. 9, 1–24. https://doi.org/10.3390/geosciences9120496

Massaro, L., Corradetti, A., Vinci, F., Tavani, S., Iannace, A., Parente, M., Mazzoli, S., 2018. Multiscale Fracture Analysis in a Reservoir-Scale Carbonate Platform Exposure (Sorrento Peninsula, Italy): Implications for Fluid Flow. Geofluids 2018. https://doi.org/10.1155/2018/7526425

Matos, R. M. D., 1992. The Northeast Brazilian Rifte System: Tectonics, 11(4), 766–791. https://doi.org/10.1029/91TC03092

Matos, R.M.D, 2000. Tectonic evolution of the equatorial South Atlantic. In: Mohriak, W.U., Talwani, M. (Eds.), Atlantic rifts and continental margins. AGU Geophysical Monograph, 115, 331–354. https://doi.org/10.1029/GM115p0331

Manzocchi, T. (2002). The connectivity of two-dimensional networks of spatially correlated fractures. Water Resources Research, 38(9), 1-1. http://dx.doi.org/10.1029/2000WR000180

Medekenova, A., Jones, G.D., 2014. Characterization and modeling challenges associated with fracture and karst (non-matrix) in the margin area of a carbonate reservoir. Soc. Pet. Eng. - SPE Annu. Casp. Tech. Conf. Exhib. https://doi.org/10.2118/172275-ms

Menezes, D.F., Bezerra, F.H., Balsamo, F., Arcari, A., Maia, R.P., Cazarin, C.L., 2020. Subsidence rings and fracture pattern around dolines in carbonate platforms – Implications for evolution and petrophysical properties of collapse structures. Mar. Pet. Geol. 113, 104113. https://doi.org/10.1016/j.marpetgeo.2019.104113

Miranda, T.S., Santos, R.F., Barbosa, J.A., Gomes, I.F., Alencar, M.L., Correia, O.J., Falcão, T.C., Gale, J.F.W., Neumann, V.H., 2018. Quantifying aperture, spacing and fracture intensity in a carbonate reservoir analogue: Crato Formation, NE Brazil. Mar. Pet. Geol. 97, 556–567. https://doi.org/10.1016/j.marpetgeo.2018.07.019

Moumni, Y., Msaddek, M.H., Chermiti, A., Chenini, I., Mercier, E., Dlala, M., 2016. Quantitative analysis of fractured carbonate reservoir and hydrodynamic implications: Case study of Horchane-Braga basin (central Tunisia). J. African Earth Sci. 124, 311–322. https://doi.org/10.1016/j.jafrearsci.2016.09.016

Nelson, R. A.,2001. Geologic Analysis of Naturally Fractured Reservoirs, 2nd ed., Gulf Prof. Publ. Co., Boston, Mass.

Neuman, S.P., 2008. Multiscale relationships between fracture length, aperture, density and permeability. Geophys. Res. Lett. 35, 1–6. https://doi.org/10.1029/2008GL035622

Odling, N.E. bac., Gillespie, P., Bourgine, B., Castaing, C., Chilés, J.P., Christensen, N.P., Fillion, E., Genter, A., Olsen, C., Thrane, L., Trice, R., Aarseth, E., Walsh, J.J., Watterson, J., 1999. Variations in fracture system geometry and their implications for fluid flow in fractured hydrocarbon reservoirs. Pet. Geosci. 5, 373–384. https://doi.org/10.1144/petgeo.5.4.373

Olson, J.E., 2003. Sublinear scaling of fracture aperture versus length: An exception or the rule? J. Geophys. Res. Solid Earth 108. https://doi.org/10.1029/2001jb000419

Ortega, O.J., Marrett, R.A., Laubach, S.E., 2006. A scale-independent approach to fracture intensity and average spacing measurement. Am. Assoc. Pet. Geol. Bull. 90, 193–208. https://doi.org/10.1306/08250505059

Peacock, D.C.P., Nixon, C.W., Rotevatn, A., Sanderson, D.J., Zuluaga, L.F., 2016. Glossary of fault and other fracture networks. J. Struct. Geol. 92, 12–29. https://doi.org/10.1016/j.jsg.2016.09.008

Pessoa Neto, O., Soares, U.M., Fernandes Da Silva, J.G., Roesner, E.H., Florencio, C.P., Valentin De Souza, C.A., 2007. Bacia Potiguar. Bol. Geociencias da Petrobras 15, 357–369.

Pickering, G., Bull, J.M., Sanderson, D.J., Harrison, P. V., 1994. Fractal Fault Displacements: A Case Study from the Moray Firth, Scotland. Fractals Dyn. Syst. Geosci. 105–119. https://doi.org/10.1007/978-3-662-07304-9_9

Popov, P., Efendiev, Y., Qin, G., 2009. Multiscale modeling and simulations of flows in naturally fractured karst reservoirs. Commun. Comput. Phys. 6, 162– 184.

Price, N.J., 1966. Fault and Joint Development in Brittle and Semi-brittle Rock. Pergamon, Oxford.

Rabelo, J.G., Maia, R.P., Bezerra, F.H.R., Silva, C.C.N., 2020. Karstification and fluid flow in carbonate units controlled by propagation and linkage of mesoscale fractures, Jandaíra Formation, Brazil. Geomorphology 357, 107090. https://doi.org/10.1016/j.geomorph.2020.107090Rashid, F., Hussein, D., Lawrence, J.A., Ahmed, Z., 2021. Fluid flow and permeability analysis of tight gas carbonate reservoir rocks using fractures and dynamic data. J. Nat. Gas Sci. Eng. 90, 103894. https://doi.org/10.1016/j.jngse.2021.103894

Reis, A.F.C., Bezerra, F.H.R., Ferreira, J.M., Do Nascimento, A.F., Lima, C.C., 2013. Stress magnitude and orientation in the Potiguar Basin, Brazil: implications on faulting style and reactivation. J. Geophys. Res.: Solid Earth 118. https://doi.org/10.1002/ 2012JB009953.

Rispoli, R., 1981. Stress fields about strike-slip faults inferred from stylolites and tension gashes. Tectonophysics 75(3-40, T29-T36. https://doi.org/10.1016/0040-1951(81)90274-2

Sanderson, D.J. and Nixon, C.W., 2015. The use of topology in fracture network characterization. J. Struct. Geol. 72, 55–66. https://doi.org/10.1016/j.jsg.2015.01.005

Sanderson, D.J., Nixon, C.W., 2018. Topology, connectivity and percolation in fracture networks. J. Struct. Geol. 115, 167–177. https://doi.org/10.1016/j.jsg.2018.07.011

Santos Filho, M.A.B., Piovesan, E.K., Fauth, G., Srivastava, N.K., 2015. Paleoenvironmental interpretation through the analysis of ostracodes and carbonate microfacies: study of the Jandaíra Formation, upper cretaceous, Potiguar Basin. Brazilian J. Geol. 45, 23–34. https://doi.org/10.1590/23174889201500010002.

Siddiqui, N. A., Mathew, M. J., Ramkumar, M., Sautter, B., Usman, M., Rahman, A. H. A., ... & Sum, C. W., 2020. Sedimentological characterization, petrophysical properties and reservoir quality assessment of the onshore Sandakan Formation, Borneo. Journal of Petroleum Science and Engineering, 186, 106771. https://doi:10.1016/j.petrol.2019.106771

Silva, O.L., Bezerra, F.H.R., Maia, R.P., Cazarin, C.L., 2017. Karst landforms revealed at various scales using LiDAR and UAV in semi-arid Brazil: consideration on karstification processes and methodological constraints. Geomorphology 295, 611–630. https://doi.org/10.1016/j.geomorph.2017.07.025

Snow, D.T., 1965, A parallel-Plate Model of Fractured Permeable Media. Ph.D. Thesis. University of California, Berkeley, and University Microfilms, Inc., Ann Arbor, Michigan.

Souche, L., Astratti, D., Aarre, V., Clerc, N., Clark, A., Al Dayyni, T.N.A., Mahmoud, S.L., 2012. A dual representation of multiscale fracture network modelling: Application to a giant UAE carbonate field. First Break 30, 43–52. https://doi.org/10.3997/136S-2397.2012004

Tian, F., Jin, Q., Lu, X., Lei, Y., Zhang, L., Zheng, S., Zhang, H., Rong, Y., Liu, N., 2016. Multi-layered ordovician paleokarst reservoir detection and spatial delineation: A case study in the Tahe Oilfield, Tarim Basin, Western China. Mar. Pet. Geol. 69, 53–73. https://doi.org/10.1016/j.marpetgeo.2015.10.015

Tibana, P., Terra, G.J.S., 1981. Sequências carbonáticas do cretáceo na Bacia Potiguar. Bol. Tec. Petrobras 24, 174–183.

Torabi, A., Berg, S.S., 2011. Scaling of fault attributes: A review. Mar. Pet. Geol. 28, 1444–1460. https://doi.org/10.1016/j.marpetgeo.2011.04.003

Vermilye, J. M., and Scholz, C. H., 1995. Relation between vein length and aperture: Journal of Structural Geology, 17(3), 423–434, doi:10.1016/0191-8141(94)00058-8. https://doi.org/10.1016/0191-8141(94)00058-8

Volatili, T., Zambrano, M., Cilona, A., Huisman, B.A.H., Rustichelli, A., Giorgioni, M., Vittori, S., Tondi, E., 2019. From fracture analysis to flow simulations in fractured carbonates: The case study of the Roman Valley Quarry (Majella Mountain, Italy). Mar. Pet. Geol. 100, 95–110. https://doi.org/10.1016/j.marpetgeo.2018.10.040

Wang, J., Yu, Q., 2018. Experimental investigations of the process of carbonate fracture dissolution enlargement under reservoir temperature and pressure conditions. Geofluids 2018, 1–19. https://doi.org/10.1155/2018/5971421

Wilson, C.E., Aydin, A., Karimi-Fard, M., Durlofsky, L.J., Sagy, A., Brodsky, E.E., Kreylos, O., Kellogg, L.H., 2011. From outcrop to flow simulation: constructing discrete fracture models from a LIDAR survey. AAPG Bull. 95, 1883–1905. https://doi.org/10.1306/03241108148

Wennberg, O.P., Casini, G., Jonoud, S., Peacock, D.C.P., 2016. The characteristics of open fractures in carbonate reservoirs and their impact on fluid flow: A discussion. Pet. Geosci. 22, 91–104. https://doi.org/10.1144/petgeo2015-003

Witherspoon, P. A., Wang, J. S., Iwai, K., Gale, J. E.,1980. Validity of cubic law for fluid flow in a deformable rock fracture. Water resources research, 16(6), 1016-1024. https://doi.org/10.1029/WR016i006p01016

Xavier Neto, P., Bezerra, F.H.R., Silva, C.C.N., da Cruz, J.B., 2008. O condicionamento estrutural do carste Jandaíra e da espeleogênese associada pela tectônica pós-campaniana da Bacia Potiguar. Congresso Brasileiro De Geologia, 44 Curitiba.

Yao, M., Chang, H., Li, X., Zhang, D., 2019. An integrated approach for history matching of multiscale-fracture reservoirs. SPE J. 24, 1508–1525. https://doi.org/10.2118/195589-PAZeeb, C., Gomez-Rivas, E., Bons, P.D., Blum, P., 2013. Evaluation of sampling methods for fracture network characterization using outcrops. AAPG Bull. 97, 1545–1566. https://doi.org/10.1306/02131312042

3. MANUSCRITO SUBMETIDO

O conteúdo deste capítulo compõe um manuscrito que foi submetido em 10/09/2022 para publicação no periódico *Marine and Petroleum Geology.*

Three-dimensional characterization of karstic dissolution zones, fracture networks, and lithostratigraphic interfaces using GPR cubes, core logs, and petrophysics: implications for thief zones development in carbonate reservoirs

Juliana A.G. Lopes[(a)], Walter E. Medeiros[(a)(b)(c)(e)], Josibel G. Oliveira Jr. [(a)(b)], Flávio L. Santana[(a)(b)], Renata E.B. Araújo[(a)], Vincenzo La Bruna[(a)(d)], Milton M. Xavier[(a)(b)], Francisco H.R. Bezerra[(a)(d)]

(a) Post-Graduation Program on Geodynamics and Geophysics, Federal University of Rio Grande do Norte, Natal, Brazil
(b) Department of Geophysics, Federal University of Rio Grande do Norte, Natal, Brazil
(c) INCT-GP/CNPq/CAPES-National Institute of Science and Technology in Petroleum Geophysics
(d) Department of Geology, Federal University of Rio Grande do Norte, Natal, Brazil
(e) Corresponding author

E-mails: walter.medeiros@ufrn.br
juliana.aglopes@yahoo.com.br
josibel.oliveira@ufrn.br
flavio.geofisica@yahoo.com.br
renataaa.brito@gmail.com
vincenzolabruna@gmail.com
milton.morais@ufrn.br
hilario.bezerra@ufrn.br

Abstract

Fractures and karstic dissolution features have been recognized to significantly affect subsurface fluid flow on a range of scales in carbonate rocks. However, due to the information gap between seismic and borehole scales, characterizing these features is a real challenge. We present a three-dimensional multidisciplinary approach to identify the main factors controlling the formation of connected rock volumes composed by permeable karstic dissolution zones. We investigate two outcrops in the Jandaíra Formation, which is an intensely fractured and karstified carbonate platform in the Potiguar Basin, Brazil. Two GPR cubes are jointly interpreted with cored boreholes, borehole images, petrophysical profiles, and thin sections. We verified that attenuated zones of GPR signal are related to secondary carbonate changes caused by fracturing and/or diagenetic alterations, leading to the development of relatively high secondary permeability. At least three types of attenuation/karstic zones might occur: fractured or broken zones affected by fracture enlargement due to dissolution, zones submitted to intense diagenetic alterations, and void spaces as a final end-member of these two processes. Fractures are preferential routes to fluid flow, thus contributing to increase dissolution processes, particularly in layers having relatively high values of primary matrix porosity and permeability. On the other hand, relevant diagenetic alterations might occur in layers that contain high concentration of stylolites. As a result of interconnecting dissolved stylolites, zones of relatively high secondary permeability can be created regardless of the primary values of matrix porosity and permeability. Geobodies of connected volumes of karstic zones often present tabular shapes and are delimited by subvertical fractures and subhorizontal lithostratigraphic interfaces. In the reservoir scale, these tabular geobodies might compose highly connected permeable volumes of altered carbonate rocks that constitute thief zones or super-K layers.

Keywords: Karstified reservoirs; reservoir analogues; karstic dissolution; thief zones; super-K layers; 3D GPR.

3.1 Introduction

Karstic dissolution in carbonate reservoirs results in a complex framework of multiscale heterogeneities. The term karstic dissolution zone is used here to refer to all zones impacted by karstic dissolution processes, such as altered rocks, air- or sediment-filled voids, enlarged fractures, and dissolved stylolites or veins. The associated secondary porosity can significantly increase porosity and permeability of carbonate reservoirs (Jones, 2015; Bagni et al., 2022; Lopes et al., 2022). In particular, layers presenting abnormally high permeability due to karstic dissolution, known as thief zones, can trigger a series of undesirable events, such as early water breakthrough, sharp formation pressure drops, and production water dumping zones (Medeiros et al., 2004; Yixiang et al., 2017; Tian et al., 2019a). Thus, characterizing karstic dissolution zones is fundamental for understanding the behavior of carbonate reservoirs.

However, characterizing karstic dissolution features is a real challenge due to the large disparity in scale of these features, which range from millimeter vugs to kilometer caves, and present irregular shapes and discontinuous distributions (Yan et al., 2022). In addition, high permeable zones are often related to faults and karstified fractures and, therefore, end up being underestimated, especially when they occur in the subseismic scale (La Bruna et al., 2021; Cross et al., 2021). Generally, it is difficult to image karstic features with seismic data due to limits in resolution (Medekenova and Jones., 2014; Tian et al., 2019b; La Bruna et al., 2021). However, larger scale features such as caves, sinkholes and channels can be detected in seismic, especially through seismic attributes (Lu et al., 2020; Cross et al., 2021). Furthermore, because few exploratory wells are commonly available, there is few information about dimensions and geometrical connectivity of karstic networks in the reservoir three-dimensional space (Medekenova and Jones, 2014; Jones, 2015; Li et al., 2016a; Yan et al., 2022). Thus, the study of outcrop analogues can contribute to a better understanding of karstic dissolution zones and, consequently, to reduce uncertainties in characterizing subsurface carbonate reservoirs (Howell et al., 2014; Gutmanis et al., 2017; Becker et al., 2018; Giuffrida et al., 2019). Furthermore, combining geological and geophysical data allows establishing relationships between micro and macro scales features, contributing to a better understanding of heterogeneous reservoirs (Tian et al., 2019b; 2019c).

Ground Penetrating Radar (GPR) is a shallow subsurface non-invasive geophysical method, that can be used to characterize sedimentary facies, fractures, and other features of reservoir analogues (McMechan et al., 2002; Jahnert et al., 2012; Grasmueck et al., 2013). Due to its high resolution and sensibility to rock heterogeneities, GPR has been widely used to image karst (Anchuela et al., 2009; Reis et al., 2014; Mount et al., 2014; Zajc et al., 2014; Fernandes Jr et al., 2015; Oliveira Jr. et al., 2020). In particular, karstic zones are associated with attenuated zones of GPR signal or low amplitude zones (Fernandes et al., 2015; Oliveira Jr. et al., 2020), which can be modeled as zones of low values of quality factor Q (Santos et al., 2022). However, despite being a widespread methodology, there are few GPR studies aiming to characterize three-dimensional (3D) karstic features (e.g., Guidry et al., 2007; Grasmueck et al., 2013; Conti et al., 2019) and, even less, 3D GPR studies of carbonate rocks supported by core logs and petrophysics (e.g., McMechan et al., 2002; Harbi and McMechan, 2011).

Composing 3D geological models of fractured and karstified reservoirs is essential to describe more effectively the relationships between karstic zones, stratigraphic framework, and fracture networks. Generally, 3D representations of hydrocarbon reservoirs are done based on the extrapolation of two-dimensional (2D) models (Zhang et al., 2020; Zhang et al., 2022) and/or based on statistical distributions laws (Méndez et al., 2020; Giuffrida et al., 2019). Nonetheless, these models do not always represent the geometric complexity of fracture networks and associated karst (Huang et al., 2020). That is the key reason to obtain more realistic 3D models of karstic networks. In particular, the resulting information can be used to compose deterministic and stochastic models to train 3D reservoir modeling algorithms (Ghobadi, 2016; Wu et al., 2020).

Our objective is to present a conceptual model for understanding the development of 3D karstified zones in carbonate rocks. The study area is a large outcrop of the Jandaíra Formation, which is an intensely karstified carbonate platform in the Potiguar Basin, Brazil. Specifically, based on the joint interpretation of two GPR cubes, core logs, borehole images, petrophysical profiles and thin sections, we characterize the 3D distribution of karstified zones associated to GPR attenuation zones. We show that connected volumes of karstic zones, as mapped by GPR attenuation zones, compose geobodies that often present tabular shape and are delimited by subvertical fractures and subhorizontal lithostratigraphic interfaces. In the reservoir scale, these tabular geobodies might compose highly connected permeable volumes of altered carbonate rocks, which constitute thief zones or super-K layers.

3.2 Geological Setting

The Potiguar Basin is an aborted NE-trending rift, located on the Equatorial margin of Brazil (Fig. 1A), that was formed during the breakup between South American and African plates in the Jurassic–Cretaceous (Matos, 1992; De Castro et al., 2012).

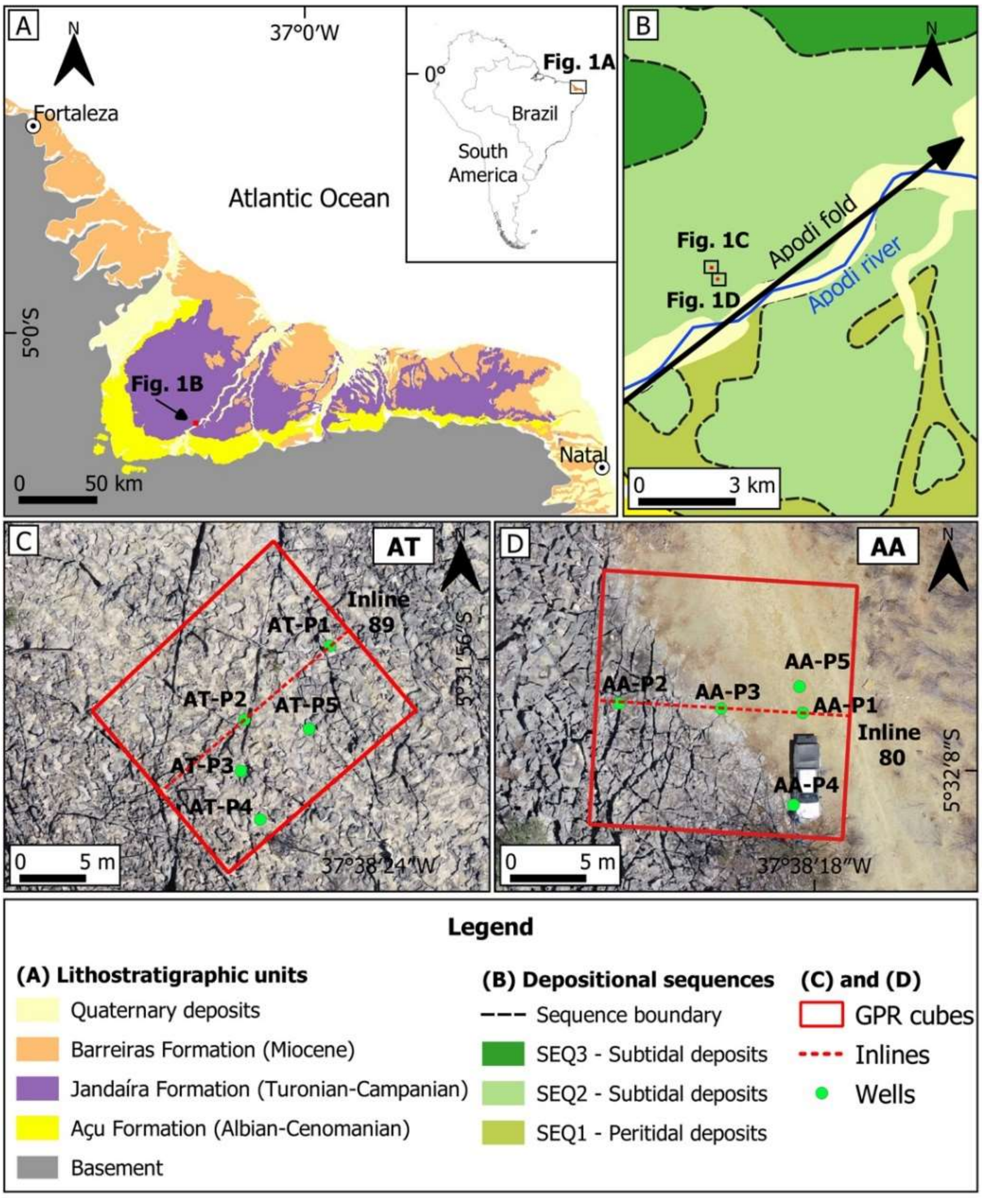

Figure 1: Study area. (A) Simplified geological map of Potiguar Basin, with location of the large Arapuá outcrop. (B) Local geological context of the Arapuá outcrop in relation to the Apodi Fold (modified from Bagni et al., 2020), locating the two small studied areas AT (C) and AA (D). (C and D) Unmanned aerial vehicle images of the two small areas

AT and AA in the Arapuá outcrop, respectively, showing the outlines of the surveyed GPR cubes and positions of the vertical boreholes.

The Potiguar Rift evolved from a NW-SE-oriented extensional regime, in the Early Berriasian, to an E-W-oriented extension during the final stage of rifting in the Barremian (Matos, 1992). This change in the rifting axis direction was responsible for the formation of the onshore and offshore parts of the basin. During the post-rift phase, the tectonic regime was controlled by thermal subsidence and continental drift, allowing the deposition of post-rift sedimentary sequences, including the Jandaíra Formation (Pessoa Neto et al., 2007), focus of this study.

The Jandaíra Formation is an Eoturonian-Eocampanian carbonate platform implanted on a paleomorphology ramp during a transgressive cycle (Córdoba; 2001). The sedimentary package of this unit has a maximum thickness of 600 m, dips gently to NNE, and include lithofacies ranging from mudstones, bioclastic, intraclastic packstones and grainstones to boundstones, with rare intercalations of sandstones, shales, marl, and evaporites (Córdoba, 2001; Pessoa Neto et al., 2007). These lithofacies were deposited in estuarine and mixed beach systems, in the eastern part of the ramp, and tidal plains, besides shallow lagoons and carbonate sand-shoal systems, in the western portion (Córdoba, 2001). The study area (Figs. 1A-B) is in the western part of the basin, where subtidal carbonate deposits crop out (Bagni et al., 2022). The carbonate rocks present porosity around 10% without significant permeability, generally < 1 mD (Bagni et al., 2022). Nevertheless, most of the present porosity and permeability is secondary and is associated with karstified features occurring along bedding planes and fractures (Silva et al., 2017; Bagni et al., 2022).

3.2.1 Evolution of the Jandaíra epigenic karst

The carbonate rocks of the Jandaíra Formation have a history of burial and exhumation episodes, that occurred during the post-rift phase of the Potiguar Basin and led to its present karst landforms. Subvertical fractures and stylolites, in addition to subhorizontal stylolites, which developed during the post-rift phase, are the main conduits for meteoric water percolation that form the epigenic karst in the region (Bertotti et al., 2017; Bagni et al 2020; Araújo 2021; Bagni et al., 2022).

In the post-rift phase, two strike slip regimes affected the sedimentary units of the Jandaíra Formation. During the first tectonic regime, characterized by a Campanian to Miocene N-S-oriented compression and an E-W-oriented extension, the carbonate rocks were completely cemented, and the fluid circulation was restricted to the interconnected fracture networks (de Graaf et al., 2017; Bezerra et al., 2020). According to de Graaf et al. (2017), at the end of this event, percolation of ascending fluids from the underlying siliciclastic Açu Formation led to calcite precipitation as veins, at depths between 400 m and 900 m, decreasing rock permeability. In addition, during a burial episode when carbonates reached depths around 800 to 900 m, subhorizontal stylolites were generated liberating calcite due to pressure solution, which sealed subvertical open fractures, thus also contributing to the reduction of porosity and permeability (Bertotti et al., 2017).

The second and most recent event of deformation, from Miocene to the present, is characterized by a NW-SE-oriented compression and a NE-SW-oriented extension in the central and western parts of the basin, which generated folds and fractures (Bezerra et al., 2020; Bagni et al., 2020). This event was less intense than the first one. As a result, the new structures were not sufficient to reestablish the fluid flow from the Açu Formation (de Graaf et al., 2017). However, the subaerial exposure of the platform in this period, with erosion and karstification due to superposed meteoric-dissolution processes, contributed to the dissolution and enlargement of pre-existing veins, stylolites and fractures, and dissolution of stratigraphic layers (Bertotti et al., 2017; Silva et al., 2017; Bagni et al., 2020; Araujo et al. 2021; Bagni et al., 2022). In the study area, the NW-SE-oriented compression resulted in a large-scale anticline, the Apodi Fold (Fig. 1B), which has a NE-SW-striking fracture corridor on its hinge, that coincides with the Apodi River valley in this region (Bagni et al., 2020). Fracturing and karstic dissolution increase towards the fold axis (Bagni et al., 2020; Lopes et al., 2022).

3.3 Materials and methods

3.3.1 GPR data acquisition

Two 200 MHz pseudo-3D GPR cubes, named as 3D-AT and 3D-AA, were acquired in two small areas of the Arapuá outcrop, named as AT and AA (Figs. 1B-D), respectively. The Arapuá outcrop is close to the Apodi Fold (Bagni et al., 2020), as shown in Fig. 1B.

Both GPR datasets have 169 parallel lines, regularly spaced at 0.1 m (Fig. 2), thus covering approximately 17 m (Figs. 1C-D). The lines are approximately 19 m and 17 m in 3D-AT and 3D-AA (Figs. 1C-D), respectively. The GPR antenna was mounted on wooden rails (Fig. 2), allowing a small and fixed distance between lines (just 0.1 m). As a result, the superposition of the associated Fresnel zones (Yilmaz, 2001) is guaranteed, justifying treating the datasets as pseudo-3D GPR cubes (Grasmueck et al., 2013; Santos et al., 2022). It is then possible to visualize the cube through the simultaneous analyses of parallel (inlines), perpendicular (crosslines), and z-slices (horizontal) images. The inlines correspond to the lines acquired in the field, while the crosslines and z-slices result from interpolation. The inlines were acquired along directions N49 (3D-AT) and N93 (3D-AA) (Figs. 1C-D), to be approximately perpendicular to the main fracture directions, as seen locally. The operational logistics of placing, leveling and stabilizing the wooden pallets on the rough karst terrain is very time consuming (approximately 90% of the survey time), but the quality of the obtained datasets compensates for the effort required.

The raw data were collected with the 200 MHz GSSI antenna, within a time window of 250 ns and a sampling time interval of 0.244 ns. Along inlines, traces were collected every 5 cm and distances were measured with an odometer. To allow the absolute positioning of the cubes, the vertices were located with DGPS.

Figure 2: Photograph taken during the GPR survey in the AT area highlighting the use of wooden pallets. A 200 MHz GSSI antenna is mounted on wooden rails, which are fixed

to the pallet and spaced regularly at 0.10 m. The rails were fixed with small wooden spikes, so that metallic objects are not used.

3.3.2 GPR data processing

The raw data were processed according to the flow described by Oliveira Jr. et al. (2020), using the software REFLEXW (Sandmeier, 2012) and the Seismic Unix subroutines (Colorado School of Mines). The processing flow of Oliveira Jr. et al. (2020) is specially adjusted to improve the quality of GPR images in karstified carbonate rocks. The processing steps include: zero-offset correction, low-frequency noise removal (DEWOW), gain to compensate for spherical divergence losses (SEC), spectral balancing to compensate for absorption and dispersion (Xavier Neto and Medeiros, 2006), Kirchhoff migration, bandpass filtering, and an optional amplitude enhancement technique (Bulhões 1999; Bulhões and Amorim 2005; Vernengo and Trinchero, 2015). The enhancement technique is applied for interpretation purposes, because it allows a better visualization of low amplitude zones (Oliveira Jr. et al., 2020). Migration was done using a mean velocity equal to 0.09 m/ns, estimated by fitting existent hyperbolas due to diffraction in non-migrated sections. Time-depth conversion was done using this velocity value. Topographic correction was not necessary because altitude variation is small on the leveled wooden pallets (Fig. 2).

3.3.3 Boreholes

3.3.3.1 Borehole location

Zones associated with karstic dissolution in general are interpreted as causes of GPR signal attenuation (e.g. Fernandes et al., 2015). However, the precise origins of GPR attenuation zones were not known. Thus, a preliminary interpretation was then performed in the two GPR cubes to choose borehole locations (see an example in Figs. 3A-B), to sample both attenuated and non-attenuated GPR zones, so that the different causes of attenuation could be identified. Five boreholes were drilled in each outcrop (Figs. 1C-D), each one being 10 m deep.

3.3.3.2 Borehole drilling

The vertical boreholes were drilled by a rotary drilling rig and used for rock coring. The core recovery factor was around 91% and 82% for the AT and AA outcrops, respectively, thus revealing that AA outcrop is more affected by fracturing and/or karstic dissolution. An identification of the approximate depth and thickness of voids and fragmented levels was made while drilling.

3.3.3.3 Borehole images

We filmed the borehole walls to allow a direct comparison with cores and GPR images. We use a set of PVC tube pieces that can be threaded together, allowing to reach any depth in the open borehole. Then, we fixed a 21-megapixel cell phone camera at one end of the tube, which was moved into the well to film. A graduated tape was affixed to the tube to identify the depth and direction in which the film was being shot. The threshold depth for each film was determined by the presence of rainwater at the bottom of the well. In the case of boreholes AA-P1 and AA-P5 (Fig. 1D), it was not possible to obtain images because they got obstructed.

3.3.4 Core logs

3.3.4.1 Core description

Core description along depth included lithology, color, texture, type of contact (horizontal discontinuities, lithological variations, dissolved stylolites, voids and/or broken rocks), relative porosity, stylolite characterization (amount per sample, degree of alteration and filling), besides any other relevant information, such as the presence of geodes, veins, and pressure solution seams. After the description of the macroscopic core, sampling points were selected for petrographic analysis and petrophysical measurements of the main identified lithostratigraphic layers.

3.3.4.2 Petrographic analysis

Petrographic analysis aimed to classify the different lithofacies macroscopically identified in the cores. For that, five thin sections were selected that correspond to the main identified lithofacies. The petrographic analyses were performed on an Olympus

BX41 polarized light microscope equipped with a digital camera. The microfacies were classified according to their texture, based on the classification of Dunham (1962) and Embry and Klovan (1971). In addition, the porosity was described based on the principles of Lucia (2007).

3.3.4.3 Petrophysical measurements

Petrophysical measurements include gamma ray, porosity, and permeability. The gamma-ray measurements were obtained directly on the cores using a portable gamma-ray spectrometer (RS-230 BGO Super-SPEC), that allowed to obtain measurements of total radiation (GR) approximately every 20 cm. However, due to the presence of voids and fragments in the cores, keeping measurements at a constant distance of 20 cm was not always possible.

Porosity and permeability measurements were carried out on 2.5 cm diameter plugs, made from the cores, at the same locations where gamma ray measurements were done. A total of 376 plugs were analyzed, 204 for AT outcrop and 172 for AA outcrop. Porosity at atmospheric pressure and permeability measurements corrected by the Klinkenberg factor (Klinkenberg, 1941; Li et al., 2016b) were obtained using the Coreval equipment (gas permeameter in unstable state and porosimeter in overload pressure).

3.4 Results

3.4.1 Identification of the main lithostratigraphic layers

From core description and thin section analyses three main lithostratigraphic layers (AT-I, AT-II, and AT-III) were identified in AT outcrop, and two layers (AA-I and AA-II) in AA outcrop. The main characteristics of the lithostratigraphic layers are described in Fig. 4.

In AT outcrop, the shallowest AT-I package corresponds to grain-supported carbonates composed by packstones/grainstones containing highly micritized grains. The intermediate AT-II package consists of matrix-supported carbonates composed by dolowackstones, which include dolomite crystals, and, in a smaller amount, bioclasts. This package presents a high concentration of bed-parallel stylolites and it is possible to observe that dolomite crystals are concentrated along stylolites and fractures. Finally, the deepest AT-III package consists of grain-supported carbonates, which correspond to bioturbated grainstones/packstones composed mainly of dolomite crystals and, in a smaller amount, intraclasts and bioclasts, mainly foraminifera. Most of the bioturbation appears to be recrystallized, and sometimes filled with a black opaque material, probably organic matter.

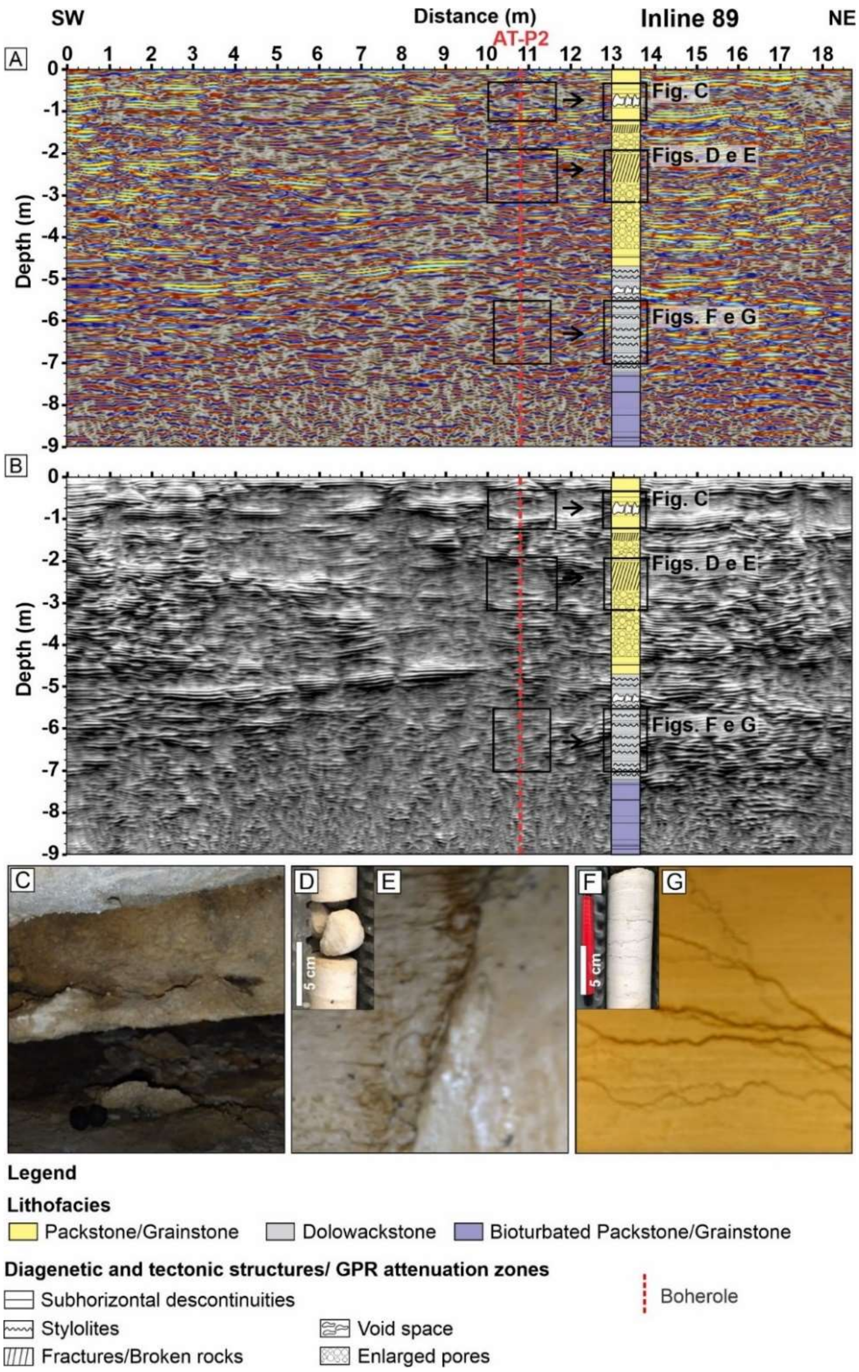

Figure 3: AT outcrop. Example of borehole location (A and B) and photograps illustrating some of the causes of the attenuated zones of GPR signal (C-G). (A and B) GPR Inline

89 of 3D-AT and AT-P2 core log description (see locations in Fig. 1C); the GPR images were processed not including (A) and including (B) the amplitude enhancement technique, that allows a better visualization of attenuated zones of GPR signal (black rectangles). The dashed vertical red line in (A) and (B) shows the exact location of the borehole; note that the core log is shifted horizontally to allow joint viewing. Photographs of the borehole walls (C, E, and G) and core samples (D and F) showing: a void space (C), fragmented rocks (D) due to a partially dissolved subvertical fracture (E), and partially dissolved subhorizontal stylolites (F and G). Pair of photographs D and E were taken approximately in the same depth, the same for the pair F and G.

In AA outcrop, the shallowest AA-I package consists of grain-supported rocks, which correspond to packstones/grainstones composed of highly micritized grains. The deepest AA-II package consists of matrix-supported carbonates, which correspond to wackstones with crystals, mainly calcite, of various sizes, in addition to bioclasts dispersed in a very homogeneous matrix. This package also has a high concentration of stylolites, either slightly or partially dissolved.

Although the AT and AA outcrops present similar characteristics for the lithostratigraphic layers, we decided to not propose a lateral correlation between them because this correlation would require further studies, on a regional scale, on both stratigraphy and structural framework that is beyond the scope of this study.

3.4.2 Correlation of the main lithostratigraphic layers with petrophysical data and GPR images

Porosity and permeability measurements can only be made on preserved cores. As a result, the obtained profiles present gaps where void spaces and fragmented parts of the cores occur. In addition, even in preserved cores, anomalous high values of porosity and permeability can be measured because of relatively intense karstic dissolution, as exemplified in Fig. 5. To obtain statistical robustness to these outliers, we use the median instead of the mean to obtain representative values of porosity and permeability (Tables 1 and 2). The resulting estimates present good correlation with the main lithostratigraphic layers, as can be seen either in cross-plot graphs (Fig. 6) and depth profiles (Figs. 7 and 8).

The AT-I and AA-I packages, composed of packstones/grainstones, present the highest porosity and permeability values in the two outcrops (Figs. 6-8). On the other hand, the AT-II and AA-II packages, which are composed of the finest and recrystallized lithofacies, present the lowest values of porosity and permeability (Figs. 6-8). In general, the contact between AT-I and AT-II, and also between AA-I and AA-II packages, is well-marked by a significant reduction of porosity and permeability (Figs. 7 and 8). Note that in the porosity and permeability profiles (Figs. 7 and 8), it is possible to observe porosity and permeability peaks that stand out within the patterns observed for each sedimentary package. These peaks are examples of the above referred outliers and are related to the presence of dissolved stylolites and pores in the sampled plugs (Fig. 5). Finally, the AT-III package, which is composed of bioturbated packstones/grainstones, presents intermediate values of porosity and permeability (Fig. 6). The contact between AT-II and AT-III packages is also well marked by a sudden change in the pattern of porosity and permeability profiles (Fig. 7A-E).

The gamma-ray profiles (total radiation) present very similar values between all packages, either in AT and AA outcrops (Figs. 7 and 8, and Tables 1 and 2). This behavior is due to the fact that all rocks contain practically the same small amount of radioactive elements, due to their common organic origin. The small oscillations observed in the profiles of total radiation are possibly related to the presence of allochthonous matter.

The interfaces separating the main lithostratigraphic layers are well marked with reflection events in the GPR traces, although some of these events are not too strong, as can be evaluated in Figs. 7 and 8. Nonetheless, lateral continuity is quite good, so that lateral extrapolation of the interfaces inside the GPR cubes could be done, as shown in Figs. 9 and 10. In detail, the M1 surface, which separates the AT-I and AT-II packages, is characterized by a continuous, high-amplitude reflector (Fig. 9A). In turn, the M2 surface, separating AT-II and AT-III layers, can be identified because the AT-III package presents radarfacies with a chaotic pattern (Fig. 9A). In AA outcrop, the M1 surface, which separates the AA-I and AA-II packages, is characterized by a continuous reflector, with high amplitude (Fig. 10A).

Sedimentary package	Core	Thin sections	Lithofacies	Grain size (mm)	Main components (aloquimic grains)	Main cement	Sedimentarary/ Diagenetic structures	Tectonic structures	Main pore type
AT-I (0 ~ 4.5 m)			Packstone/ grainstone	< 6	Foraminifers, gastropods, equinoderms, Intraclasts, pellets	Calcite	Microfractures	Fractures/ veins	Moldic intergrain
AT-II (4.5 ~ 7 m)		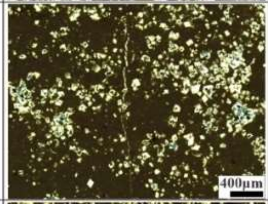	Dolowackstone	< 0.5	Ostracods gastropods	Dolomite	Stylolites filled by calcite	Fractures/ veins	Moldic, intracrystal intercrystal
AT-III (7 ~ 9 m)		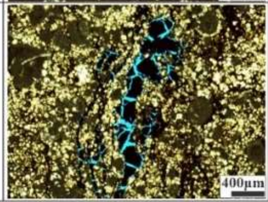	Bioturbated Packstone/ grainstone	< 0.2	Foraminifers intraclasts	Dolomite	Recrystalized bioturbation and stylolites	Fractures/ veins	Moldic intergrain
AA-I (0 ~ 4 m)	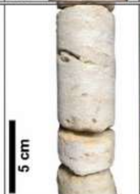	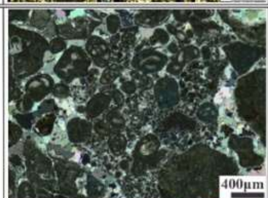	Packstone/ grainstone	< 5.6	Foraminifers, gastropods, equinoderms, Intraclasts	Calcite	Stylolites filled by calcite	Fractures/ veins	Moldic
AA-II (4 ~ 9 m)	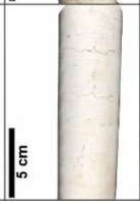	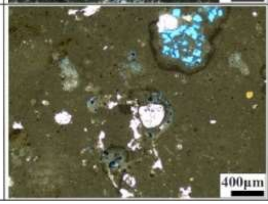	Wackstone	< 0.5	Ostracods gastropods	Calcite and dolomite	Stylolites filled by calcite	Fractures/ veins	Moldic, intracrystal

Figure 4: Characteristics of the main lithostratigraphic layers identified in the outcrops AT and AA from core and thin section analyses.

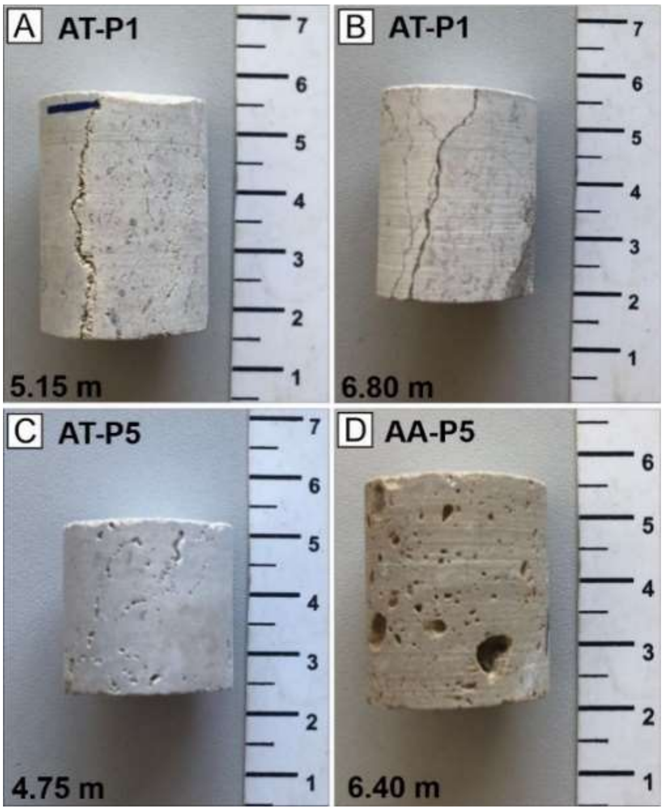

Figure 5: Four examples of core plugs where relatively high porosity and permeability values were measured due to karstic features. (A) shows highly connected open dissolved stylolites. (B) shows connected dissolved stylolites that were partially filled. Finally (C and D) show enlarged pores; in photograph (C), connection of large pores can be seen even in exposed surfaces. Each figure identifies the borehole, plug depth, and scale in cm. Borehole locations are shown in Figs. 1C and 1D.

An integrated interpretation was also performed to define secondary interfaces within the main lithostratigraphic layers. In this process, it was also important to consider the presence of interfaces that delimit either geobodies associated with the GPR signal attenuation zones or relatively more fractured layers. These two aspects will be presented in the next sections. Five secondary stratigraphic surfaces were finally identified in the AT outcrop (S1 to S5 in Figs. 9A and B), and four in the AA outcrop (S1 to S4 Figs. 10A-B).

Table 1: AT outcrop. Statistical summary of the estimates of gamma ray, porosity at atmospheric pressure, and permeability corrected by the Klinkenberg factor, in each main

lithostratigraphic layer. Min, Max, and Mdn stand for the minimum, maximum, and median values, respectively. The total number of plugs for AT outcrop is equal to 204.

Lithofacies	Well	Gamma Ray ($nGyh^{-1}$)			Porosity (%)			Permeability (mD)		
		Min	Max	Mdn	Min	Max	Mdn	Min	Max	Mdn
Grainstones (AT-I)	AT-01	57.6	65.5	59.8	10.22	19.10	16.39	0.008	0.657	0.279
	AT-02	55.4	63.5	59.6	7.37	20.87	18.24	0.003	1.067	0.390
	AT-03	59.3	68.4	62.9	13.91	23.52	18.77	0.048	2.590	0.425
	AT-04	60.5	71.4	66.1	10.58	22.84	17.55	0.065	6.051	0.478
	AT-05	58.2	69.8	65.3	5.86	23.28	16.94	0.005	1.699	0.313
Recrystallized grainstone (AT-II)	AT-01	57.1	62.7	59.1	3.58	9.80	7.18	0.002	1.285	0.003
	AT-02	58.6	65.8	62.5	4.59	9.92	6.08	0.002	0.005	0.003
	AT-03	60.7	64.8	63.0	4.17	13.98	6.89	0.002	0.171	0.004
	AT-04	58.3	68.9	63.0	2.10	7.15	3.46	0.001	0.019	0.003
	AT-05	59.4	68.9	62.9	4.67	18.88	6.62	0.002	0.861	0.004
Brecciated and bioturbated grainstone (AT-III)	AT-01	57.1	62.7	59.1	4.80	14.07	7.19	0.002	1.034	0.008
	AT-02	54.7	69.5	62.8	7.69	16.71	9.48	0.003	0.249	0.012
	AT-03	58.0	65.0	61.6	8.12	18.98	12.64	0.004	1.168	0.093
	AT-04	60.9	70.5	64.9	3.69	20.84	11.68	0.002	2.477	0.043
	AT-05	61.6	71.0	66.2	7.51	13.40	9.10	0.003	0.319	0.014

Table 2: AA outcrop. Statistical summary of the estimates of gamma ray, porosity at atmospheric pressure, and permeability corrected by the Klinkenberg factor, in each main lithostratigraphic layer. Min, Max, and Mdn stand for the minimum, maximum, and median values, respectively. The total number of plugs for AA outcrop is equal to 172.

Lithofacies	Well	Gamma Ray ($nGyh^{-1}$)			Porosity (%)			Permeability (mD)		
		Min	Max	Mdn	Min	Max	Mdn	Min	Max	Mdn
Grainstones (AA-I)	AA-01	61.0	67.3	63.7	4.11	23.20	14.54	0.008	76.69	0.339
	AA-02	59.6	64.1	62.1	5.25	17.26	9.10	0.008	235.0	0.022
	AA-03	62.5	68.7	65.3	12.71	26.16	18.21	0.044	7.049	1.048
	AA-04	57.5	65.5	61.0	7.72	20.99	14.90	0.005	28.24	1.363
	AA-05	58.6	67.4	63.5	6.26	23.60	11.59	0.003	106.9	0.151
Recrystallized grainstone (AA-II)	AA-01	59.7	68.5	64.8	4.38	17.78	9.19	0.002	6.840	0.004
	AA-02	58.0	66.5	62.0	3.66	22.35	6.94	0.002	0.013	0.006
	AA-03	58.5	68.8	64.0	5.41	8.35	8.66	0.002	0.251	0.005
	AA-04	55.3	67.2	61.6	6.02	12.62	9.56	0.003	0.029	0.004
	AA-05	57.0	67.6	63.4	5.79	18.42	9.06	0.000	5.034	0.003

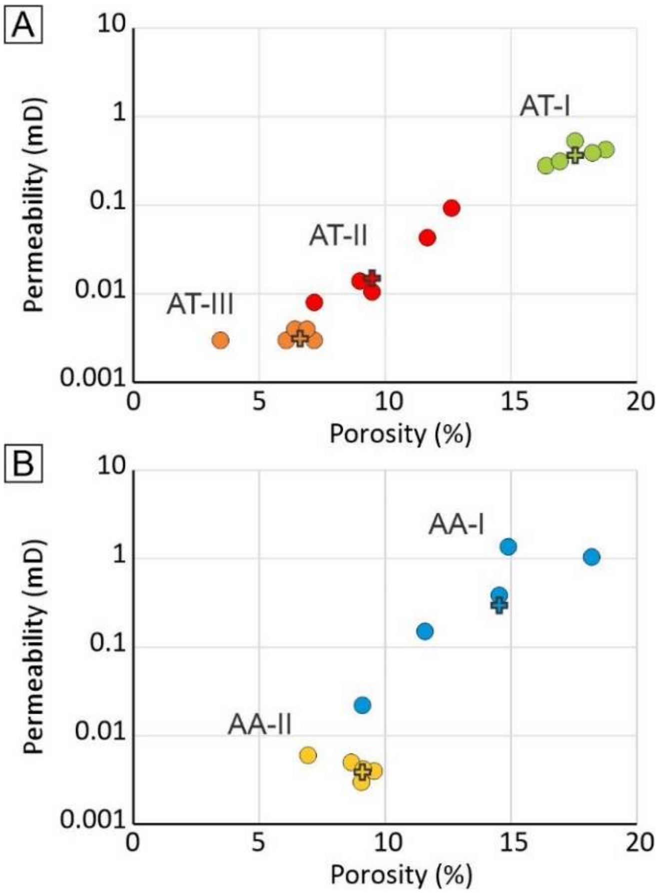

Figure 6: Cross-plot of porosity and permeability values for AT (A) and AA (B) outcrops. In each graph, the values are clustered according to the main lithostratigraphic layers identified in the two outcrops (see Fig. 3). The values for each cluster are shown as circles of the same color and the black cross in each cluster is the median value. Statistical summaries of the estimates are shown in Tables 1 and 2, for AT and AA outcrops, respectively.

3.4.3 Fracture networks

Using preferentially inlines and z-slices, fracture networks were identified based on the presence of persistent discontinuities in the GPR signal, such as small shifts in reflectors and/or narrow subvertical zones of attenuated signal (Fernandes Jr et al., 2015), as illustrated in Figs. 11A and 12A, for AT and AA outcrops, respectively. Furthermore, we pay more attention to laterally continuous non-stratabound fractures, as these discontinuities in general contribute more efficiently to fluid flow percolation, which plays a key role in karstification processes. The final results are shown in Figs. 11B and 12B, for AT and AA outcrops, respectively.

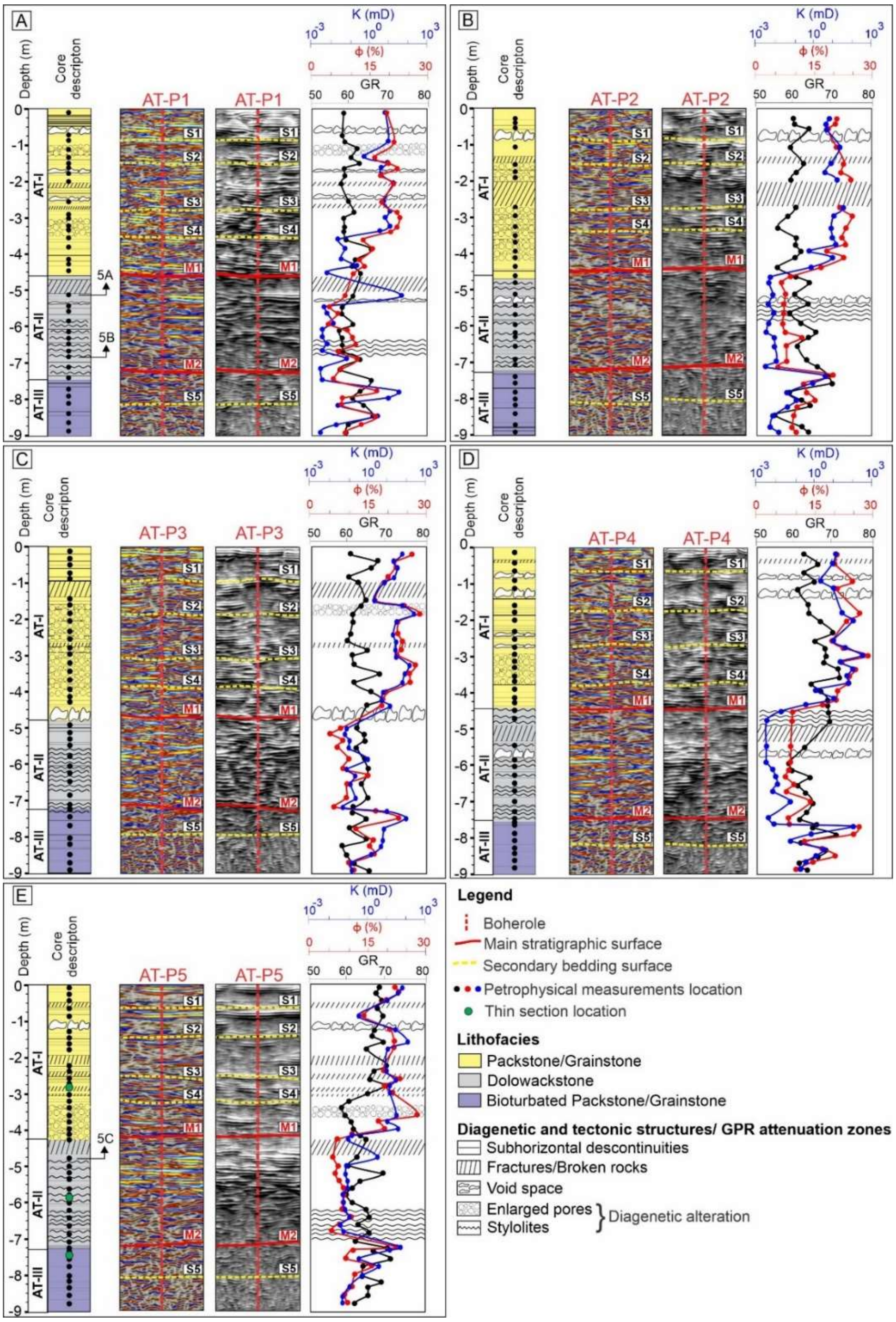

Figure 7: AT outcrop. Depth correlations of core logs with GPR images, permeability (k, mD), porosity (φ, %), and gamma ray (GR, nGyh^{-1}) profiles for boreholes AT-P1 (A), AT-P2 (B), AT-P3 (C), AT-P4 (D), and AT-P5 (E). Borehole locations are shown in Fig. 1C.

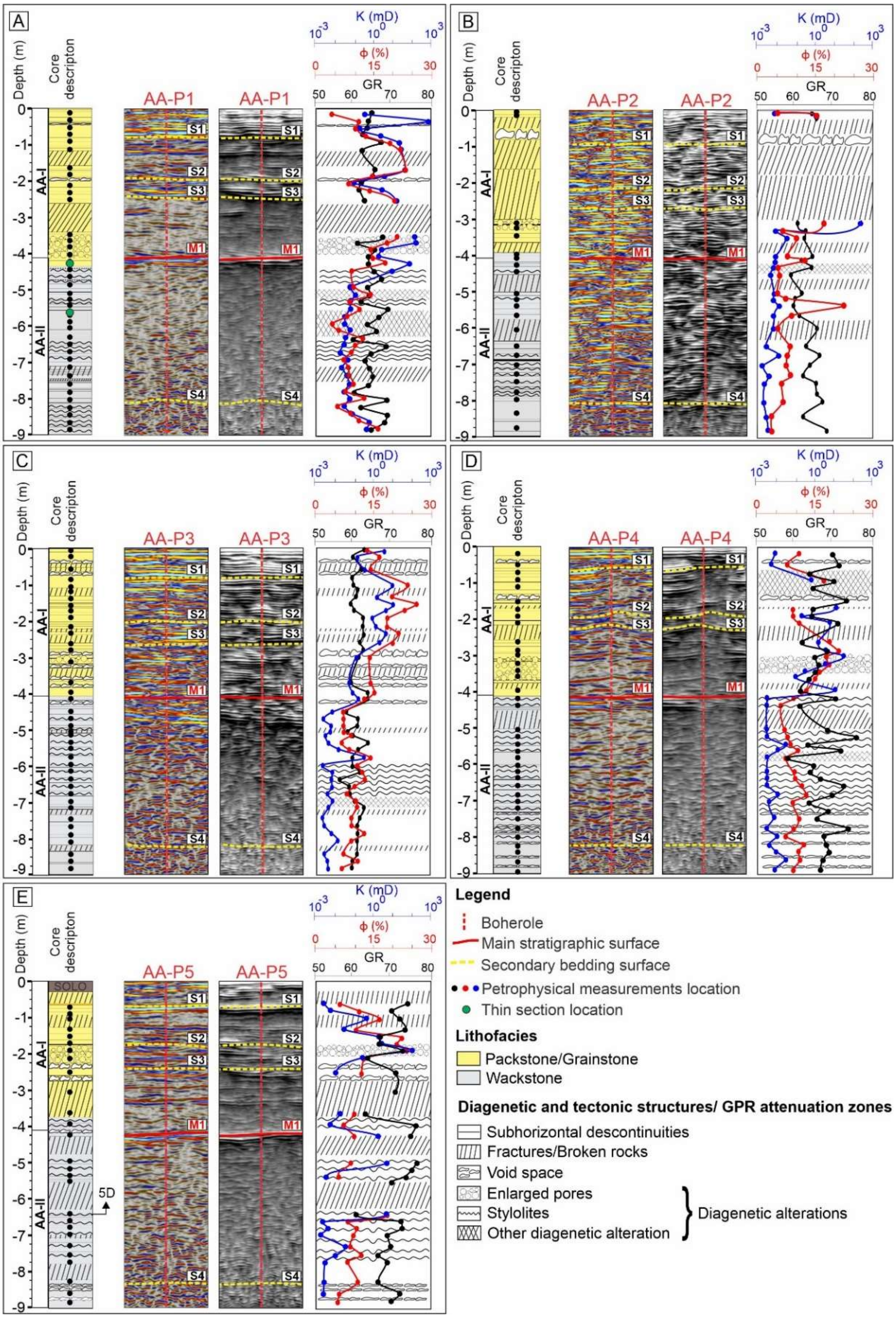

Figure 8: AA outcrop. Depth correlations of core logs with GPR images, permeability (k, mD), porosity (φ, %), and gamma ray (GR, $nGyh^{-1}$) profiles for boreholes AA-P1 (A), AA-P2 (B), AA-P3 (C), AA-P4 (D), and AA-P5 (E). Borehole locations are shown in Fig. 1D.

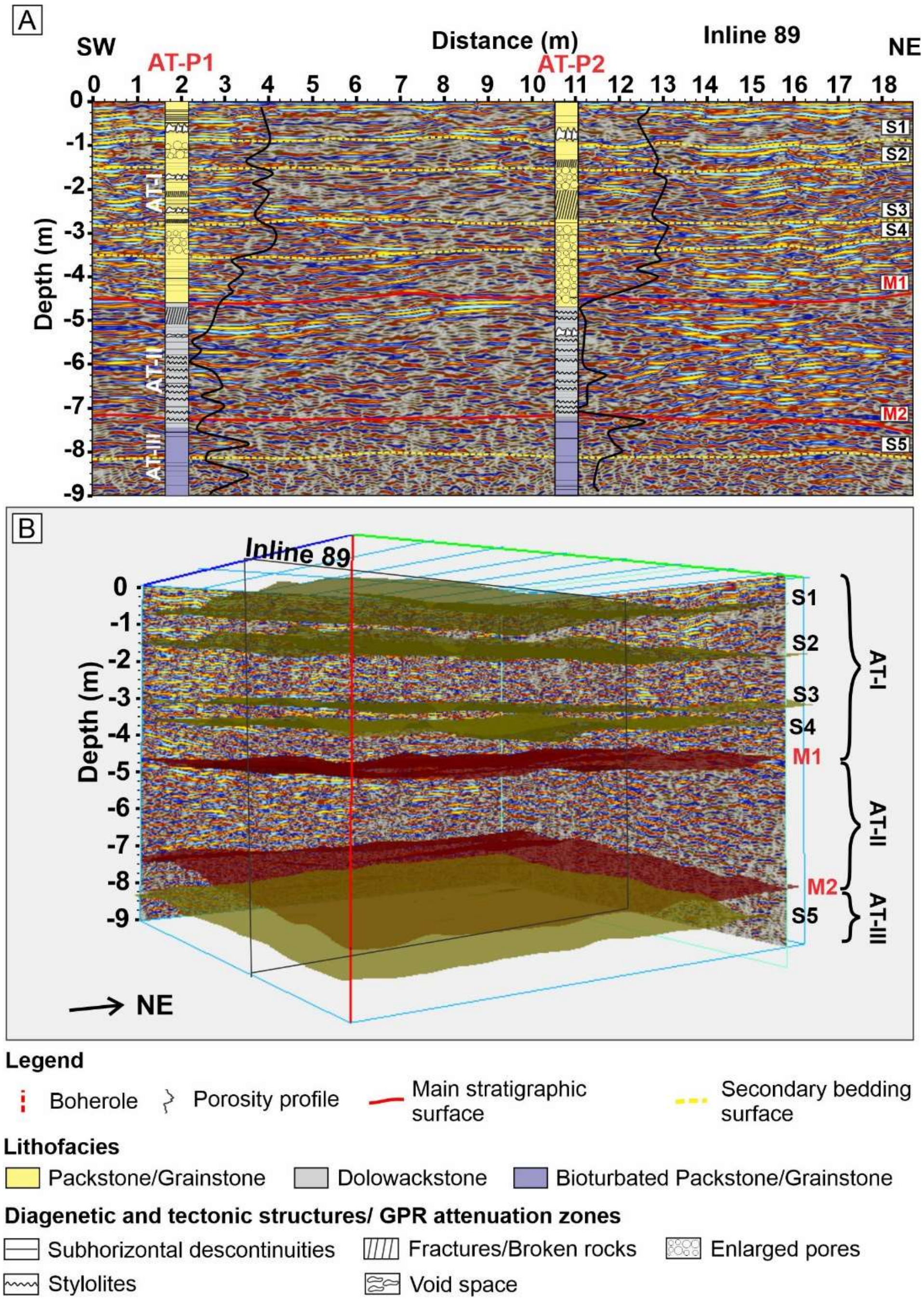

Figure 9: AT outcrop. GPR-based three-dimensional lateral extrapolation of the main lithostratigraphic layers AT-I, AT-II, and AT-III identified in the outcrop (see Fig. 3). (A) GPR Inline 89 superposed with the core log descriptions of boreholes AT-P1 and AT-P2 (locations in Fig. 1C), porosity profiles (black lines), main interfaces (M1 and M2, in red), and secondary interfaces (S1 to S5, in yellow). (B) 3D view of the interfaces highlighting that they are all sub-horizontal. The scaled porosity profiles are shown in Fig. 7.

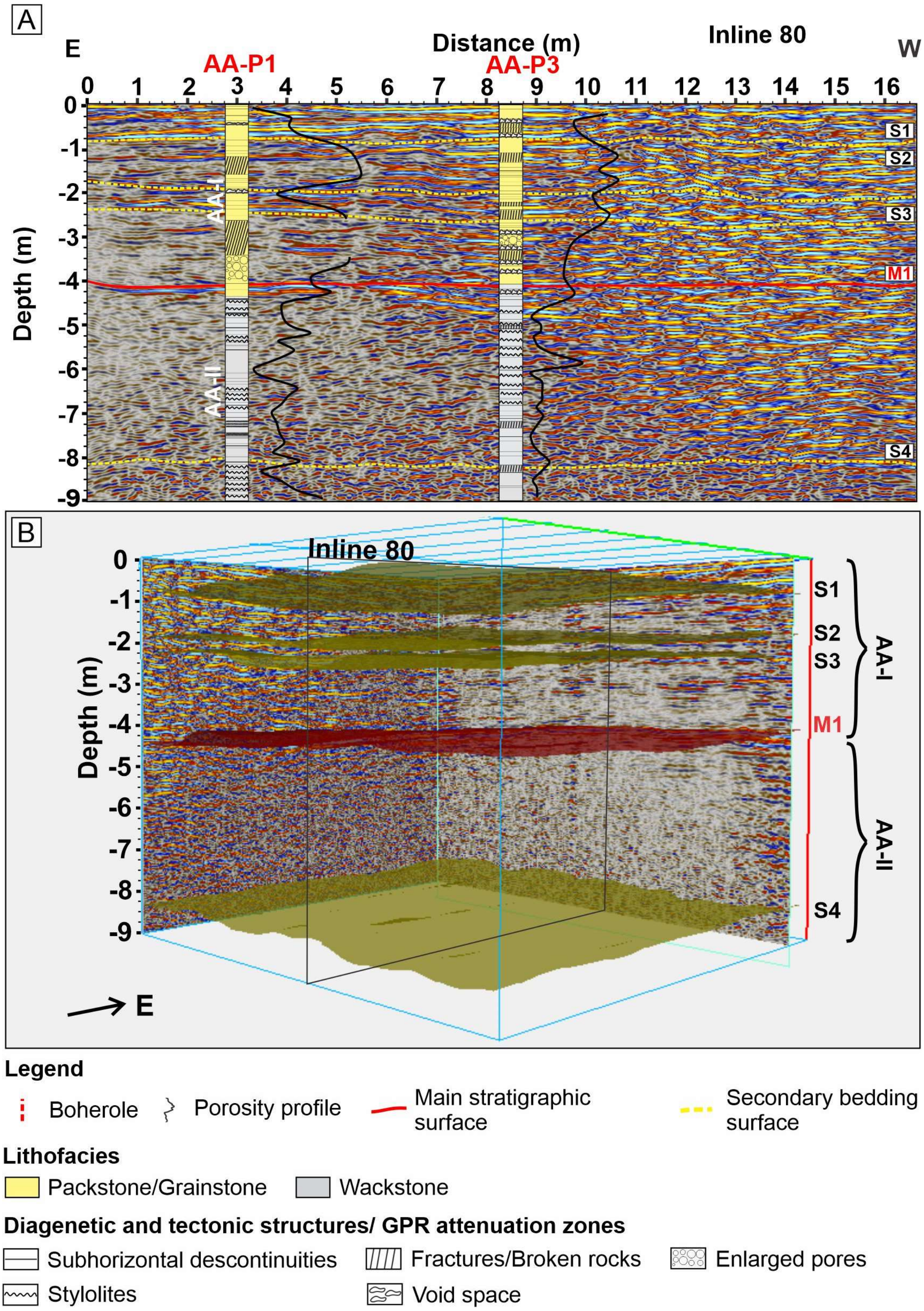

Figure 10: AA outcrop. GPR-based three-dimensional lateral extrapolation of the main lithostratigraphic layers AA-I and AA-II identified in the outcrop (see Fig. 3). (A) GPR Inline 80 superposed with the core log descriptions of boreholes AA-P1 and AA-P3 (locations in Fig.

1D), porosity profiles (black lines), main interface M1 (in red), and secondary interfaces (S1 to S4, in yellow). (B) 3D view of the interfaces highlighting that they are all sub-horizontal. The scaled porosity profiles are shown in Fig. 8.

In the 3D-AT GPR cube (Fig. 11B), the structural framework is dominantly formed by highly connected subvertical NNE-SSW fractures and incipient oblique faults striking NE-SE associated to their N-S conjugate antithetic fault segments. On the other hand, in the 3D-AA GPR cube (Fig. 12B), non-stratabound fractures exist only in the northeastern part of the outcrop. In particular, from two large NW-SE fractures, other small fractures branch into small flowers (Fig. 12B). Note that these structures are not connected with the fractures of the southwestern part of the outcrop, where stratabound fractures are most abundant (Fig. 12B).

The fracture networks interpreted in AT and AA outcrops are in general in accordance with the current tectonic regime (Miocene to the present) of the Potiguar Basin (Bezerra et al., 2020). However, the complexity of the structural network interpreted in the AT outcrop may be related to reactivations of pre-existing joints and stylolites, formed in the previous stress field (from Campanian to Miocene), as faults and splay fractures in a fragmentation zone.

3.4.4 3D delimitation of the attenuated zones of GPR signal

Also preferably using inlines and z-slices, GPR attenuation zones presenting high lateral continuity were delimited as contiguous volumes, which compose geobodies inside the GPR cubes, as exemplified in Fig. 13. The final results, shown in joint visions with fracture networks and litostratigraphic interfaces are given in Figs. 14 and 15, for AT and AA outcrops, respectively.

The obtained geobodies often present tabular shape and are delimited by subvertical fratures and litostratigraphic interfaces (Figs. 13-15). Boundary fractures can be either non-stratabound and stratabound, and boundary interfaces can be either major or secondary. In fact, we chose some of the secondary lithostratigraphic interfaces as the ones that separate the layers with marked contrast in the abundance of geobodies (Figs. 14B and 15B). In the 3D-AT GPR cube, the attenuation zones are concentrated in the AT-I layer (Fig, 14B). On the other hand, in the 3D-AA GPR cube, the attenuation zones are more dispersed, occupying about half of the cube volume, but concentrated in the eastern part of the cube around the two major non-stratabound fractures (compare Figs. 12B and 15B).

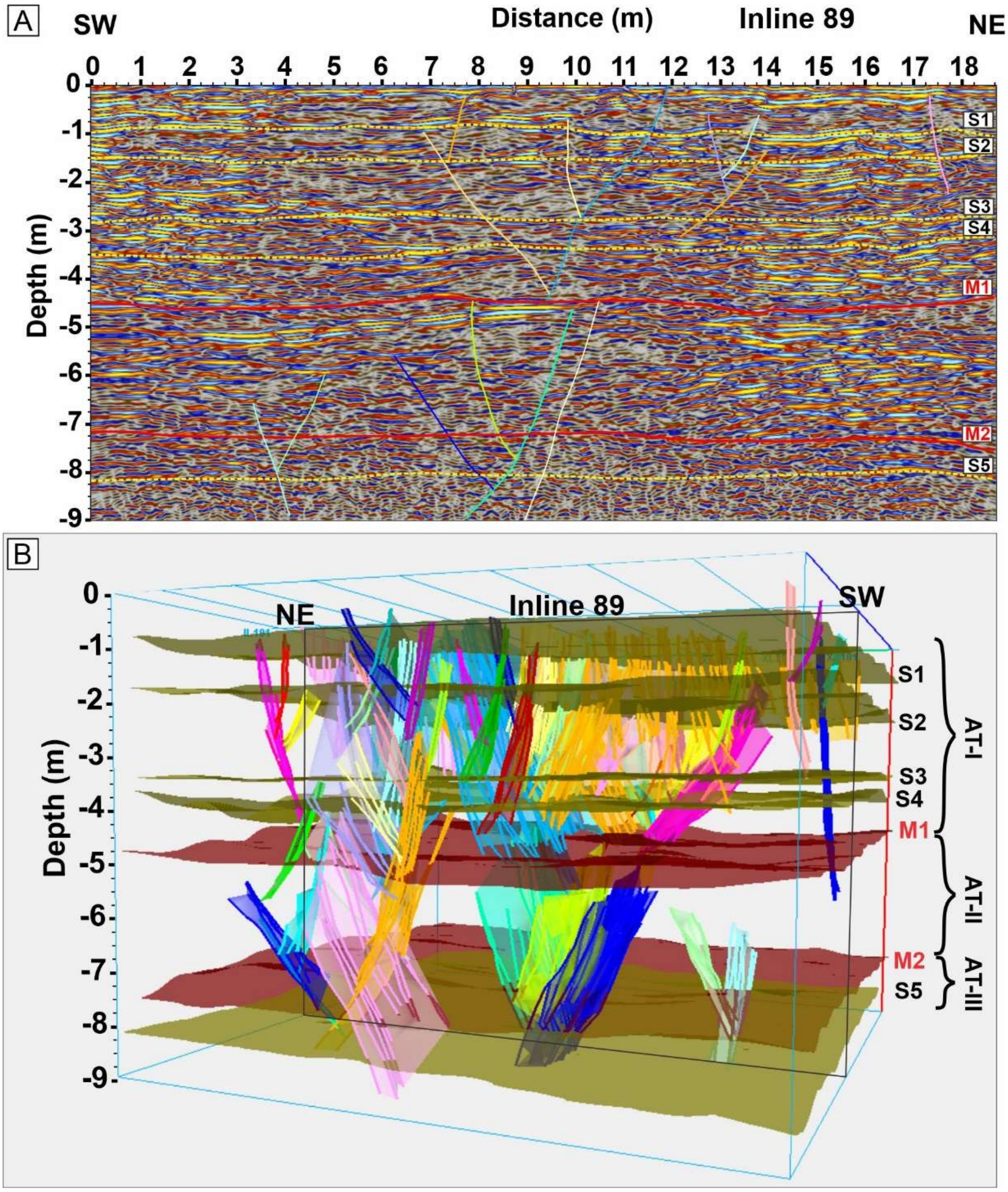

Figure 11: AT outcrop. Final interpretation of lithostratigraphic interfaces and fracture networks along GPR Inline 89 (A) and in 3D view (B). Note that the fractures are concentrated in the AT-I package, where they are very interconnected. The color used for the fractures are the same in Fig. 14.

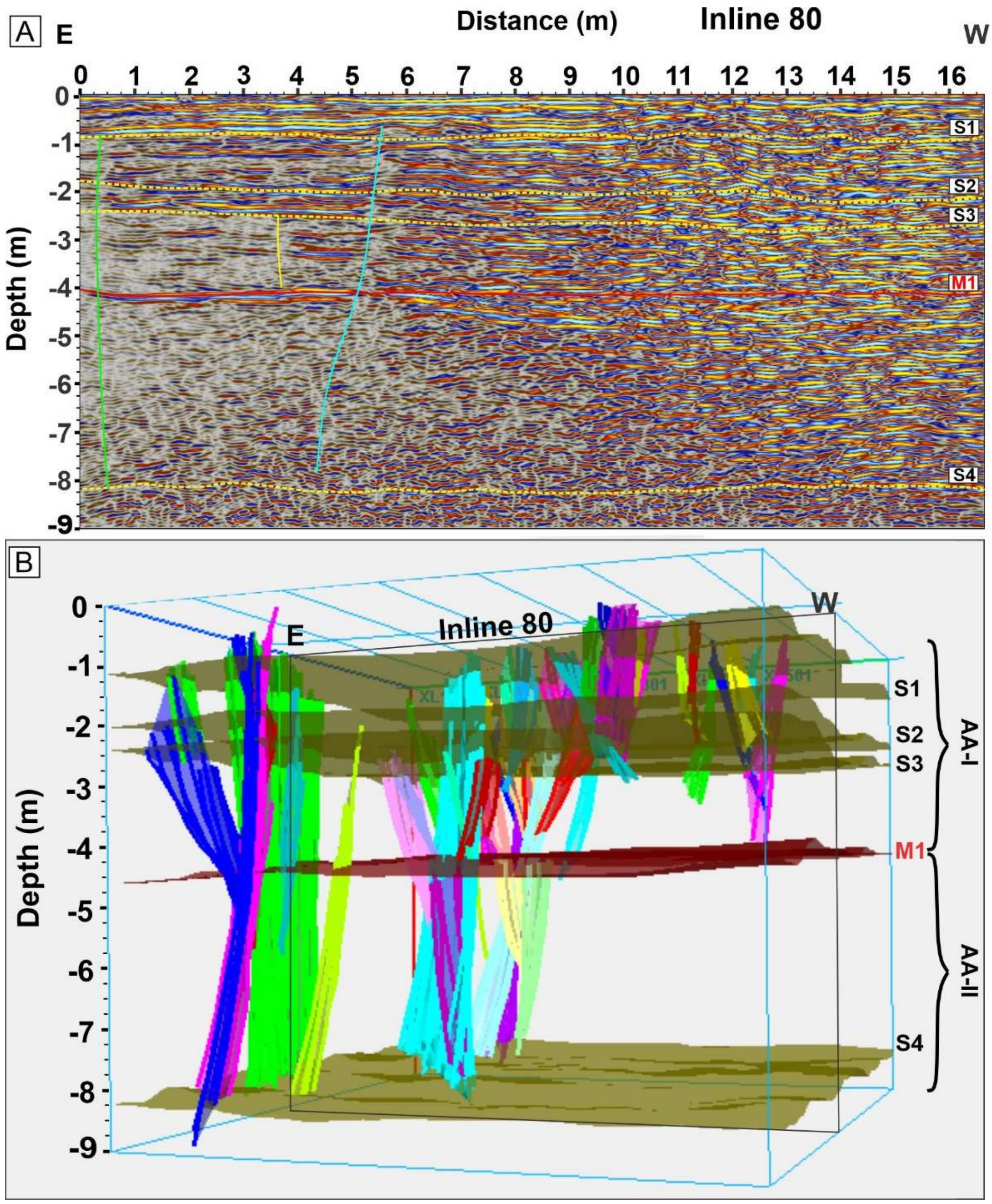

Figure 12: AA outcrop. Final interpretation of lithostratigraphic interfaces and fracture networks along GPR Inline 80 (A) and in 3D view (B). Note that most of the non-strata-bounded fractures are concentrated in the eastern part of the cube. The color used for the fractures are the same in Figs. 13 and 15.

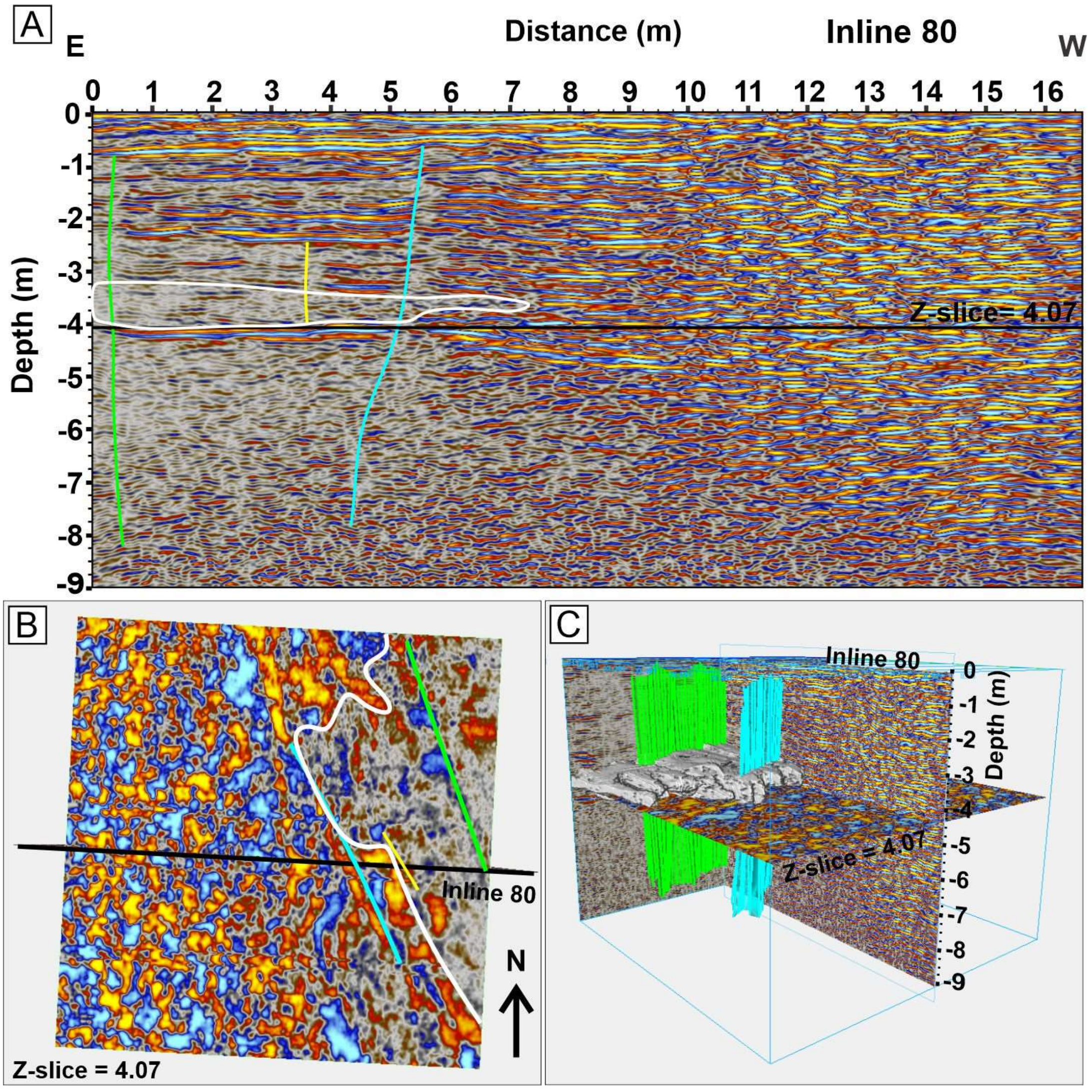

Figure 13: AA outcrop. Example of the 3D delimitation of a geobody composed by connected volumes of GPR attenuation zones. (A) GPR Inline 80 (location in Fig. 1D) superposed with an interpreted geobody (white contour) and fractures (in green and blue, for non-strata-bounded fractures and, in yellow, for a strata-bounded fracture). (B) GPR slice at depth equal to 4.07 m (black line in A) showing the same elements; note the high amplitude of the GPR reflector at the base of the delimited geobody, certainly caused by the strong contrast between rock and void space. (C) A chair view highlighting that the geobody has a tabular shape resulting from the fact that it is limited by subvertical fractures and subhorizontal lithostratigraphic interfaces. The color used for the fractures are the same in Figs. 12 and 15.

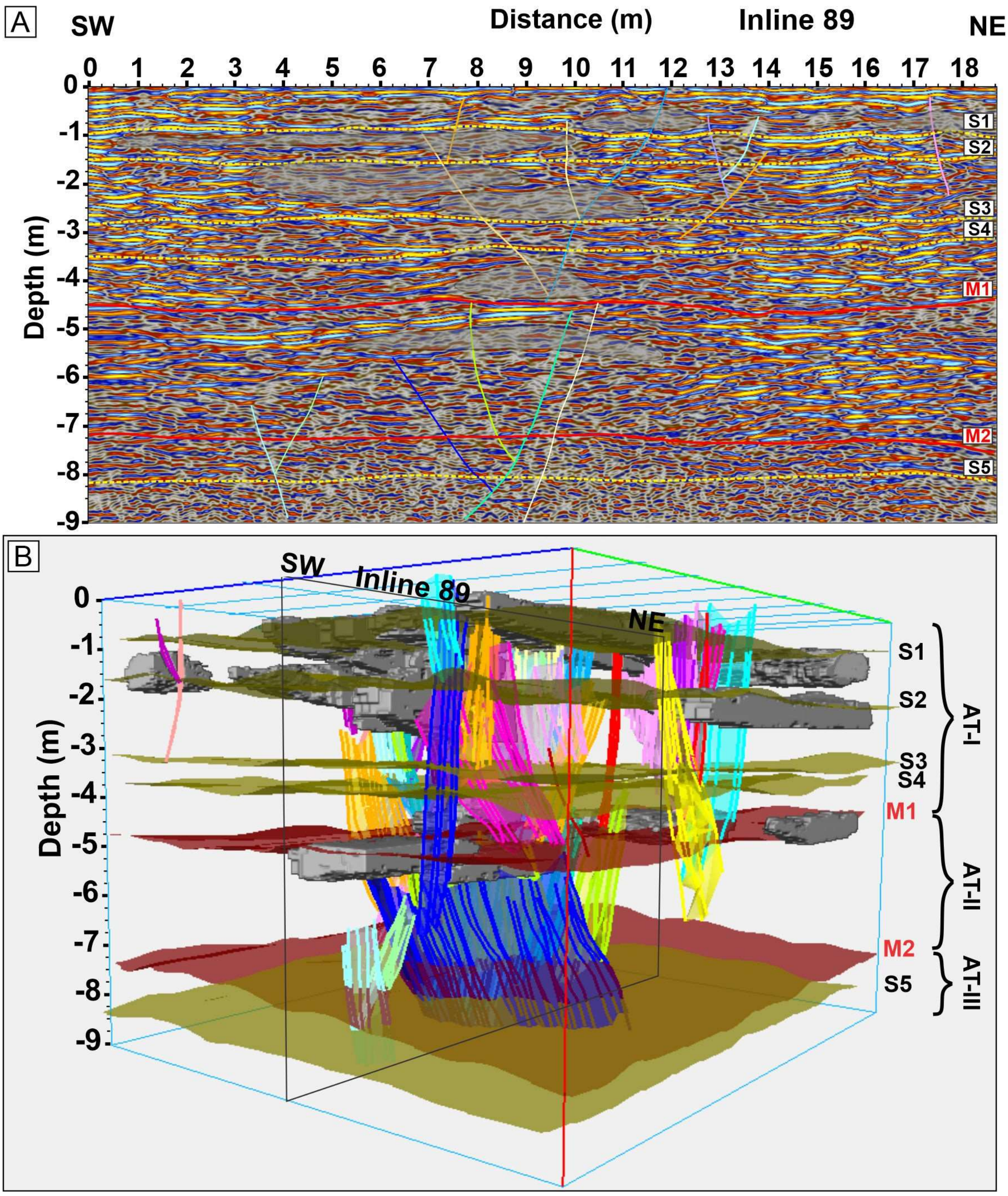

Figure 14: AT outcrop. Final interpretation of lithostratigraphic interfaces, fracture networks, and geobodies composed by connected volumes of GPR attenuation zones. (A) View along GPR Inline 89. (B) 3D view. Note that most geobodies are concentrated above the M1 interface, where fractures are abundant. For better visualization of the geobodies, (B) is shown in a different view of Figs. 12 and 14. The color used for the fractures are the same in Fig. 11.

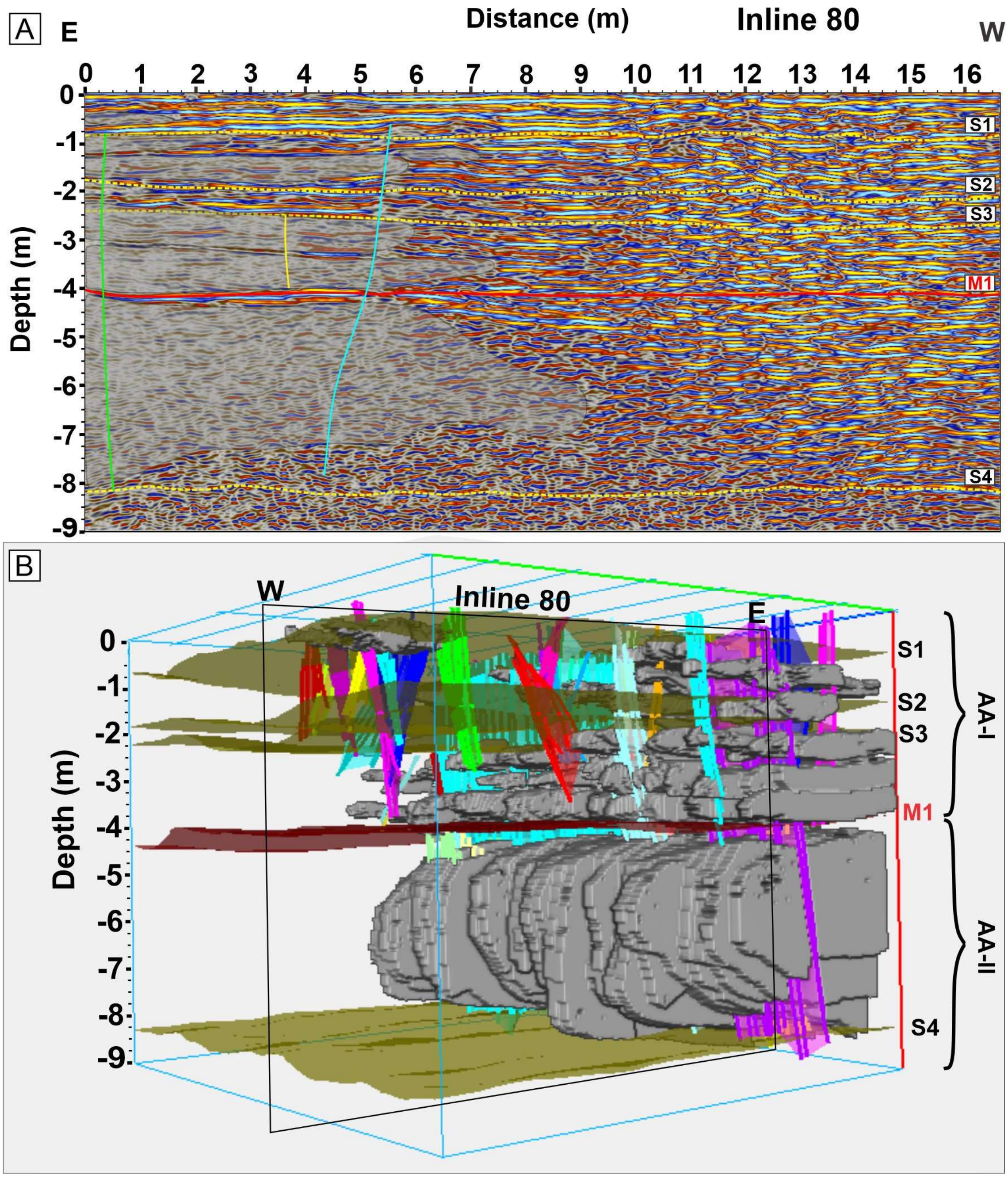

Figure 15: AA outcrop. Final interpretation of lithostratigraphic interfaces, fracture networks, and geobodies composed by connected volumes of GPR attenuation zones. (A) View along GPR Inline 80. (B) 3D view. Note that the geobodies are concentrated in the eastern part of the cube, where fractures are abundant. For better visualization of the geobodies, (B) is shown in a different view of Figs. 13 and 15. The color used for the fractures are the same in Fig. 12 and 13.

3.4.5 Causes of the GPR attenuation zones

By correlating GPR images with core descriptions, petrophysical profiles, and borehole wall photographs, we identified at least three causes for the GPR attenuation zones (Figs. 3, 7 and 8): fractured and/or broken zones affected by fracture enlargement due to dissolution, zones submitted to intense diagenetic alterations, and void spaces as a final end-member of these two processes. Regarding diagenetic alterations, two main types were identified: pore enlargement and stylolite dissolution.

Both in AT and AA outcrops, broken zones and void spaces appear dominantly in the shallowest packages AT-I and AA-I (Figs. 7 and 8). These packages concentrate fractures (Figs. 11 and 12) and present the highest relative values of porosity and permeability (Fig. 6 and Tables 1 and 2). In fact, some of the alteration zones of AT-I and AA-I packages are associated with high porosity and permeability values, when compared to the adjacent layers (Figs. 6-8). Thus, the associated GPR attenuation zones result both from fracture and pore enlargement, in a rock that certainly had relatively high primary matrix porosity. In the case of the AT outcrop, these shallow GPR attenuation zones are correlated with rock volumes with porosity and permeability greater than 10% and 0.01 mD, respectively, whilst in AA outcrop, with porosity and permeability greater than 5% and 0.001 mD, respectively.

To identify void spaces in GPR images, an important auxiliary diagnostic feature is the presence of strong reflection events at the void boundaries (Nobes, 2018), as exemplified in Fig. 3 (black rectangle, around 1 m depth) and Fig. 13 (strong reflection event at the bottom of the delimited geobody, around 4 m depth).

The attenuation zones related mainly to stylolite dissolution are concentrated in AT-II and AA-II packages (Figs. 14 and 15). Note that they are related to lithofacies of low porosity and permeability (Figs. 7 and 8, and Tables 1 and 2). Thus, the secondary porosity and permeability is mainly due to stylolite interconnection (Araújo et al., 2021), a fact that can be seen even in cores (Figs. 5A-B).

3.5. Discussion

3.5.1 Correlation of GPR attenuation zones with karstic alterations

The comparison of GPR images, core logs, porosity/permeability profiles, and borehole wall images was fundamental to identify the most important origins of GPR attenuation zones. The key result is that GPR attenuation zones in carbonate rocks are mainly related to secondary alterations, either of mechanical origin (fracturing) and/or diagenetic alterations due to karstic dissolution, as fracture/pore enlargement and dissolution of veins and stylolites. Both cases can result in void space creation. Table 3 summarizes our findings about the main factors that control temporal karst evolution in fractured carbonate rocks. To remain close to the actual conditions we found in our study area, only primary matrix porosity/permeability and presence of stylolites compose the initial conditions.

The summary presented in Table 3 agrees with both the results of Araújo et al. (2021) and Bagni et al. (2022). Araújo et al. (2021) studied outcropping rocks located approximately 20 km from our area. The analyzed carbonates by Araújo et al. (2021) include mostly packstones and grainstones, which present bed-parallel stylolites and microfractures caused by compaction and vertical upload. These structures were dissolved by water percolation, forming dissolution features such as vugs and channels. As in the outcrops studied by Araújo et al. (2021), the shallowest layers of our outcrops also present vugs and channels that were identified in the walls of drilled boreholes (Fig. 3C). On the other hand, Bagni et al. (2022) characterized regionally the subtidal deposits outcropping in our study area and described that millimeter to centimeter vuggy porosity occur. According to Araújo et al. (2021) and Bagni et al. (2022), this secondary porosity is particularly concentrated along connected discontinuities, such as fractures, stylolites, and stratifications, which is accordance with the fact that GPR attenuation zones compose tabular geobodies delimited by fractures and subhorizontal interfaces.

A study carried out by Cunningham et al. (2004), in the subtidal deposits of the Biscayne Aquifer, associated GPR attenuation zones with high matrix porosity and pore enlargement. Besides this effect, our results evidence that GPR attenuation zones can occur even in low porosity and permeability layers, if karstic dissolution promoted dissolution and connection of stylolites and veins, besides additional fracture/pore enlargement.

Several studies have already demonstrated the ability of the GPR method to image fractures and karst features in carbonate rocks (e.g. Anchuela et al., 2009; Grasmueck et al., 2013; Fernandes et al., 2015; Olivera Jr. et al., 2020). In particular, void spaces can be identified in GPR images as anomalous low amplitude zones, usually related to the presence of multiple reflections, and limited by high-amplitude signal reflectors (Nobes, 2018). Top and/or bottom reflections from air-filled voids might be seen, as already described in Figs. 3 and 13, but often they cannot be recognized because void thickness might be small, thus causing overlapping of top and bottom reflections, as discussed by Nobes (2018). As an example, minor void spaces detected in borehole AA-P2 cannot be identified in GPR images (Fig. 8B).

Table 3: Schematic description of the dependence of karst development on some initial conditions in fractured carbonate rocks. We restricted the initial conditions to primary matrix porosity/permeability and presence of stylolites.

Primary matrix porosity/permeability	**Without stylolites**	**With stylolites**
Low	Relatively minor development of secondary porosity/permeability	Stylolites are dissolved. Connected volumes of open and/or partially dissolved stylolites might compose high permeability zones
High	Pores are enlarged. Connected volumes of relatively high porosity might compose high permeability zones	Pores are enlarged and stylolites are dissolved. Connected volumes of relatively high porosity and open and/or partially dissolved stylolites might compose high permeability zones. Relatively higher probability of void creation

The attenuation of GPR signals due to partially filled enlarged fractures and karst features is caused by dielectric dispersion effects (Xavier Neto and Medeiros, 2006; Fernandes et al., 2015; Oliveira et al., 2020) and can be adequately modeled as zones of relatively low Q-quality factor (Santos et al., 2022). In fact, Q values are quite sensitive to petrophysical parameters, such as porosity, permeability and clay and/or water contents (Wunderlich and Rabbel, 2011; Akbar, 2019). Note that GPR attenuation zones might occur even above water level due to water adsorption to grains (McMechan et al., 2002; Harbi and McMechan, 2011). In this sense, in the AA-II package the attenuation effect is greater than in the AT-II package, since the grain size in the first is relatively smaller since the AT-II package has undergone intense recrystallization.

3.5.2 Implications for thief zones development in carbonate reservoirs

Several studies highlight the structural control in the development of karst features (e.g. Pepe and Parise, 2014; Privalov et al., 2019; Bagni et al., 2020; La Bruna et al., 2021; Araújo et al., 2021; Pisani et al., 2022). Our 3D approach made this control even more evident, as GPR cubes allowed us to visualize the spatial geometric relationships of fracture networks, lithostratigraphic interfaces, karst alteration zones and voids.

The karst dissolution zones evolved similarly in the two outcrops. This is certainly a consequence of the fact that the two outcrops are located in the same stratigraphic unit (subtidal deposits), only 400 m apart, and related to the same regional structural control associated with the Apodi Fold. The minor discrepancies are mainly related to different characteristics of the local fracture networks, which influenced fluid flow locally and, as a result, the karst development. We summarize in Fig. 16 the common aspects of the temporal karst development found in AT and AA outcrops. Because the pointed controls act also in the reservoir scale, this conceptual evolution model might be also applied for this scale. The key message is that geobodies of connected volumes of karstic altered zones commonly present tabular shape and are delimited by subvertical fractures and subhorizontal lithostratigraphic interfaces. The resulting tabular geobodies might compose highly connected permeable volumes of altered carbonate rocks, thus constituting thief zones or super-K layers in carbonate reservoirs.

Our findings are in accordance with known results about thief zones in carbonates as, for example, the results of Li et al. (2010), Yixiang et al. (2017), and Liu et al. (2021). According to Li et al. (2010), in the Mauddud carbonate reservoirs, located in Sabiriyah field (Kuwait), the main thief zones developed in two types of layers: a) high porosity layers with vuggy porosity and dissolved channels and b) low porosity fractured layers. The layers that compose the thief zones in the Mauddud reservoir have similar characteristics to the units described in the AT and AA outcrops. The main difference is that, in the case of AT-II and AA-II units, the partially dissolved bed-parallel stylolites play a similar role as fractures in the Mauddud reservoir. In turn, Yixiang et al. (2017) showed that, in the Mishrif carbonate formation of Rumaila oil field (Iraq), thief zones developed in coarse lithofacies, such as grainstones and packstones, with porosity ranging from 18 to 30%. In our study area, porosity of the packstones/grainstones layers reach similar values (26%). Finally, Liu et al. (2021) pointed that thief zones are associated with sedimentary units of relatively high porosity/permeability, when compared to adjacent layers. In this sense, factors influencing the creation of secondary porosity, such as fracturing and karst dissolution, might contribute to significantly increase permeability (Bagni et al., 2020; Araújo et al., 2021), thus leading to the formation of thief zones of secondary origin.

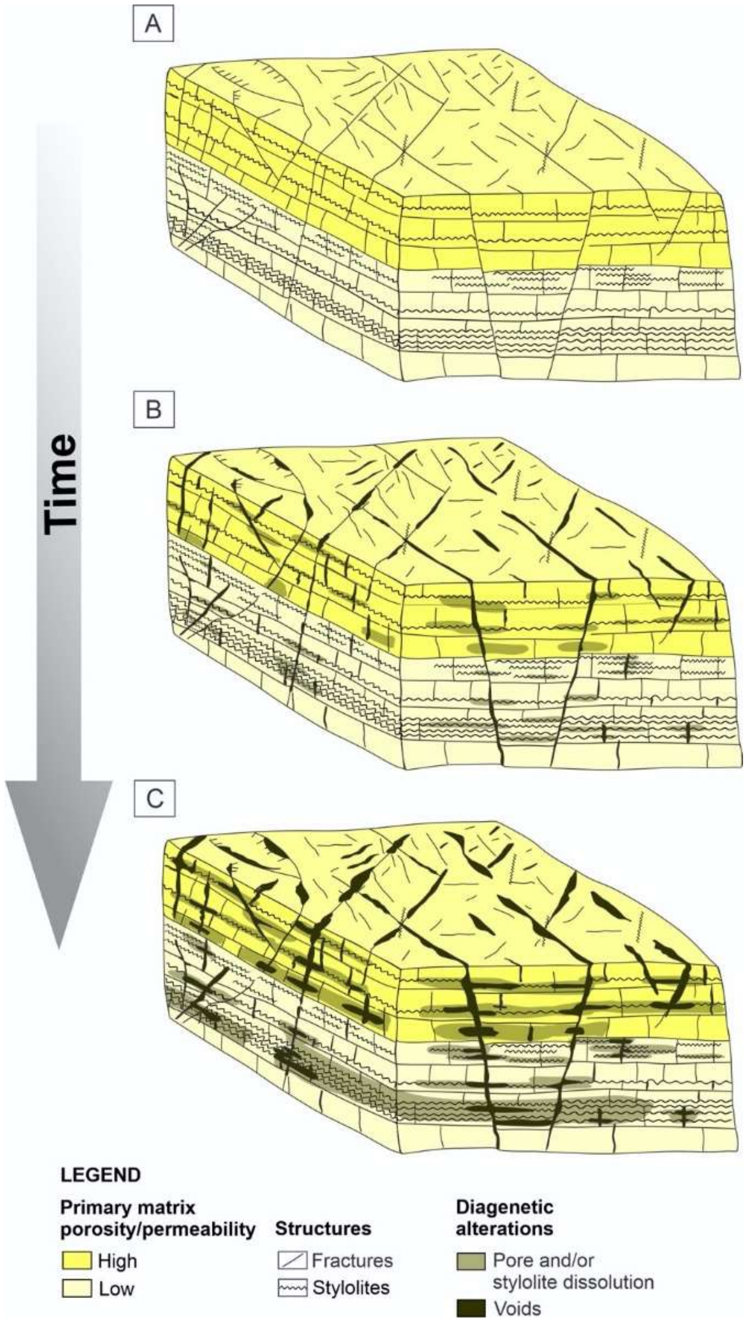

Figure 16: Conceptual block diagrams showing the time evolution of karstic alterations in carbonate rocks. In (A), fracture/fault networks are implanted. Because fractures are preferential routes to fluid flow, in both epigenic and hypogenic karst environments, dissolution process is facilitated (B), particularly along fractures and layers having high values of primary matrix porosity/permeability and/or high concentration of stylolites. As time passes, fracture enlargement and pore/stylolite dissolution might occur, thus leading to the development of relatively high secondary porosity/permeability zones (C), resulting from connected volumes of rocks containing dissolved pores and/or stylolites, in the last case even in layers where

primary values of porosity/permeability might be low. The resulting bodies often present tabular shapes because they are delimited by fractures and subhorizontal lithostratigraphic interfaces. In the reservoir scale, these tabular geobodies might constitute thief zones or super-K layers.

3.6 Conclusions

The joint interpretation of GPR cubes, core logs, porosity/permeability profiles, and borehole wall images allow to identify that GPR attenuation zones in carbonate rocks are mainly related to secondary alterations. The origin can be either fracturing or diagenetic processes, such as fracture/pore enlargement and dissolution of veins and stylolites. Both cases can result in void space creation. The 3D characterization approach we used revealed the spatial geometric relationships between karst alteration zones, fracture networks and lithostratigraphic interfaces.

Triggered by fluid flow, particularly in fractures, most of the dissolution processes develop in layers which have high values of primary matrix porosity and/or high concentration of stylolites. As a result, enlarged fractures/pores and dissolved stylolites can create highly connected permeable volumes of altered carbonate rocks. In the case of high concentration of stylolites, these connected rock volumes might develop even in layers having low primary values of porosity and permeability.

The resulting connected permeable volumes of altered carbonate rocks often present tabular shapes because they are delimited by subvertical fractures and subhorizontal lithostratigraphic interfaces. In the reservoir scale, these tabular bodies might constitute thief zones or super-K layers.

Acknowledgments

This research was carried out in association with the ongoing R&D project registered as ANP 20502–1, "Processos e Propriedades em Reservatórios Carbonáticos Fraturados e Carstificados – POROCARSTE 3D" (UFRN/UNB/UFRJ/UFC/Shell Brasil/ANP) – Porokarst – Processes and Properties in Fractured and Karstified Carbonate Reservoirs, sponsored by Shell Brasil under the ANP R&D levy as "Compromisso de Investimento com Pesquisa e Desenvolvimento". The Brazilian agency CNPq is thanked for the research fellowships and associated grants provided to WEM and FHRB. Besides financial support from the INCT-GP/CNPq/CAPES to purchase the computational infrastructure used in this study. We thank Antônio Vicente and Bruno Baraúna for their support in acquiring the GPR data.

References

Akbar, N.M.A., 2019. New Approaches of Porosity-Permeability Estimations and Quality Factor Q Characterization based on Sonic Velocity , Critical Porosity , and Rock Typing. https://doi.org/10.2118/199777-STU

Anchuela, Ó.P., Casas-Sainz, A.M., Soriano, M.A., Pocoví-Juan, A., 2009. Mapping subsurface karst features with GPR: Results and limitations. Environ. Geol. 58, 391–399. https://doi.org/10.1007/s00254-008-1603-7

Araújo, R.E.B., La Bruna, V., Rustichelli, A., Bezerra, F.H.R., Xavier, M.M., Audra, P., Barbosa, J.A., Antonino, A.C.D., 2021. Structural and sedimentary discontinuities control the generation of karst dissolution cavities in a carbonate sequence, Potiguar Basin, Brazil. Mar. Pet. Geol. 123. https://doi.org/10.1016/j.marpetgeo.2020.104753

Bagni, F.L., Bezerra, F.H., Balsamo, F., Maia, R.P., Dall'Aglio, M., 2020. Karst dissolution along fracture corridors in an anticline hinge, Jandaíra Formation, Brazil: Implications for reservoir quality. Mar. Pet. Geol. 115, 104249. https://doi.org/10.1016/j.marpetgeo.2020.104249

Bagni, F.L., Erthal, M.M., Tonietto, S.N., Maia, R.P., Bezerra, F.H., Balsamo, F., Córdoba, V.C., de Souza, F.G., Brod, J.A., Fernandes, C.P., Fonseca, J.P.T., 2022. Karstified layers and caves formed by superposed epigenic dissolution along subaerial unconformities in carbonate rocks – Impact on reservoir-scale permeability. Mar. Pet. Geol. 138. https://doi.org/10.1016/j.marpetgeo.2022.105523

Becker, I., Koehrer, B., Waldvogel, M., Jelinek, W., Hilgers, C., 2018. Comparing fracture statistics from outcrop and reservoir data using conventional manual and t-LiDAR derived scanlines in Ca2 carbonates from the Southern Permian Basin, Germany. Mar. Pet. Geol. 95, 228–245. https://doi.org/10.1016/j.marpetgeo.2018.04.021

Bertotti, G., de Graaf, S., Bisdom, K., Oskam, B., Vonhof, H.B., H. R. Bezerra, F., J. G. Reijmer, J., L. Cazarin, C., 2017. Fracturing and fluid-flow during post-rift subsidence in carbonates of the Jandaíra Formation, Potiguar Basin, NE Brazil. Basin Res. 29, 836–853. https://doi.org/10.1111/bre.12246

Bezerra, F.H., de Castro, D.L., Maia, R.P., Sousa, M.O.L., Moura-Lima, E.N., Rossetti, D.F., Bertotti, G., Souza, Z.S., Nogueira, F.C.C., 2020. Postrift stress field inversion in the Potiguar Basin, Brazil – Implications for petroleum systems and evolution of the equatorial margin of South America. Mar. Pet. Geol. 111, 88–104. https://doi.org/10.1016/j.marpetgeo.2019.08.001

Bulhões E.M., 1999, Técnica "Volume de Amplitudes" para mapeamento de feições estruturais: 6th International Congress of the Brazilian Geophysical Society, SBGf, no. 296, Expanded Abstract, 1–4. [In Portuguese]

Bulhões E.M. and Amorim W.N., 2005, Princípio da sismocamada elementar e sua aplicação técnica de volume de amplitudes (TecVA): 9th International Congress of the Brazilian Geophysical Society & EXPOGEF, SBGf, pp. 1382–1387. [In Portuguese]

Conti, I.M.M., de Castro, D.L., Bezerra, F.H.R., Cazarin, C.L., 2019. Porosity Estimation and Geometric Characterization of Fractured and Karstified Carbonate Rocks Using GPR Data in the Salitre Formation, Brazil. Pure Appl. Geophys. 176, 1673–1689. https://doi.org/10.1007/s00024-018-2032-5

Córdoba, V.C., 2001, A evolução da plataforma carbonática Jandaíra durante o Neocretáceo na Bacia Potiguar: Análise paleoambiental, diagenética e estratigráfica. PhD Thesis. Universidade Estadual Paulista (UNESP).

Cross, N.E., van Veen, L.J., Al-Enezi, A., Singh, S., van Beusekom, G., 2021. Seismic Geomorphology of Karst in Cretaceous to Early Cenozoic Carbonates of North Kuwait. Mar. Pet. Geol. 128, 104947. https://doi.org/10.1016/j.marpetgeo.2021.104947

Cunningham, K.J., 2004. Application of ground-penetrating radar, digital optical borehole images, and cores for characterization of porosity hydraulic conductivity and paleokarst in the Biscayne aquifer, southeastern Florida, USA. J. Appl. Geophys. 55, 61–76. https://doi.org/10.1016/j.jappgeo.2003.06.005

de Castro, D.L., Bezerra, F.H.R., Sousa, M.O.L., Fuck, R.A., 2012. Influence of Neoproterozoic tectonic fabric on the origin of the Potiguar Basin, northeastern Brazil and its links with West Africa based on gravity and magnetic data. J. Geodyn. 54, 29–42. https://doi.org/10.1016/J.JOG.2011.09.002.

de Graaf, S., Reijmer, J.J.G., Bertotti, G. V., Bezerra, F.H.R., Cazarin, C.L., Bisdom, K., Vonhof, H.B., 2017. Fracturing and calcite cementation controlling fluid flow in the shallow-water carbonates of the Jandaíra Formation, Brazil. Mar. Pet. Geol. 80, 382–393. https://doi.org/10.1016/j.marpetgeo.2016.12.014

Dunham, R.J., 1962. Classification of carbonate rocks according to depositional textures. In: Classification of Carbonate Rocks According to Depositional Textures. AAPG Special Volumes, pp. 108–121.

Embry, A.F., Klovan, J.E., 1971. A late devonian reef tract on north-eastern banks island. Bull. Can. Petrol. Geol. 19, 730–781.

Fernandes, A.L., Medeiros, W.E., Bezerra, F.H.R., Oliveira, J.G., Cazarin, C.L., 2015. GPR investigation of karst guided by comparison with outcrop and unmanned aerial vehicle imagery. J. Appl. Geophys. 112, 268–278. https://doi.org/10.1016/j.jappgeo.2014.11.017

Ghobadi, R., 2016. Geostatistical modelling and simulation of karst systems. Sch. Civil, Environ. Min. Eng. Master, 114.

Giuffrida, A., La Bruna, V., Castelluccio, P., Panza, E., Rustichelli, A., Tondi, E., Giorgioni, M., Agosta, F., 2019. Fracture simulation parameters of fractured reservoirs: Analogy with outcropping carbonates of the Inner Apulian Platform, southern Italy. J. Struct. Geol. 123, 18–41. https://doi.org/10.1016/j.jsg.2019.02.007

Grasmueck, M., Quintà, M.C., Pomar, K., Eberli, G.P., 2013. Diffraction imaging of sub-vertical fractures and karst with full-resolution 3D Ground-Penetrating Radar. Geophys. Prospect. 61, 907–918. https://doi.org/10.1111/1365-2478.12004

Guidry, S.A., Grasmueck, M., Carpenter, D.G., Gombos, A.M., Bachtel, S.L., Viggiano, D.A., 2007. Karst and early fracture networks in carbonates, Turks and Caicos Islands, British West Indies. J. Sediment. Res. 77, 508–524. https://doi.org/10.2110/jsr.2007.052

Gutmanis, J., I Oró, L.A., DíEz-Canseco, D., Chebbihi, L., Awdal, A., Cook, A., 2017. Fracture analysis of outcrop analogues to support modelling of the subseismic domain in carbonate reservoirs, south-central Pyrenees. Geol. Soc. Spec. Publ. 459, 139–156. https://doi.org/10.1144/SP459.2

Harbi, H., McMechan, G.A., 2011. Modeling 3D porosity and permeability from GPR data in the Ellenburger Dolomite, central Texas. Geophysics 76. https://doi.org/10.1190/geo2011-0051.1

Howell, J.A., Martinius, A.W., Good, T.R., 2014. The application of outcrop analogues in geological modelling: a review, present status and future outlook. Geol. Soc. London, Spec. Publ. 387, 1–25. https://doi.org/10.1144/sp387.12

Huang, F., Yao, C., Yang, J., He, C., Shao, Y., Zhou, C., 2020. Connectivity evaluation of fracture networks considering the correlation between trace length and aperture. Appl. Math. Model. 88, 870–887. https://doi.org/10.1016/j.apm.2020.07.011

Jahnert, R., de Paula, O., Collins, L., Strobach, E., Pevzner, R., 2012. Evolution of a coquina barrier in Shark Bay, Australia by GPR imaging: Architecture of a Holocene reservoir analog. Sediment. Geol. 281, 59–74. https://doi.org/10.1016/j.sedgeo.2012.08.009

Jones, G.D., 2015. Flow-Based Effective Properties of Sub-Seismic Karst Karst Flow-Based Properties Geologic Modeling Workflow Overview 8–11. https://doi.org/10.2118/172648-MS

Klinkenberg, L.J., 1941. The permeability of porous media to liquids and gases. In: Drilling and Production Practice. American Petroleum Institute.

La Bruna, V., Bezerra, F.H.R., Souza, V.H.P., Maia, R.P., Auler, A.S., Araujo, R.E.B., Cazarin, C.L., Rodrigues, M.A.F., Vieira, L.C., Sousa, M.O.L., 2021. High-permeability zones in folded and faulted silicified carbonate rocks – Implications for karstified carbonate reservoirs. Mar. Pet. Geol. 128, 105046. https://doi.org/10.1016/j.marpetgeo.2021.105046

Li, B., Najeh, H., Lantz, J., Rampurawala, M.A., Gok, I., Al-Khabbaz, M., 2010. Detecting thief zones in carbonate reservoirs by integrating borehole images with dynamic measurements: Case study from the mauddud reservoir, north Kuwait. SPE Reserv. Eval. Eng. 13, 193–202. https://doi.org/10.2118/116286-PA

Li, D., Yang, J., Lu, D., 2016a. Thief zone identification based on transient pressure analysis: a field case study. J. Pet. Explor. Prod. Technol. 6, 63–72. https://doi.org/10.1007/s13202-015-0168-8

Li, C., Xu, P., Qiu, S., Zhou, Y., 2016b. The gas effective permeability of porous media with Klinkenberg effect. J. Nat. Gas Sci. Eng. 34, 534–540. https://doi.org/10.1016/j.jngse.2016.07.017.

Liu, H., Shi, K., Liu, B., Song, X., Deng, L., Guo, R., Tian, Z., Li, Y., Deng, Y., Wang, G., 2021. The characteristics and origins of thief zones in the Cretaceous limestone reservoirs of Central and southern Mesopotamian Basin. J. Pet. Sci. Eng. 201, 108395. https://doi.org/10.1016/j.petrol.2021.108395

Lopes, J.A.G., Medeiros, W.E., La Bruna, V., Lima, A. De, Bezerra, F.H.R., Schiozer, D.J., 2022. Advancements towards DFKN modelling : Incorporating fracture enlargement resulting from karstic dissolution in discrete fracture networks. J. Pet. Sci. Eng. 209. https://doi.org/10.1016/j.petrol.2021.109944

Lu, X., Wang, Y., Yang, D., & Wang, X. (2020). Characterization of paleo-karst reservoir and faulted karst reservoir in Tahe Oilfield, Tarim Basin, China. Advances in Geo-Energy Research, 4(3), 339. https://10.46690/ager.2020.03.11.

Lucia, F.J., 2007. Carbonate Reservoir Characterization: an Integrated Approach, second ed. Springer-Verlag Berlin Heidelberg. https://doi.org/10.1007/978-3-540-72742-2.

Matos, R.M.D. De, 1992. The Northeast Brazilian Rifte System. Tectonics 11, 766–791.

McMechan, G.A., Loucks, R.G., Mescher, P., Zeng, X., 2002. Characterization of a coalesced, collapsed paleocave reservoir analog using GPR and well-core data. Geophysics 67, 1148–1158. https://doi.org/10.1190/1.1500376

Medeiros, R.S., Biswas, D., DeGolyer, MacNaughton, Suryanarayana, P. V., 2004. Impact of thief zone identification and shut-off on water production in the nimr field. SPE/IADC Underbalanced Technol. Conf. Exhib. - Proc. 297–303. https://doi.org/10.2523/91665-ms

Medekenova, A., Jones, G.D., 2014. Characterization and modeling challenges associated with fracture and karst (non-matrix) in the margin area of a carbonate reservoir. Soc. Pet. Eng. - SPE Annu. Casp. Tech. Conf. Exhib. https://doi.org/10.2118/172275-ms

Méndez, J.N., Jin, Q., González, M., Zhang, X., Lobo, C., Boateng, C.D., Zambrano, M., 2020. Fracture characterization and modeling of karsted carbonate reservoirs: A case study in Tahe oilfield, Tarim Basin (western China). Mar. Pet. Geol. 112, 104104. https://doi.org/10.1016/j.marpetgeo.2019.104104

Mount, G.J., Comas, X., Cunningham, K.J., 2014. Characterization of the porosity distribution in the upper part of the karst Biscayne aquifer using common offset ground penetrating radar, Everglades National Park, Florida. J. Hydrol. 515, 223–236. https://doi.org/10.1016/j.jhydrol.2014.04.048

Nobes, D. C. 2018. Pitfalls to Avoid in Void Interpretation from Ground Penetrating Radar Imaging. Interpretation, 1–31. doi:10.1190/int-2018-0049.1

Odling, N.E. bac., Gillespie, P., Bourgine, B., Castaing, C., Chilés, J.P., Christensen, N.P., Fillion, E., Genter, A., Olsen, C., Thrane, L., Trice, R., Aarseth, E., Walsh, J.J., Watterson, J., 1999. Variations in fracture system geometry and their implications for fluid flow in fractured hydrocarbon reservoirs. Pet. Geosci. 5, 373–384. https://doi.org/10.1144/petgeo.5.4.373

Oliveira Jr., J.G., de Medeiros, W.E., de Santana, F.L., Bezerra, F.H.R., Cazarin, C.L., 2020. Enhancing stratigraphic, structural and dissolution features in GPR images of carbonate karst through data processing. Near Surf. Geophys. 18, 135–148. https://doi.org/10.1002/nsg.12074

Pepe, M., Parise, M. 2014. Structural control on development of karst landscape in the Salento Peninsula (Apulia, SE Italy). Acta Carsologica, 43(1). https://doi.org/10.3986/ac.v43i1.643

Pessoa Neto, O.D.C., Soares, U.M., Fernandes Da Silva, J.G., Roesner, E.H., Florencio, C.P., Valentin De Souza, C.A., 2007. Bacia Potiguar. Bol. Geociencias da Petrobras 15, 357–369.

Pisani, L., Antonellini, M., Bezerra, F. H., Carbone, C., Auler, A. S., Audra, P., ... De Waele, J. 2022. Silicification, flow pathways, and deep-seated hypogene dissolution controlled by structural and stratigraphic variability in a carbonate-siliciclastic sequence (Brazil). Marine and Petroleum Geology, 139, 105611. https://doi.org/10.1016/j.marpetgeo.2022.105611

Privalov, V., Randi, A., Sterpenich, J., Pironon, J., Morlot, C. 2019. Structural control of a dissolution network in a limestone reservoir forced by radial injection of CO2 saturated solution: Experimental results coupled with X-Ray computed tomography. Geosciences, 9(1), 33.https://doi.org/10.3390/geosciences9010033

Reis, J.A. dos, de Castro, D.L., de Jesus, T.E.S., Filho, F.P.L., 2014. Characterization of collapsed paleocave systems using GPR attributes. J. Appl. Geophys. 103, 43–56. https://doi.org/10.1016/j.jappgeo.2014.01.007

Sandmeier, K.J., 2012. REFLEXWVersion 7.0, Program for the processing of seismic, acoustic or electromagnetic reflection, refraction and transmission data. Software Manual, Karlsruhre, Germany.

Santos, B. B.; Dantas, R.; Medeiros, W. E.; Lopes, J. A. G.; Oliveira Jr., J.; Santana, F. L., 2022, A linear approach to simulate a constant-Q model in time-domain GPR modeling using multiple Debye poles: Theory and application in karst carbonate rocks: Geophysics, in press. https://doi.org/10.1190/geo2021-0731.1.

Silva, O.L., Bezerra, F.H.R., Maia, R.P., Cazarin, C.L., 2017. Karst landforms revealed at various scales using LiDAR and UAV in semi-arid Brazil: Consideration on karstification processes and methodological constraints. Geomorphology 295, 611–630. https://doi.org/10.1016/j.geomorph.2017.07.025

Tian, Z., Guo, R., Xu, Z., Yi, L., 2019a. Quantitative Petrophysical Characterization of Original Super-Permeability Zones of Bioclastic Limestone Reservoir. Springer Singapore. https://doi.org/10.1007/978-981-10-7560-5

Tian, F., Di, Q., Jin, Q., Cheng, F., Zhang, W., Lin, L., ..., Li, Y. 2019b. Multiscale geological-geophysical characterization of the epigenic origin and deeply buried paleokarst system in Tahe Oilfield, Tarim Basin. Mar. Pet. Geol., 102, 16-32. https://doi.org/10.1016/j.marpetgeo.2018.12.029

Tian, F., Luo, X., Zhang, W., 2019c. Integrated geological-geophysical characterizations of deeply buried fractured-vuggy carbonate reservoirs in Ordovician strata, Tarim Basin. Mar. Pet. Geol. 99, 292–309. https://doi.org/10.1016/j.marpetgeo.2018.10.028

Vernengo L., and Trinchero E, 2015, Application of amplitude volume technique attributes, their variations, and impact. The Leading Edge 34, 1246–1253.

Wu, X., Yan, S., Qi, J., Zeng, H., 2020. Deep Learning for Characterizing Paleokarst Collapse Features in 3-D Seismic Images. J. Geophys. Res. Solid Earth 125. https://doi.org/10.1029/2020JB019685

Wunderlich, T., Rabbel, W., 2011. Attenuation of GPR Waves in Soil Samples Based on Reflection Measurements. 2011 6th Int. Work. Adv. Gr. Penetrating Radar. https://doi.org/10.1109/IWAGPR.2011.5963879

Xavier Neto, P., Eugênio de Medeiros, W., 2006. A practical approach to correct attenuation effects in GPR data. J. Appl. Geophys. 59, 140–151. https://doi.org/10.1016/j.jappgeo.2005.09.002

Yan, L., Liu, Q., Liu, X., 2022. Research on 3D geological modeling of fractured-vuggy carbonate reservoirs. Energy Reports 8, 491–500. https://doi.org/10.1016/j.egyr.2022.03.052

Yılmaz, Öz (2001). Seismic data analysis. Society of Exploration Geophysicists.

Yixiang, Z., Xinmin, S., Benbiao, S., Shuiqing, H., Changbing, T., Yan, G., Weimin, Z., Yong, L., 2017. Genesis of High Permeable Thief-zones and Integrated Reservoir Modeling of Intense Heterogeneous Reef-flat Carbonates: A Case Study for the Mishrif Formation of the Rumaila Oilfield, Iraq. SPE Annu. Tech. Conf. Exhib. 1–12. https://doi.org/https://doi.org/10.2118/187235-MS

Zajc, M., Pogačnik, Ž., Gosar, A., 2014. Ground penetrating radar and structural geological mapping investigation of karst and tectonic features in flyschoid rocks as geological hazard for exploitation. Int. J. Rock Mech. Min. Sci. 67, 78–87. https://doi.org/10.1016/j.ijrmms.2014.01.011

Zhang, J., Zhou, J., Fu, L., Li, H., Lou, D., 2020. Karstification of Ordovician carbonate reservoirs in Huanghua depression and its control factors. Carbonates and Evaporites 35, 1–16. https://doi.org/10.1007/s13146-020-00572-x

Zhang, X., Huang, Z., Lei, Q., Yao, J., Gong, L., Sun, S., Li, Y., 2022. Connectivity, permeability and flow channelization in fractured karst reservoirs: A numerical investigation based on a two-dimensional discrete fracture-cave network model. Adv. Water Resour. 161, 104142. https://doi.org/10.1016/j.advwatres.2022.104142.

4. DESENVOLVIMENTOS PARALELOS AO TEMA DESTA TESE

Durante a elaboração desta tese, os dados e os conhecimentos adquiridos me permitiram contribuir de maneira efetiva para o desenvolvimento de outras pesquisas, de colegas de pós-graduação da UFRN e UNICAMP, desenvolvidas no âmbito do projeto POROCARSTE 3D e também relacionadas ao estudo de fraturas e feições cársticas. Essa contribuição resultou na coautoria de três manuscritos científicos, que são descritos sumariamente a a seguir.

4.1 M-1: Impact of fracture set scales and aperture enlargement due to karstic dissolution on the fluid flow behavior of carbonate reservoirs A workflow to include sub-seismic fractures in 3D simulation models

Autores: Alexandre de Lima, Juliana A.G. Lopes, Walter E. Medeiros, Denis José Schiozer, Vincenzo La Bruna e Francisco H.R. Bezerra.

Manuscrito submetido em 24 de junho de 2022 ao *Journal of Petroleum Science and Engineering* e que está atualmente na 1ª etapa de revisão (*Moderate revision*)

M-1 resultou de uma parceria entre os projetos POROCARSTE 3D (UFRN) e SIMFRAC (UNICAMP), ambos financiados pela Shell Brasil e desenvolvidos de forma paralela. M-1 está estreitamente relacionado com o primeiro artigo resultante desta tese, que foi apresentado no Capítulo 2. Numa visão sintética, os resultados do artigo apresentado no capítulo 2 incluem um modelo estático de reservatórios carbonáticos, impactados por redes de fraturas subverticas carstificadas, enquanto que M-1 apresenta o modelo dinâmico associado. Nesta colaboração, nós fornecemos todas as informações estruturais e estatísticas sobre as fraturas e feições cársticas, que possibilitaram ao doutorando Alexandre de Lima construir os modelos DFKN's estáticos e dinâmicos. Observe-se que Alexandre de Lima é também coautor do nosso artigo (Capítulo 2).

Os resultados evidenciam que fraturas subsísmicas podem impactar significativamente o comportamento do fluxo de fluido, dependendo da localização do poço produtor em relação à rede de fraturas e do grau de dissolução cárstica. Além disso, os resultados também forneceram à indústria de petróleo e gás um fluxo de trabalho para caracterizar fraturas subsísmicas em modelos de simulação de fluxo de fluido.

4.2 M-2: The influence of subseismic-scale fracture interconnectivity on fluid flow in fracture corridors of the Brejões carbonate karst system, Brazil

Autores: Carla P.Q. Furtado, Walter E. Medeiros, Sergio V. Borges, Juliana A.G. Lopes, Francisco H.R. Bezerra, Francisco P. Lima-Filho, Rubson P. Maia, Giovanni Bertotti, Augusto S. Auler, Washington L.E. Teixeira.

Publicado em 16 de abril de 2022 no periódico *Marine and Petroleum Geology*

https://doi.org/10.1016/j.marpetgeo.2022.105689

Link de acesso: https://www.sciencedirect.com/science/article/abs/pii/S0264817222001672

M-2 apresenta um estudo multidisciplinar e multiescalar em corredores de fraturas da Formação Salitre, Bacia de Irecê, Bahia, para investigar o impacto de feições subsísmicas no fluxo de fluido. A minha contribuição foi centrada em auxiliar na interpretação das redes de fratura e nas análises estatísticas. A interpretação regional revelou que a formação de corredores de fraturas está associada com um anticlinal de direção N-S. Um estágio avançado de carstificação causou o alargamento de fraturas e dissoluções intracamadas, levando à formação de cavernas e cânions estruturalmente controlados. Como resultado do avançado processo de carstificação, foram criados grandes volumes de macroporosidade secundária, principalmente na zona de maior intensidade de fraturas, próxima ao eixo principal da dobra. Este cenário pode ser usado para compreender melhor os reservatórios formados em ambiente com controles estruturais semelhantes.

4.3 M-3: A linear approach to simulate a constant-Q model in time-domain GPR modeling using multiple Debye poles: Theory and application in karst carbonate rocks

Autores: Bruno B. Santos, Renato R. S. Dantas, Walter E. Medeiros, Juliana A. G. Lopes, Josibel G. Oliveira Jr., Flávio L. Santana.

Pre-print publicado em 04 de setembro de 2022 no *Geophysics*

https://doi.org/10.1190/geo2021-0731.1

Link de acesso: *https://library.seg.org/doi/10.1190/geo2021-0731.1*

M-3 está estreitamente relacionado com o manuscrito apresentado no Capítulo 3 desta tese. M-3 apresenta uma eficiente abordagem linear para modelar, no domínio do tempo, seções sintéticas de GPR incluindo os efeitos dispersivos causados pela variação de fator de qualidade Q. A minha contribuição foi interpretar as imagens de GPR de campo utilizadas, que fazem parte de um dos cubos de GPR utilizados na presente tese. M-3 demonstrou que as zonas de atenuação de sinal de GPR, que caracterizamos no Capítulo 3, podem ser modeladas como zonas de relativamente baixo fator de qualidade Q, assim confirmando o seu caráter de dispersão ou atenuação de sinal.

5. CONCLUSÕES

Esta tese apresentou uma abordagem multidisciplinar e multiescalar integrada para avaliar e compreender como a dissolução cárstica afeta a porosidade e permeabilidade das rochas carbonáticas fraturadas e carstificadas da Formação Jandaíra. As análises 2D e 3D realizadas demonstraram que as redes de fratura representam as principais rotas para o fluxo de fluido e contribuem efetivamente para o aumento da dissolução cárstica.

A combinação entre dados de afloramentos (*scanlines*) e imagens de VANT mostrou como a conectividade das fraturas influencia na distribuição da rede carstificada. Quanto menor for a conectividade do sistema, maior será a concentração/canalização do fluxo em fraturas mais longas, o que leva a um maior alargamento dessas estruturas. Com a evolução temporal do processo, já em sistemas altamente conectados, todos os comprimentos de fraturas influenciam na percolação de fluidos, levando a uma dissolução mais uniforme. Desse modo, o processo de alargamento das fraturas, devido a carstificação, altera as distribuições estatísticas das aberturas, que passam de uma relação abertura-comprimento linear em um gráfico bilogarítmico, para aberturas aproximadamente constantes em um estágio de carstificação muito avançado. Como resultado, o alargamento das fraturas promove um aumento de até cinco ordens de grandeza na transmissividade do sistema de fraturas, o que implica que sistemas com a mesma conectividade podem apresentar diferentes valores de transmissividade.

Por sua vez, a interpretação tridimensional integrada de cubos de GPR, testemunhos de sondagem, perfis petrofísicos, imagens de paredes de poços e lâminas delgadas, nos permitiu caracterizar os principais fatores que controlam o desenvolvimento e distribuição de zonas de atenuação do sinal de GPR. Tais zonas estão relacionadas a mudanças secundárias das rochas carbonáticas, que são causadas por faturamento e/ou alterações diagenéticas, a exemplo de alargamento de poros e fraturas, bem como dissolução de estilólitos. Em casos extremos, pode haver até mesmo a criação de espaços vazios. Tais zonas alteradas podem compor volumes conectados de rocha, de alta permeabilidade, formando camadas super-K. Estes volumes em geral apresentam geometria tabular, porque são delimitados por fraturas subverticais e superfícies estratigráficas.

Esses resultados contribuem para um melhor entendimento dos processos controladores de fluxo de fluidos em reservatórios carbonáticos fraturados e carstificados, com consequente aumento da capacidade de predição dos efeitos associados durante a sua explotação.

Como sugestões para pesquisas futuras, recomendamos uma abordagem mais detalhada a respeito das estruturas (poros e estilólitos) que compõem as principais unidades estratigráficas nos afloramentos estudados. Essa abordagem poderia incluir estudos mais amplos em lâminas delgadas, visando uma análise mais precisa a respeito dos tipos de porosidade e da sua relação com os arcabouços estratigráficos e estruturais, bem como um olhar mais detalhado com relação à dissolução de estilólitos, veios e fraturas na escala micro. Além disso, sugerimos também análises químicas, como Difratometria de Raios X (DRX) e Espectrometria de Energia Dispersiva de Raios X (EDS), para definição dos tipos de matriz e cimento. Estas análises poderim contribuir para uma compreensão mais aprofundada dos fatores controladores da dissolução cárstica. Por fim, são necessários estudos aprofundados a respeito dos parâmetros de permissividade dielétrica e fator de qualidade Q de rochas carbonáticas, para que se obtenha uma compreensão petrofísica aprofundada das causas da atenuação do sinal de GPR.